Wave Effects on Power Mismatch Losses in Offshore Floating PV

SET3901: Graduation Project

Philipp Tiwald

Delft University of Technology

Wave Effects on Power Mismatch Losses in Offshore Floating PV

by

Philipp Tiwald

to obtain the degree of Master of Science in
Sustainable Energy Technology
at the Delft University of Technology,
Friday, July 7, 2023

Student Name	Student Number
Philipp Tiwald	5621542

Thesis committee

Chair	Dr. R.A.C.M.M. van Swaaij	PVMD, ESE, EWI, Associate Professor
External Member	Dr. G. Lavidas	Offshore Engineering, CiTG, Assistant Professor
Supervisor	Dr. H. Ziar	PVMD, ESE, EWI, Assistant Professor
Supervisor	Dr. O.J. Colomés Gené	Offshore Engineering, CiTG, Assistant Professor
Daily Supervisor	Ir. A. Alcañiz	PVMD, ESE, EWI, PhD candidate

Preface

As I write these lines, I am concluding my ”Sustainable Energy Technology” master’s program at Delft University of Technology. Over the past two years, I had the opportunity to expand my knowledge in photovoltaic technologies and electrical engineering, in addition to my previous background in mechanical engineering. This thesis allowed me to combine both sets of knowledge, and I am delighted to have chosen this program, which has equipped me to tackle challenges related to the ongoing energy transition. I hope my work will contribute to a better understanding of offshore floating PV, which will help reduce our reliance on fossil fuels in the future.

The last two years at TU Delft have been fabulous. Beyond the academic experiences, I have had the pleasure of crossing paths with numerous ambitious, inspiring, and kind individuals who have become dear friends. Their support has been invaluable throughout my time here, particularly during the intensive nine-month graduation project. I am sincerely grateful to each and every one of them. Enduring nine months of continuous work on the same project can be draining. However, thanks to the company of my friends, my spare moments were filled with excitement and adventure. Looking back, those nine months dedicated to my thesis flew by in an instant, and I can now reflect on a remarkably smooth journey filled with unforgettable moments. I would also like to express my gratitude to my friends from Austria and various parts of the world who visited me; some even made multiple trips during my stay in the Netherlands. Despite being physically apart, I never felt disconnected from them.

The smooth progress of my thesis was largely thanks to the daily guidance and quick responses from my supervisors, Alba and Shagun. As you might know, in the Austrian mountains, we care about water, but in a solid state. So thank you, Shagun, for explaining several topics related to ocean engineering which were not covered in detail in my bachelor’s program. I also want to express my appreciation to Alba for her continuous guidance throughout the entire process and for her assistance in addressing questions that arose after the monthly meetings. I would like to extend my thanks to Oriol for always being approachable and providing valuable input on Gridap, despite his busy schedule. Our Gridap meetings felt like solving puzzles, and I truly cherish those moments. Lastly, I want to acknowledge Hesan for raising thought-provoking questions during our monthly meetings, fostering scientific thinking and reflection on my results. I am fortunate to have had such an exceptional team of supervisors.

Last but certainly not least, I would like to express my heartfelt gratitude to my family. I am immensely thankful for their support in my decision to pursue a master’s program abroad. Despite the fact that I was rarely able to visit home or missed reaching out to them for weeks due to my busy schedule (due to university and studying, of course), they never complained.

To all readers, I hope you enjoy reading this report as much as I enjoyed working on it.

Philipp Tiwald
Delft, June 2023

Abstract

Global warming represents the most significant threat to humankind, making the need for renewable energy more crucial than ever. However, in densely populated areas near the coast, electricity production faces competition from various sectors such as agriculture, housing, and tourism. To address this challenge, one viable solution is to explore offshore electricity production.

Building upon this context, this research delves into investigating the wave-induced effect on power mismatch losses along a PV string in offshore floating photovoltaic (OFPV) systems. OFPV offers a promising solution for generating electricity in unused marine areas, complementing offshore wind energy. Although OFPV holds great potential, our understanding of its complexities remains limited, particularly regarding the impact of wave-induced power mismatch losses. To bridge this knowledge gap, a comprehensive approach is taken. A floating structure is modeled using the Bernoulli-Euler beam theory, while the fluid domain is analyzed using potential flow/linear wave theory. Structural behavior is examined in the frequency domain through the application of a FEM with the package Gridap in Julia. The wave amplitude spectra are determined using the Jonswap sea spectrum, with consideration given to four distinct sea states based on the Douglas sea scale: slight, moderate, rough and very rough. The optoelectrical modeling is conducted in pvlib in Python.

The results reveal that monthly energy losses due to power mismatch are negligible during summer months for all sea states studied. However, in winter months, monthly energy losses exceed 1%, with daily losses reaching up to 6%. Additionally, the orientation of the PV string is identified as a crucial parameter for minimizing losses. Finally, the findings indicate that using either a thick structure with a stiff and dense or a thin structure with a flexible and lightweight material can help reduce energy losses caused by power mismatch.

Contents

Nomenclature

Abbreviations

Abbreviation	Definition
2D	Two-dimensional
AC	Alternating current
°C	Degree Celsius
DC	Direct current
E	East
EPS	Expanded polystyrene
EU	European Union
FEM	Finite element method
FPV	Floating photovoltaic
GFRP	Glass fiber reinforced polymer
GW	Gigawatt
HDPE	High-density polyethylene
I-V	Current-Voltage
IPCC	Intergovernmental panel on climate change
kg/m^3	Kilogram per cubic meter
kW(p)	Kilowatt(-peak)
LCOE	Levelized cost of electricity
MAE	Mean absolute error
MPPT	Maximum power point tracker
MW(p)	Megawatt(-peak)
N	North
OFPV	Offshore floating photovoltaic
PDEs	Partial differential equations
PDF	Probability density function
PV	Photovoltaic
PVC	Polyvinyl chloride
RAO	Response amplitude operator
STC	Standard test condition
VLFS	Very large floating structure
W/m^2	Watt per square meter

Symbols

Symbol	Definition
A	Area of the cross-section
A_M	Module's azimuth
A_S	Sun's Azimuth
A_0	Wave's Amplitude
D_R	Wind turbine's rotor diameter
DHI	Diffused horizontal irradiance
DNI	Direct normal irradiance
d	Water depth
E_b	Beam's Young's modulus

Symbol	Definition
E_{DC}	DC Energy
e	Euler's number
FF	Fill factor
f	Frequency
f_s	Sample frequency
$\hat{G}$	Fourier transform
G_M	Total in-plane irradiance on a module
G_M^{dif}	Diffused irradiance component
G_M^{dir}	Direct irradiance component
G_M^{ground}	Ground reflected irradiance component
GHI	Global horizontal irradiance
g	Gravitational constant
H	Height outer rectangle of hollow cross-section
H_s	Significant wave height
h	Height inner rectangle of hollow cross-section
h_b	Beam's height/thickness
I	Geometrical moment of inertia
I_{mpp}	Current at maximum power point
I_{sc}	Short circuit current
i	Imaginary unit
J	Joint
k	Wavenumber
k_B	Boltzmann constant
k_r	Spring constant
L_b	Beam's length
N_d	Number of days
N_f	Number of frequencies
N_s	Number of samples in time signal
N_S	Number of cells in a module
n	Ideality factor
$\vec{n}$	Normal vector
P_{ideal}	Ideal power output
P_{losses}	Power mismatch losses
P_{max}	Power at maximum power point
P_{sys}	System's power output
p	Pressure
p_{h_n}	Wall thickness
q	Elementary charge
SVF	Sky view factor
T	Wave period
T_M	Module's temperature
T_p	Peak wave period
u_{in}	Inlet velocity
u_{out}	Outlet velocity
V_{mpp}	Voltage at maximum power point
V_{oc}	Open circuit voltage
$\vec{v_w}$	Direction of the wave propagation
W	Width
x	x-coordinate
y	Real value
$\hat{y}$	Approximated value
α	Albedo
α_S	Sun's altitude
α_{sc}	Short circuit temperature coefficient

Symbol	Definition
β_j	Scaling factor of peak enhancement factor
β_{oc}	Open circuit temperature coefficient
Γ_b	Beam surface
Γ_d	Inlet damping surface
Γ_{fs}	Free water surface
Γ_{in}	Inlet surface
Γ_{out}	Outlet surface
Γ_{sb}	Seabed surface
γ	Peak enhancement factor
γ_{aoi}	Angle of incidence
γ_I	Scaling parameter for I
$d\omega$	Stepsize in frequency spectrum
ϵ	Phaseshift
η	Beam's surface elevation
η_x	Beam's surface slope with respect to x-direction
θ_M	Module's tilt
θ_z	Sun's zenith
κ	Free surface elevation
κ^*	Reduced free surface elevation
κ_{in}	Free surface elevation at the inlet
λ	Wavelength
μ	Mean
μ_0	Target damping coefficient
μ_1	Damping coefficient
μ_2	Damping coefficient
V_η	Functional space on η
V_κ	Functional space on κ
V_Ω	Functional space on Ω
π	Pi constant
ρ_b	Beam's density
$\rho_{b_{reduced}}$	Reduced beam's density
ρ_w	Water density
σ	Shape function
σ	Standard deviation
ϕ	Velocity potential
ϕ^*	Reference velocity potential
ϕ_{in}	Velocity potential at the inlet
∇	Nabla operator
$\nabla^2 = \Delta$	Laplace Operator
Ω	Fluid domain
ω	Wave's angular frequency
ω_n	Eigenfrequencies

1 Introduction

Climate change has emerged as one of the most pressing global challenges of our time. The latest report by the Intergovernmental Panel on Climate Change (IPCC) [1] has painted a drastic picture of the consequences we face if immediate and decisive action is not taken. The urgency to mitigate climate change and transition to renewable energy sources has never been greater. Renewable energy, particularly solar power, plays a pivotal role in this energy transition, offering a sustainable and environmentally friendly solution to meet our growing energy demands. For instance, the European Union (EU) aims to have 750 gigawatts (GW) of installed photovoltaic (PV) power by 2030, according to [2].

However, large-scale solar power installations pose challenges due to their significant land requirements, which can put pressure upon sectors such as accommodation or agriculture [3]. Land scarcity is even more pronounced in densely populated areas, where electricity demand is high. Hence, with over 50% of the global population residing within 100km from the coastline [4], there is a pressing need to explore alternative locations for large-scale solar power installations.

The sea presents a promising location for renewable energy installations. While offshore wind technology has reached maturity, with over 2,600 wind farms already installed in the North Sea [5], offshore floating photovoltaic (OFPV) systems are still a relatively new technology. However, there are ambitious plans to deploy large-scale OFPV systems in the North Sea. Notably, the EU-Scores program [6] aims to install OFPV within existing wind farms, maximizing electricity output per unit area. This integrated approach optimizes the utilization of electrical infrastructure and promotes efficient use of resources.

Deploying floating photovoltaic (FPV) systems, especially offshore, is not trivial and involves considering various factors. The electrical components are exposed to the humid and salty ocean environment, necessitating careful material selection and maintenance. Additionally, the motion of the structure caused by waves or the potential environmental impacts on the ocean must be considered.

To address the limited research on the behavior of OFPV systems and their impact on power mismatch losses, this study aims to fill the existing knowledge gap. This chapter provides an extensive literature review on OFPV, covering key aspects such as its general description, market development, and the research conducted on wave-structure interaction and its effects on PV yield in section 1.1. The research gaps and relevant questions to be explored within this thesis are presented in section 1.2. Additionally, the research approach and the overall structure of the thesis are outlined in section 1.3, providing a clear roadmap for subsequent chapters and analysis.

1.1. Literature Review on (Offshore) Floating PV

This section aims to provide general information about OFPV systems. The section begins with a description of floating photovoltaic FPV and OFPV systems in subsection 1.1.1, outlining the essential components required for constructing such systems. It also discusses the advantages, disadvantages, and challenges associated with OFPV. Subsequently, in subsection 1.1.2, the development of FPV technology from its early stages to the current state of market solutions for OFPV is explained. Lastly, information regarding the modeling of OFPV system is provided in subsection 1.1.3

1.1.1. Description of Offshore Floating PV

A schematic diagram illustrating the configuration of a FPV system is presented in Figure 1.1. As of today, typically utilized in inland water bodies, the FPV system consists of pontoon or float structures that serve as platforms for accommodating PV modules. These PV modules are interconnected through strings and connected to a DC-AC inverter, facilitating the conversion of DC power generated by the modules into AC power. To ensure the stability and position retention of the floating structures, mooring lines are strategically employed and anchored in the seabed.

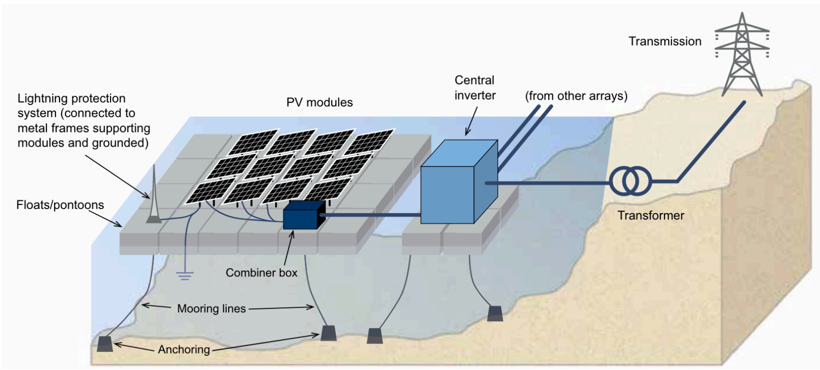

Figure 1.1: Schematic of an (O)FPV system [7].

Types of Floating Structures

Different types of floating structures can be distinguished for (O)FPV systems, as described by Ziar [8] as depicted in Figure 1.2. These include a pure-float floating structure, pontoons interconnected with steel frames and lightweight structures that enable a large plastic-water contact area. Each of these options possesses its own set of advantages and disadvantages, warranting careful consideration. The pure-float floating structure, despite its lightweight nature, renders vulnerability to wind and wave forces, thereby exerting stress on the mooring system. Nevertheless, its ease of deployment and cost-effectiveness make it an attractive choice. The second alternative, incorporating pontoons interconnected with steel frames, entails higher costs and intricate construction processes, as underscored by Kim et al. [9]. However, this design affords the advantages of sun-tracking capability and increased tilt installations. In contrast, a notable drawback of the third option is the necessity for modules to lie flat on the membrane, precluding the ability to mount them at desired tilts. However, these structures with extensive plastic-water contact areas offer the advantage of a cooling effect resulting from the close proximity of PV modules to the water surface.

(a) Pure-floats [10] **(b)** Interconnected pontoons [11] **(c)** Structure with plastic-water contact [12]

Figure 1.2: Different types of floating structures as defined by Ziar [8]: (a) Pure-floats, (b) Interconnected pontoons, and (c) Structure with plastic-water contact.

Components of a (O)FPV System

While sharing several common components with land-based PV systems, such as PV modules, inverters, mounting structures and cables, OFPV systems must additionally exhibit a high degree of resilience and durability to withstand the harsh marine environment. Given the corrosive nature of saltwater, stringent measures must be taken to safeguard the system components against corrosion and degradation caused by exposure to the marine environment [7]. To address this, the pontoon structures, typically interconnected using pins, are often constructed using high-density polyethylene (HDPE) due to its favorable combination of durability and cost competitiveness. This choice of material ensures that the pontoons can withstand the challenging conditions encountered at sea while maintaining their structural integrity [7, 13].

The requirements imposed on both the pontoons and the mooring/anchoring system are rigorous, as they must endure the considerable forces exerted by waves and wind loads to effectively secure the (O)FPV system in its intended location [13]. A substantial number of mooring lines, approximately 30 per megawatt-peak (MWp) of installed FPV capacity, are typically deployed to ensure sufficient stability and positioning of the system [8].

Advantages and Disadvantages

FPV, including both offshore and onshore applications, offers numerous advantages, as supported by several studies [7, 8, 14, 15]. Notable advantages include:

- **Saving land**. Using water bodies or the sea for energy production reduces stress and competition for land resources such as housing, food production, or infrastructure.

- **Increased efficiency**. The marine environment provides a cooling effect on PV cells, leading to improved power output. With PV cells having a negative temperature power coefficient, lower temperatures increase efficiency.

- **Less evaporation and algal growth**. FPV systems assist in reducing water evaporation in inland water bodies used as agricultural reservoirs. Additionally, they help mitigate algal bloom, thereby improving water quality.

- **Synergy with wind energy**. By harnessing solar energy during clear sky days, OFPV systems complement wind energy generation, which is often associated with adverse weather conditions. The combination of wind and solar power can be facilitated through shared grid infrastructure, enabling support for large offshore wind farms and OFPV plants.

- **Simple deployment**. The utilization of modular pontoons in (O)FPV systems offers the advantage of rapid deployment, enabling the assembly of the system directly at the waterfront. This efficient approach facilitates the installation of up to 1 MWp per day.

Indeed, the field of OFPV systems presents several challenges and disadvantages, as highlighted in various studies and reports [7, 8, 15, 16]. These challenges include:

- **No specific guidelines**. Due to its relatively early stage of development, the field of OFPV systems currently lacks established standards and guidelines. The existing standards that are applied to ground-based PV systems cannot be directly translated or utilized for systems deployed above water. These standards are designed to ensure long lifetimes for PV systems but may not adequately address the unique challenges and requirements associated with OFPV installations.

- **High costs**. When comparing OFPV installations to land-based PV systems, the former currently involves higher costs. These costs can be attributed to two main factors: the need for a floating structure (floaters and anchoring/mooring system) and the more stringent specifications for electrical components. The levelized cost of electricity (LCOE) for an OFPV system can be lowered when the system is installed in shallow waters [17].

- **Effect on eco-system**. FPV systems can potentially lead to adverse effects on the water ecosystem. Restricting oxygen and gas exchanges between the water surface and the ambient environment can result in anaerobic conditions, impacting microbial communities and water chemistry. Additionally, the coverage of the water surface by PV modules reduces solar radiation penetration, potentially negatively affecting the water ecosystem despite the beneficial reduction of algal growth. Another concern is the risk of chemical pollution arising from the installation, maintenance, or lifespan of FPVs, including the chemicals present in PV modules, floats, and other components of the system.

- **Environmental challenges**. The constant exposure of electrical systems in FPV installations to humidity and potential salinity poses long-term operational risks. Furthermore, the constant motion of floating structures accelerates degradation, corrosion and bio-fouling, necessitating periodic component reinforcement or replacement for sustained reliability and safety.

1.1.2. Development of (O)PFV

Commercial FPV projects began with the construction of the inaugural FPV system in Aichi, Japan in 2007 [18]. Since then, numerous ventures have been undertaken across various regions, including Japan, the United States, Italy and China. Notably, these projects have primarily been deployed on inland water bodies such as reservoirs and lakes. As reported by the World Bank, the cumulative installed FPV capacity worldwide reached 1314 MWp in 2018 [7], and by 2021, it had already surged to 3000 MWp [19].

The foray into OFPV commenced approximately a decade after the establishment of the first FPV system in Japan. In 2017, the Dutch consortium ”Zon op Zee” (Solar at Sea) was founded with the goal of installing an offshore floating solar utility. This vision was realized in November 2017 when Oceans of Energy successfully deployed an 8.5 kilowatt-peak (kWp) system in the Dutch North Sea, claiming the title of the first offshore floating solar farm [20]. In January 2023, Oceans of Energy received the ”Approval of Principle” for their offshore, high-wave solar farm from Bureau Veritas, affirming the success demonstrated by their 0.5 MW system over the past three years [21]. Another pioneer in the offshore solar domain is the Austrian company ”Swimsol,” which launched its inaugural offshore solar installation at sea in 2014 [22]. It is worth noting that their design is specifically suited for offshore lagoon waters with wave heights up to 2 meters [23].

In 2021, the Dutch firm ”Solar Duck” emerged on the scene, unveiling its innovative solution and successfully installing a 65 kW demonstration pilot project in inshore waters [24]. News surfaced in late 2022 that Solar Duck had secured a contract with RWE to construct an offshore solar farm as part of an offshore wind-farm project in the Dutch North Sea. The anticipated 5 MWp solar farm is slated to become operational in 2026 [25]. SolarDuck was also entrusted with the task of building an oFPV demonstrator in Tokyo Bay [26].

While the aforementioned companies employ rigid PV modules in their systems, others opt for flexible structures carrying flexible PV modules. The Norwegian company Ocean Sun uses a membrane stretched between a circular floater to carry the PV modules. Notably, the company contributed its technology to the commissioning of the first offshore wind and solar farm (0.5 MWp) by Chinese firm SPIC in 2022, with plans to expand the capacity to 20 MWp by 2023 [27]. Bluewater is also engaged in testing a novel technology utilizing flexible PV modules mounted on a flexible structure, although their solution is currently in the pilot phase [28].

The four exemplary solutions are presented in the subsequent Figure 1.3.

DNV, in its comprehensive analysis of the energy outlook for the Dutch North Sea [29], projects a substantial increase in floating solar capacity. Their report foresees a total of 100 MW of floating solar capacity by 2030 and 500 MW by 2035. These projections underscore the significant potential of OFPV in the years to come when the technology reaches maturity.

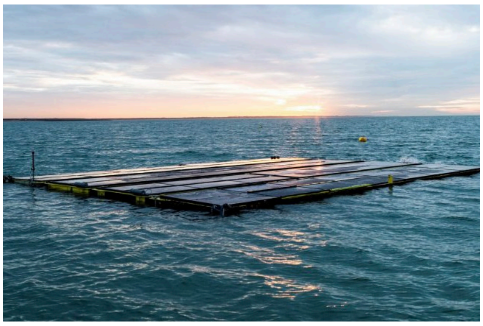

(a) Oceans of Energy

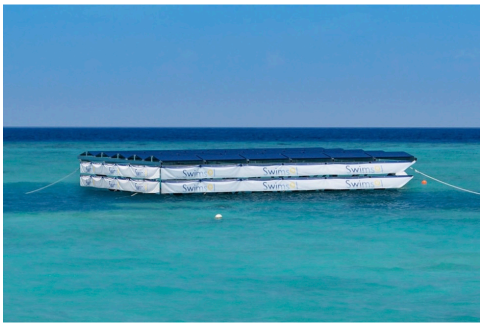

(b) Swimsol

(c) SolarDuck

(d) Ocean Sun

Figure 1.3: Four exemplary solutions of OFPV which can be found in the market.

1.1.3. Modeling OFPV

One notable advantage of OFPV systems is the enhanced performance of solar cells, attributed to the cooling effect provided by the surrounding water. Extensive research has been conducted in this area, yielding varying findings regarding the potential increase in electricity generation compared to land-based alternatives in close proximity [4, 30].

For instance, Golroodbari et al. [4] suggest that OFPV systems can achieve up to an 18% increase in electricity yield compared to a stationary system on land, while Cazzaniga et al. [30] propose an even higher increase of 20% due to the cooling effect. It is worth noting that the latter study was conducted in an inland water setting without considering wave effects. Additionally, Liu et al. [31] support the argument of a higher energy yield when comparing the performance ratio of floating systems in a testbed to rooftop-based systems in Singapore. A case study [32] carried out in the sea surrounding the Maltese island revealed that the average electrical output of the FPV system was 11% higher in comparison to a land-based system.

Other case studies have also provided confirmation of the higher yield of OFPV systems [14]. However, it is important to note that achieving the previously claimed significant increases in electricity production has not been consistently observed. Oliveira-Pinto et al. [33] highlight that the actual increase in production falls within the range of 0.31% to 2.59%. The authors attribute this discrepancy to the lack of a comprehensive simulation tool, particularly in terms of addressing thermal modeling, which makes it challenging to estimate the exact electricity output accurately.

Thus, while the cooling effect of water on solar cells in OFPV systems does enhance performance, the precise extent of the increase in electricity generation remains a topic of ongoing research and debate, with various factors such as location, environmental conditions, and modeling tools influencing the observed outcomes [4, 30, 33].

Accurately modeling the thermal behavior of OFPV systems is essential, but it is also crucial to consider the effects of waves. Waves can induce changes in module tilt, leading to variations in in-plane irradiance. This becomes particularly relevant when modules connected along a single string experience different irradiance levels due to varying tilts. This leads to power mismatch losses. To address the issue of waves, waves are often modeled as forces that generate a torque on the rigid pontoon holding a module when the force acts outside the center of mass [4, 17, 34, 35].

Research [34] demonstrates that waves can have positive effects on energy yield. However, for severe sea conditions, average wave-induced losses of nearly 18% compared to a stationary PV system mounted at optimal tilt can occur. Compared to a 0° stationary PV system, the losses stay below 1% [34]. Dörenkämper et al. [35] address the aforementioned issue of power mismatch losses resulting from modules experiencing different tilts and, consequently, different in-plane irradiance. Their research demonstrates that in situations where modules along a string have different tilts due to wave-induced torque, power mismatch losses can reach values of up to 9% in the worst-case scenario.

Mechanical models have been developed to investigate the forces and moments experienced by the floaters in OFPV systems. Wave loads for OFPV and wind loads for FPV can exert significant pressure on the floating and mooring structure, resulting in loads reaching several meganewtons (mN) as suggested by a quasi-static analytical model [13]. The stress experienced by the connection pins and the structural components is addressed by Sree et al. [36]. These studies contribute to a better understanding of the mechanical aspects and structural integrity of OFPV systems.

1.2. Research Gap and Scope of the Thesis

While this research does not specifically address the mechanical performance and induced stress on floating structures supporting PV modules, it emphasizes the crucial aspect of power mismatch losses in OFPV systems. As highlighted by Dörenkämper et al. [35], power mismatch can result in substantial energy losses, yet it remains an aspect that is not well-represented in prevailing literature. Therefore, the following research question can be raised:

- **How does power mismatch contribute to daily and monthly energy losses in offshore floating photovoltaic (OFPV) systems deployed in deep water environments?**

The following subquestions will help address and answer the main research question:

- How can the floating structure be accurately modeled to reflect real-world installations?
- What is the interaction between waves and the structure, and how does it affect the system's performance?
- What are the implications of varying tilts along the structure on power production, and how can these losses be quantified?
- How do changes in material parameters, such as density and stiffness, impact power mismatch and energy losses?

This thesis focuses on quantifying the energy losses resulting from power mismatch along a PV string in OFPV systems. Numerical values for these losses will be obtained by considering various input parameters such as material properties, sea conditions, and weather factors. A two-dimensional model incorporating a very large floating structure (VLFS) will be utilized, solving the behavior using Bernoulli Euler beam theory and potential flow/linear wave theory. A finite element method (FEM) in the frequency domain will be employed to solve the problem.

Aspects beyond the scope mentioned above, such as the structural feasibility, anchoring and mooring systems, are not addressed in this study. While these elements play vital roles in the overall design and stability of OFPV systems, their evaluation requires separate analysis. By narrowing the focus to power mismatch-related performance measures, this study aims to provide a comprehensive analysis specifically in this area, enhancing understanding and optimizing OFPV system performance.

1.3. Research Approach and Structure of the Report

This research exclusively relies on simulation methods to achieve its objectives. Mechanical modeling will be done using a FEM approach implemented in the Julia programming language using the Gridap package. For optoelectrical modeling, the pvlib library will be employed. These open-source software tools ensure reproducibility, allowing for transparency and verification of the study's findings.

This report is structured as follows: In chapter 2, the theoretical background of the study is presented, encompassing the governing equations of the mechanical and optoelectrical models, as well as wave theory. Chapter 3 outlines the methodology employed to achieve the objective of assessing power mismatch, providing a step-by-step description of the research process. The mechanical results are discussed in chapter 4, while chapter 5 focuses on presenting and discussing the results related to power mismatch and energy losses. The conclusions of the study are presented in chapter 6, and recommendations for future work are provided in chapter 7.

2 Theoretical Background

The OFPV system consists of a fluid medium and a structure where PV modules are positioned. Understanding the behavior of the fluid and structure requires the use of specific assumptions and governing equations (subsection 2.1.1-2.1.2), shedding light on their interaction (subsection 2.1.3). When considering the fluid medium as the sea, wave theory concepts are employed to accurately characterize its dynamics (subsection 2.3.1 and 2.3.2). To facilitate analysis, these equations are solved in the frequency domain using Fourier transformations (subsection 2.4.1), with the Response Amplitude Operator (RAO) defining the system's response (subsection 2.4.2). Once the behavior of the structure, including the influence of its geometrical moment of inertia (subsection 2.1.4), is described, the focus shifts to modeling the PV modules situated on the structure. In this modeling process, the incident irradiance on the modules is a crucial consideration (subsection 2.2.1), as it depends on the tilt of the modules. Finally, the power output of the PV modules can be determined (subsection 2.2.2).

2.1. Mechanical Model

In this section, the underlying mechanical model, derived from Colomes Gene et al. [37] and used in this thesis work, is presented. The model consists of two sub-parts: the structure and the fluid. The governing equations of each part are presented in subsection 2.1.1 - subsection 2.1.2, respectively. The interface between the fluid and the structure is introduced in subsection 2.1.3.

The simplified problem is depicted in Figure 2.1. The fluid domain is denoted as Ω. The boundaries are given by the inlet surface, Γ_{in}, the seabed, Γ_{sb}, the outlet surface, Γ_{out}, the free water surface, Γ_{fs}, the structure, Γ_b and the inlet damping, Γ_d. The structure is modeled as a beam of length L_b consisting of n equally long pieces. They are connected via $(n-1)$ joints J_{n-1}, modeled as rotational springs with a spring constant k_r. The beam is defined by its height h_b, Young's modulus E_b, and density ρ_b.

The assumptions underlying this model, which are common simplifications in describing VLFS according to Colomes Gene et al. [37], are as follows:

Assumption 1 In Ω, the fluid is inviscid, incompressible, and irrotational, enabling an effective description using the concept of linear potential flow. Moreover, the absence of cavitation is assumed, ensuring that there is no detachment between the structure and the fluid.

Assumption 2 The incident waves possess a small steepness and can be accurately characterized using the linear Airy wave theory.

Assumption 3 The floating structures can be described with the linear Euler-Bernoulli beam theory, given their thin nature.

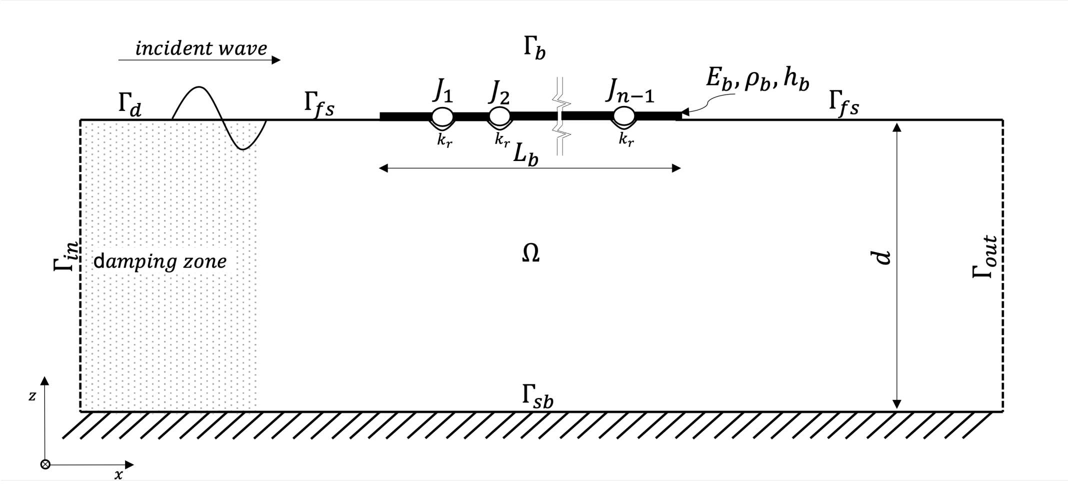

Figure 2.1: Sketch of the model used in this work.

2.1.1. Governing Equations of the Fluid

Based on Assumption 1, the behavior of the fluid can be described using the velocity potential ϕ, satisfying the Laplace equation in the fluid domain.

$$\nabla^2 \phi = 0 \quad \text{in} \quad \Omega \tag{2.1}$$

Based on Bernoulli's equation for pressure in a potential flow, neglecting the quadratic terms based on Assumption 2, one can write the linearized condition.

$$\frac{\delta \phi}{\delta t} \rho_w + p + g \rho_w \kappa = 0 \quad \text{on} \quad \Gamma_{fs} \tag{2.2}$$

ρ_w: Density of water p: Pressure g: Gravitational constant κ: Free surface elevation

Boundary conditions

The fluid domain is bounded by the free water surface, the inlet and outlet, and the seabed. The kinematic boundary conditions are derived as follows. No water is allowed to flow into or out of the seabed. Hence, the velocity, e.g., the derivative of the potential ϕ normal to the seabed, equals 0, resulting in Equation 2.3. For the fluid domain, $\vec{n}$ denotes the normal vector pointing to the outside of any surface.

$$\vec{n} \cdot \nabla \phi = 0 \quad \text{on} \quad \Gamma_{sb} \tag{2.3}$$

On the inlet and outlet surface, a prescribed inlet u_{in} and outlet u_{out} velocity are enforced, respectively. In addition, it is important to note that the waves originate from the left at $x = -\infty$ and propagate towards the right at $x = +\infty$. Reflective behavior of waves at the system boundaries is prohibited. Consequently, the Sommerfeld radiation conditions must be fulfilled for the potential of the fluid ϕ at the boundaries denoted as $\Gamma_{-\infty}$ and $\Gamma_{+\infty}$. The boundary conditions, thus, read as follows:

$$\vec{n} \cdot \nabla \phi = u_{in} \quad \text{on} \quad \Gamma_{in} \tag{2.4}$$

$$\vec{n} \cdot \nabla\phi = u_{out} \quad \text{on} \quad \Gamma_{out} \tag{2.5}$$

$$\lim_{x\to\infty} \sqrt{x}(\frac{\delta}{\delta x} \pm ik)\phi = 0 \quad \text{on} \quad \Gamma_{-\infty} \quad \text{and} \quad \Gamma_{+\infty} \tag{2.6}$$

The kinematic boundary condition on the free water surface can be expressed as in Equation 2.7. It is important to note that Assumption 2 must be satisfied for this condition. Only at a small wave steepness the normal vector of the velocity $\vec{n}$ can be described by the vertical velocity component accurately. The dynamic boundary condition for the free surface is stated in Equation 2.8, which is derived from Equation 2.2, assuming the atmospheric pressure to be 0.

$$\vec{n} \cdot \nabla\phi = \frac{\delta\kappa}{\delta t} \quad \text{on} \quad \Gamma_{fs} \tag{2.7}$$

$$\frac{\delta\phi}{\delta t} + g\kappa = 0 \quad \text{on} \quad \Gamma_{fs} \tag{2.8}$$

2.1.2. Governing Equations of the Structure

The structure can be described using the Bernoulli-Euler Beam theory as stated in Assumption 3. The governing equation reads as follows.

$$\rho_b h_b \frac{\delta^2\eta}{\delta t^2} + EI\frac{\delta^4\eta}{\delta x^4} = p \quad \text{on} \quad \Gamma_b \tag{2.9}$$

ρ_b:	Beam's density	E:	Young's Modulus	h_b:	Beam's height
η:	Beam's surface elevation	I:	Geometrical moment of inertia		

Boundary conditions

In the illustrated configuration shown in Figure 2.1, the various segments of the beam are interconnected using joints that are modeled as rotational springs. At each joint, specific requirements must be met to ensure structural integrity. These requirements are the continuity of displacement and rotation, as well as the equilibrium of forces on both sides of the joint. The signs "$+$" and "$-$" in the subsequent equations correspond to the left and right sides of the joint, respectively.

$$\eta|_{J_i^-} = \eta|_{J_i^+} \quad \forall i \in (1, n-1) \tag{2.10}$$

$$\frac{\delta\eta}{\delta x}|_{J_i^-} = \frac{\delta\eta}{\delta x}|_{J_i^+} \quad \forall i \in (1, n-1) \tag{2.11}$$

$$EI\frac{\delta^2\eta}{\delta x^2}|_{J_i^-} = EI\frac{\delta^2\eta}{\delta x^2}|_{J_i^+} = k_r(\frac{\delta\eta}{\delta x}|_{J_i^-} - \frac{\delta\eta}{\delta x}|_{J_i^+}) \quad \forall i \in (1, n-1) \tag{2.12}$$

$$EI\frac{\delta^3\eta}{\delta x^3}|_{J_i^-} = EI\frac{\delta^3\eta}{\delta x^3}|_{J_i^+} \quad \forall i \in (1, n-1) \tag{2.13}$$

At the initial position denoted as "L_0" and the final position referred to as "L_b", specific boundary conditions are applied. These boundary conditions allow for unrestricted motion at the ends of the structure, leading to zero moment and shear forces at those points. Consequently, the following equations can be derived to describe the structural behavior under these conditions.

$$EI\frac{\delta^2\eta}{\delta x^2}|_{x=L_0} = EI\frac{\delta^3\eta}{\delta x^3}|_{x=L_0} = 0 \quad on \quad \Gamma_b \tag{2.14}$$

$$EI\frac{\delta^2\eta}{\delta x^2}|_{x=L_b} = EI\frac{\delta^3\eta}{\delta x^3}|_{x=L_b} = 0 \quad on \quad \Gamma_b \tag{2.15}$$

2.1.3. Interface Fluid-Structure

The mathematical linkage between fluid dynamics and structural behavior can be achieved by integrating the fundamental equations governing fluid flow (Equation 2.2) and the Bernoulli-Euler equation (Equation 2.9). The resultant coupled equation can be derived in Equation 2.16. This equation encapsulates the influence of water pressure as a load acting upon the beam. The kinematic boundary condition for the fluid-structure interface is stated in Equation 2.17.

$$\frac{\rho_b h_b}{\rho_w}\frac{\delta^2\eta}{\delta t^2} + \frac{EI}{\rho_w}\frac{\delta^4\eta}{\delta x^4} + \frac{\delta\phi}{\delta t} + g\eta = 0 \quad \text{on} \quad \Gamma_b \tag{2.16}$$

$$\frac{\delta\eta}{\delta t} = \vec{n}\cdot\nabla\phi \quad \text{on} \quad \Gamma_b \tag{2.17}$$

2.1.4. Geometrical Moment of Inertia

The geometrical moment of inertia, in relation to the horizontal symmetry axis, of a solid body with a rectangular shape with height H and width W, as depicted in Figure 2.2a, can be calculated as follows.

$$I_{solid} = \frac{H^3W}{12} \tag{2.18}$$

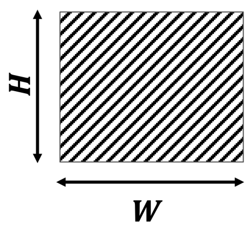

(a) Solid

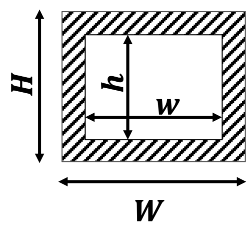

(b) Hollow

Figure 2.2: Geometrical moment of inertia for a solid and hollow rectangular body.

On the other hand, the geometrical moment of inertia for a hollow body with a rectangular shape, as shown in Figure 2.2b, can be described as stated in Equation 2.19, h and w representing the height and the width of the inner hollow rectangle, respectively.

$$I_{hollow} = \frac{H^3W - h^3w}{12} \tag{2.19}$$

2.2. Optoelectrical model

2.2.1. Total Irradiance on the Module

This section describes the underlying equations for the optoelectrical modeling conducted in this thesis. The total irradiance received by a PV module, G_M, can be calculated using the subsequent Equation 2.20. The different components, G_M^{dir}, G_M^{dif}, and G_M^{ground} are depicted in Figure 2.3.

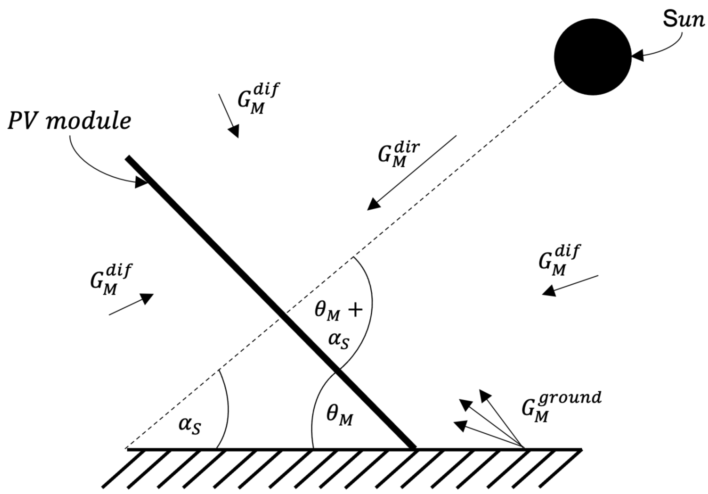

Figure 2.3: The total in in-plane irradiance G_M and its components, G_M^{dir}, G_M^{dif}, and G_M^{ground}. Figure adapted from [38].

$$G_M = G_M^{dir} + G_M^{dif} + G_M^{ground} \tag{2.20}$$

The direct irradiance on a module, denoted as G_M^{dir}, can be determined using Equation 2.21, where DNI represents the direct normal irradiance and γ_{aoi} denotes the angle of incidence.

$$G_M^{dir} = DNI \cdot cos(\gamma_{aoi}) \tag{2.21}$$

The angle of incidence, γ_{aoi} depends on the azimuth and tilt of the stationary module, as well as the sun's azimuth and altitude, which are time-dependent. These parameters collectively determine the angle at which sunlight strikes the module's surface. The calculation of the angle of incidence is shown in Equation 2.22.

$$cos(\gamma_{aoi}) = sin(\theta_M)cos(\alpha_S)cos(A_M - A_S) + cos(\theta_M)sin(\alpha_S) \tag{2.22}$$

θ_M: Module's tilt A_M: Module's azimuth A_S: Sun's Azimuth α_S: Sun's altitude

The ground reflected component, denoted as G_M^{ground}, can be computed using Equation 2.23.

$$G_M^{ground} = \alpha \cdot GHI \cdot (1 - SVF) \tag{2.23}$$

α: Albedo GHI: Global horizontal irradiance SVF: Sky view factor

The sky view factor SVF of a free horizon is computed using the equation provided in Equation 2.24. It represents the fraction of the sky dome that is visible to the module. When the module is perfectly flat, the SVF equals 1, indicating that the entire sky dome is visible. However, if the module is tilted at a 90° angle, the SVF reduces to 0.5, indicating that only half of the sky dome is visible from that perspective.

$$SVF = \frac{1 + cos(\theta_M)}{2} \tag{2.24}$$

Calculating the diffuse irradiance component on the module, denoted as G_M^{dif}, is not a straightforward process. Various models exist, each offering different levels of complexity and accuracy, which can also vary depending on the location. For this particular thesis, the Perez model [39] was employed, see Equation 2.25. This model was chosen due to its adequate level of complexity and superior performance [40] compared to other transposition models available.

$$G_M^{dif} = f(SVF, \gamma_{aoi}, GHI) \tag{2.25}$$

GHI, DHI and the direct normal irradiance DNI are related as stated in Equation 2.26.

$$GHI = DHI + DNIcos(\theta_z) \tag{2.26}$$

with θ_z the sun's zenith.

2.2.2. Power Output of a PV Module

The actual DC power output of a PV module may deviate from the value indicated on the datasheet, which is specified under standard test conditions (STC). STC refers to specific conditions where the module is exposed to an irradiance level of 1000 W/m^2, maintained at a temperature of 25°C, and subject to an AM1.5 spectrum. However, in operating conditions, the actual irradiance, temperature, and spectrum experienced by the PV module may vary. As a result, the DC power output will differ from the STC value due to the diverse environmental factors impacting the module's performance. The actual maximum power output, P_{mpp} can be obtained as shown in the subsequent equations [38]. The PV module manufacturer provides some of the parameters used in the following equations in the datasheet of the module.

$$V_{oc}(25°C, G_M) = V_{oc}^{STC} + N_S n \frac{k_B T_{STC}}{q} ln(\frac{G_M}{G_{STC}}) \tag{2.27}$$

$$I_{sc}(25°C, G_M) = I_{sc}^{STC} \frac{G_M}{G_{STC}} \tag{2.28}$$

$$P_{mpp}(25°C, G_M) = FF \cdot I_{sc}(25°C, G_M) \cdot V_{oc}(25°C, G_M) \tag{2.29}$$

k_B:	Boltzmann constant	N_S:	Number of cells of the module	n:	Ideality factor
T_{STC}:	Temperature at STC	q:	Elementary charge	G_{STC}:	Irradiance at STC
I_{sc}:	Short circuit current	V_{oc}:	Open circuit voltage	FF:	Fill factor

When the module temperature, T_M deviates from the STC value of 25°C, the following equations can be used to calculate P_{mpp} at the given module temperature. α_{sc} and β_{oc} are coefficients provided by the manufacturer.

$$V_{oc}(T_M, G_M) = V_{oc}(25°C, G_M) \cdot [1 + \beta_{oc}(T_M - T_{STC})] \tag{2.30}$$

$$I_{sc}(T_M, G_M) = I_{sc}(25°C, G_M) \cdot [1 + \alpha_{sc}(T_M - T_{STC})] \tag{2.31}$$

$$P_{mpp}(T_M, G_M) = FF \cdot I_{sc}(T_M, G_M) \cdot V_{oc}(T_M, G_M) \tag{2.32}$$

2.3. Wave Theory

This section provides a thorough explanation of the linear wave theory, which is the basis for Assumption 2. A detailed account of the theory can be found in subsection 2.3.1. It is important to note that a sea does not only consist of one sinusoidal wave but of multiple ones. These are so-called irregular waves, which are introduced in subsection 2.3.2. The analysis of irregular waves is done by using sea spectra, which are also discussed in subsection 2.3.2.

2.3.1. Linear Wave Theory

The linear wave theory is a fundamental framework used to analyze the behavior of ocean waves. It provides a simplified mathematical description of waves based on a set of underlying assumptions. The theory is derived from the governing equations of fluid motion, specifically the Bernoulli equations, under the assumption of small-amplitude waves in deep water and the potential flow of an incompressible, inviscid, and irrotational fluid. The linear wave theory assumes that the wave amplitude is small compared to its wavelength and that the water depth is much greater than the wave height. The valid regime for the application of the linear wave theory can be visually represented in Figure 2.4. This graphical depiction illustrates the range of wave conditions within which the linear wave theory holds true. Linear wave theory allows for the linearization of the Bernoulli equations, simplifying the analysis, as already introduced in subsection 2.1.1 in Equation 2.8. The complete derivation of the equations can be found in [41]. The velocity potential ϕ_{in} and free surface elevation κ_{in} are introduced in Equation 2.33 and Equation 2.34, respectively.

$$\phi_{in}(x, z, t) = \frac{A_0\omega}{k}\frac{cosh(kz)}{sinh(kd)}sin(kx - \omega t) \quad \text{in} \quad \Omega \tag{2.33}$$

$$\kappa_{in}(x, z = d, t) = -\frac{1}{g}\frac{\delta\phi}{\delta t} = A_0 cos(kx - \omega t) \quad \text{on} \quad \Gamma_{fs} \tag{2.34}$$

A_0: Wave's amplitude ω : Wave's frequency k: Wavenumber d: Water depth

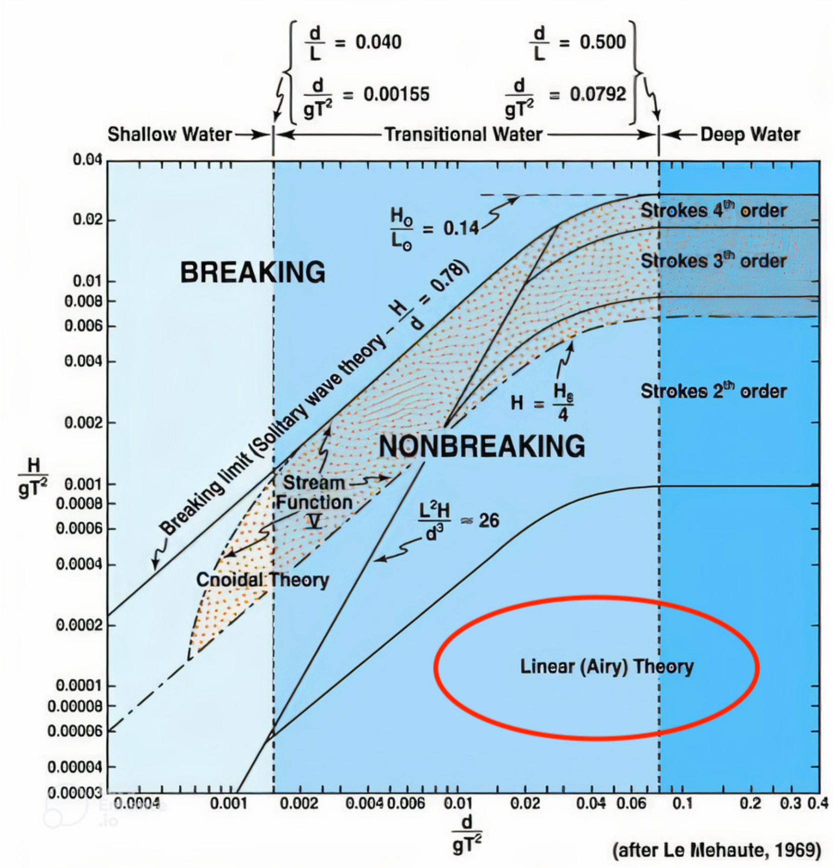

Figure 2.4: Overview of different regimes and the adequate theory to describe it [42]. In this research, the linear wave theory is used as indicated by the red circle.

The connection between the wavenumber and angular wave frequency is explained through the dispersion relationship for deep water, as mentioned in Equation 2.35. The wavenumber itself is related to wavelength λ via Equation 2.36.

$$\omega = \sqrt{gk \cdot tanh(kd)} \tag{2.35}$$

$$\lambda = \frac{2\pi}{k} \tag{2.36}$$

2.3.2. Irregular Waves: Jonswap Spectrum

To comprehend irregular seas, also known as random or confused seas, one must understand the fundamental linear wave theory. Unlike the simplified depiction of a single sinusoidal wave in Equation 2.34, the actual sea state comprises several partial sinusoidal waves with varying frequencies and amplitudes [43]. The irregular sea with N partial waves can be mathematically represented as shown in the following Equation 2.37. This equation and the relation to a wave spectrum can be visualized in Figure 2.5.

$$\kappa(t) = \sum_{i=1}^{N} A_i cos(\omega_i t + \epsilon_i) \tag{2.37}$$

When studying ocean waves, the phase angle ϵ is usually seen as arbitrary and is randomly selected from a range of $[0; 2\pi]$. This randomness accounts for the different starting points of each wave com-

A_i: Amplitude of the i[th] partial wave ω_i: Angular frequency of the i[th] partial wave
ϵ_i: Phase angle of the i[th] partial wave

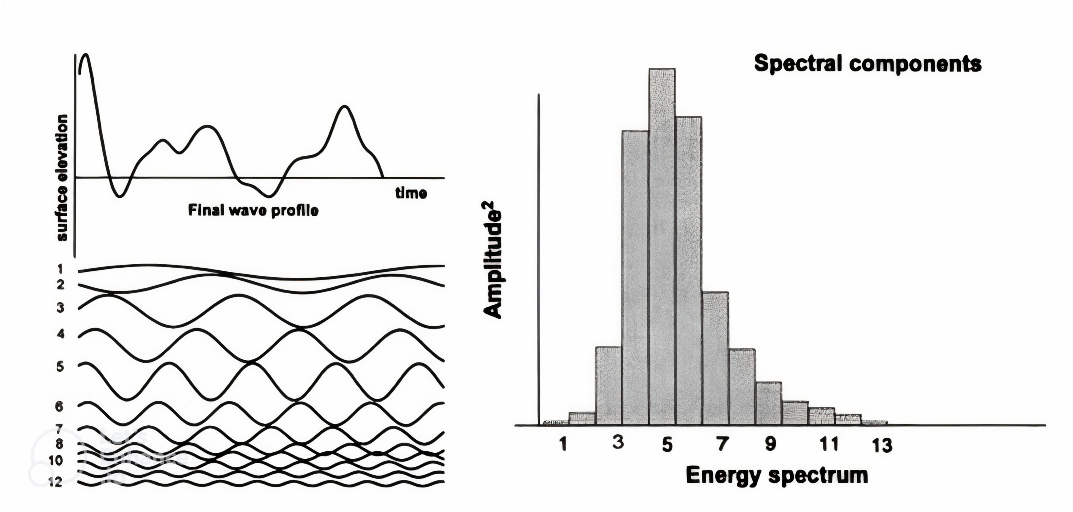

Figure 2.5: Super-position of waves (left), resulting in a wave spectrum (right) [44].

ponent in the overall wave pattern. Additionally, the amplitude of each wave is determined by an unidirectional wave amplitude spectrum. In this thesis, the North Sea Wave Observation Project (Jonswap) frequency spectrum [45] is used to describe the individual wave amplitudes. The Jonswap spectrum is similar to the Pierson-Moskowitz spectrum, but the peak of the Jonswap spectrum is more enhanced as it is used for not fully-developed seas. It is able to describe the North Sea more accurately [44]. The mathematical formulation is introduced in Equation 2.38.

$$S_{JONSWAP}(f) = \alpha g^2 (2\pi)^{-4} f^{-5} e^{-\frac{5}{4}(\frac{f}{f_m})^{-4}} \gamma^r$$
$$r = e^{\frac{-(f-f_m)^2}{2\sigma^2 f_m^2}} \tag{2.38}$$

α: Philips constant f_m: Frequency at the maximum of the spectrum
σ: Shape function γ: Peak enhancement factor

Historical wave data regarding significant wave height H_s and peak wave period T_p, two common parameters to specify sea conditions in ocean engineering, is sourced from [46] over several years for a site in the North sea with adequate water depth. Regarding the water depth, a thorough explanation of the chosen depth is provided in subsection 3.1.1. The significant wave height is the average height of the highest 33 % of the wave of a spectrum. The statistical representations of the significant wave height and peak wave period are shown in Figure 2.6a and Figure 2.6b, respectively. Hence, Equation 2.38 needs to be rewritten according to Goda [47] in terms of these two parameters, resulting in Equation 2.39.

$$S_{JONSWAP}(f) = \beta_j H_S^2 T_p^{-4} f^{-5} e^{-\frac{5}{4}(T_p f)^4} \gamma^r$$
$$r = e^{\frac{-(T_p f-1)^2}{2\sigma}} \tag{2.39}$$

H_s: Significant wave height T_p: Peak wave period β_j: Scaling factor of γ

The shape function σ can be divided into left ($f < f_p$) and right-sided ($f > f_p$), σ_a and σ_b, respectively: $\sigma_a = 0.07$ and $\sigma_b = 0.09$ are used [45]. The peak enhancement factor takes values in the range of $[1; 7]$

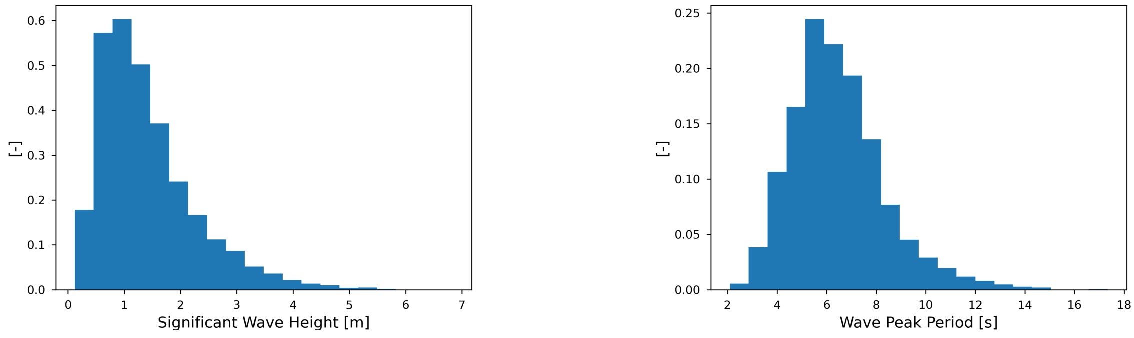

(a) H_s **(b)** T_p

Figure 2.6: Historical data for H_s and T_p. H_s is the average height of the highest one-third of waves in a wave spectrum, while T_p refers to the time interval between successive wave crests of the most energetic wave within a spectrum.

and can vary depending on sea conditions. The scaling factor β_j itself is a function of γ and can be calculated as expressed in Equation 2.40.

$$\beta_i = \frac{0.0624}{0.230 + 0.0336\gamma - 0.185(1.9+\gamma)^{-1}}(1.094 - 0.01915ln(\gamma)) \tag{2.40}$$

As the input to the mechanical model is not the wave spectral density spectrum, as calculated in Equation 2.39, the corresponding wave amplitude spectrum is derived. The resulting expression is presented in Equation 2.41, with df being the stepsize of the discretized frequency range. In addition to the amplitude spectrum $A(f)$, this research incorporates a wave-steepness spectrum $A_x(f)$ as a significant factor. The wave-steepness spectrum provides information about the slope of each wave in the spectrum, specifically with respect to the direction of wave propagation. The calculation of the $A_x(f)$ is outlined in detail in Equation 2.42. The subscript "x" in $A_x(f)$ emphasizes that the slope is determined in the x-direction, which corresponds to the direction of wave propagation, as illustrated in Figure 2.1.

$$A(f) = \sqrt{2S(f)df} \tag{2.41}$$

$$A_x(f) = \frac{2\pi A(f)}{\lambda(f)} = k(f)A(f) \tag{2.42}$$

Lastly, the wave period T, the wave frequency f and the angular wave frequency ω are related as expressed in Equation 2.43.

$$\omega = 2\pi f = \frac{2\pi}{T} \tag{2.43}$$

2.4. Frequency Domain

To speed up calculations, it is beneficial to convert partial differential equations (PDEs) into the frequency domain using the Fourier transform discussed in section subsection 2.4.1. This allows the problem to be solved for each frequency component separately. In the frequency domain, equations are solved for each specific frequency, leading to a solution that represents the system's response to that particular frequency. With the equations being linear and the superposition principle discussed in subsection 2.3.2, it is possible to solve the problem for each frequency independently, thus enabling the separate consideration of each sinusoidal wave component that makes up an irregular sea. By solving the problem for multiple frequencies and analyzing their individual responses, a comprehensive RAO that characterizes the system's response across a range of frequencies can be obtained. This approach allows for a comprehensive analysis of the system's dynamic response to the entire range of frequencies present in an irregular sea. In subsection 2.4.2 the mathematical representation of the RAO is presented.

2.4.1. Fourier Transform

In order to obtain the Fourier transform, which will lead to a complex paired function in the frequency domain, $\hat{G}$, one can use the Fourier transform pair as presented below in Equation 2.44.

$$\begin{aligned} \hat{G}(\omega) &= \int_{-\infty}^{\infty} g(t)e^{-i\omega t}dt \\ g(t) &= \frac{1}{2\pi}\int_{-\infty}^{\infty} \hat{G}(\omega)e^{i\omega t}d\omega \end{aligned} \tag{2.44}$$

with i the imaginary unit.

The linearity of the system allows for the transformation of the time-dependent equations presented in section 2.1 into the frequency domain. This transformation leads to complex-valued quantities that are dependent on frequency and space. Consequently, the solution obtained will also be in the frequency domain, representing a steady-state response. By applying Theorem 1, the time-dependent Equation 2.2, Equation 2.7, Equation 2.8, Equation 2.16 and Equation 2.17 can be rewritten as space and frequency dependent equations. To improve readability, the frequency and space dependency is not shown in the equations.

Theorem 1 $\frac{d^n g(t)}{dt^n} = (i\omega)^n \hat{G}(\omega)$

$$\frac{\delta\phi}{\delta t}\rho_w + p + g\rho_w\kappa = 0 \rightarrow -i\omega\phi\rho_w + p + g\rho_w\kappa = 0 \quad \text{on} \quad \Gamma_{fs} \tag{2.45}$$

$$\vec{n}\cdot\nabla\phi = \frac{\delta\kappa}{\delta t} \rightarrow \vec{n}\cdot\nabla\phi = -i\omega\kappa \quad \text{on} \quad \Gamma_{fs} \tag{2.46}$$

$$\frac{\delta\phi}{\delta t} + g\kappa = 0 \rightarrow -i\omega\phi + g\kappa = 0 \quad \text{on} \quad \Gamma_{fs} \tag{2.47}$$

$$\frac{\rho_b h_b}{\rho_w}\frac{\delta^2\eta}{\delta t^2} + \frac{EI}{\rho_w}\frac{\delta^4\eta}{\delta x^4} + \frac{\delta\phi}{\delta t} + g\eta = 0 \rightarrow -\frac{\rho_b h_b}{\rho_w}\omega^2\eta + \frac{EI}{\rho_w}\frac{\delta^4\eta}{\delta x^4} - i\omega\phi + g\eta = 0 \quad \text{on} \quad \Gamma_b \tag{2.48}$$

$$\frac{\delta\eta}{\delta t} = \vec{n}\cdot\nabla\phi \rightarrow -i\omega\eta = \vec{n}\cdot\nabla\phi \quad \text{on} \quad \Gamma_b \tag{2.49}$$

In analyzing the system of equations in the frequency domain, Equation 2.33 needs to be expressed without the time component. According to Andrianov [48], the time dependency in the potential ϕ can be replaced, as its shows harmonic time dependence, based on Assumption 1. Consequently, the equation describing the potential of the incident wave ϕ_{in} for a perpendicular wave with finite water depth can be rewritten as follows:

$$\phi_{in}(x,z) = \frac{gA_0}{i\omega}\frac{cosh(kz)}{cosh(kd)}e^{ikx} \tag{2.50}$$

as well as equations for the surface elevation κ_{in} and velocity over the boundary Γ_{in} in x-direction u_{in}:

$$\vec{n}\cdot\nabla\phi = -i\omega\kappa \quad \rightarrow \quad \kappa_{in} = \frac{gA_0k}{\omega^2}\frac{sinh(kz)}{cosh(kd)}e^{ikx} \tag{2.51}$$

$$\frac{\delta\phi_{in}}{\delta x} = u_{in} \quad \rightarrow \quad u_{in} = \frac{gA_0k}{\omega}\frac{cosh(kz)}{cosh(kd)}e^{ikx} \tag{2.52}$$

2.4.2. Response Amplitude Operator

The RAO is a valuable metric for analyzing dynamic systems subjected to wave forces or excitations. It quantifies the system's response in terms of amplitude at a specific frequency. The RAO represents the ratio of the system's response amplitude to the amplitude of the applied wave or excitation. In this study, the RAO is computed for two key variables.

Firstly, the RAO is calculated for the structure's elevation, denoted as η, in response to an amplitude spectrum. This RAO quantifies the system's vertical displacement as a function of the applied wave amplitude at different frequencies. Secondly, the RAO for the structure's slope, denoted as η_x, is determined in response to a wave-steepness spectrum. This RAO indicates how the structure's slope in relation to the direction of wave propagation changes, based on the wave steepness at various frequencies. The two RAOs for the elevation and slope are presented in Equation 2.53 and Equation 2.54, respectively.

$$RAO_\eta(\omega,x) = \frac{|\eta(\omega,x)|}{A(\omega)} \tag{2.53}$$

$$RAO_{\eta_x}(\omega,x) = \frac{|\eta_x(\omega,x)|}{A_x(\omega)} \tag{2.54}$$

Due to the Fourier transform, both η and η_x are complex paired functions, both dependent on the angular frequency ω and spatial position x. Thus, the absolute value is taken to calculate the RAOs. The RAO for η provides crucial information about the eigenfrequencies ω_n of the structure. The eigenfrequencies are the natural frequencies at which the system is able to oscillate without requiring any external forces or excitation. When the system is excited at or close to one of its eigenfrequencies, resonance can occur. Resonance leads to the amplification of the applied input force, resulting in the RAO exhibiting values greater than 1. This can be seen in chapter 4. The eigenfrequencies of a beam are influenced by the Young's Modulus E_b, the geometrical moment of inertial I_b, the density ρ_b, the cross-section A, and the length of the beam L_b, as stated in Equation 2.55. A complete Eigenmode analysis of the structure is out of the scope of this thesis.

$$\omega_n \propto \sqrt{\frac{E_bI_b}{\rho_bAL_b^4}} \tag{2.55}$$

2.5. Distributions and Statistics

This section serves to enhance the understanding of the distribution and statistical parameters. In particular, it explores the normal distribution and its key characteristics, such as the Central Limit Theorem, as outlined in subsection 2.5.1. The Central Limit Theorem becomes relevant when analyzing the summation of various sinusoidal waves. Additionally, the concept of the Mean Absolute Error (MAE) is introduced in subsection 2.5.2. The MAE will be utilized to quantify the errors resulting from approximations.

2.5.1. Normal Distribution

The normal distribution is an essential probability distribution that is used in many fields, including statistics, mathematics and natural sciences. It is a symmetrical distribution that takes on the shape of a bell and it is characterized by the mean μ and standard deviation σ. The probability density function (PDF) of a normal distribution is presented in Equation 2.56 [49].

$$PDF(x) = \frac{1}{\sigma\sqrt{2\pi}} e^{-\frac{1}{2}\left(\frac{x-\mu}{\sigma}\right)^2} \tag{2.56}$$

Most data is concentrated around the mean and the distribution has several useful properties, including the Central Limit Theorem. In the context of this thesis, the Central Limit Theorem becomes relevant as it indicates that the distribution of many samples tends to follow a normal distribution, even if each individual distribution is skewed [50].

This concept is applied to the summation of irregular waves, specifically in relation to the elevation and slope of the structure. Individually, the PDF of each sinusoidal wave displays maxima at the edges. However, when multiple sinusoidal waves with different frequencies are summed together, the PDF transforms into a normal distribution with a mean value of zero. The reason why the individual PDFs turn into a normal distribution is due to the combination and overlapping of multiple sinusoidal waves. This aggregation of wave characteristics results from the Central Limit Theorem, which explains how the sum of these waves leads to a normal distribution pattern. Graphically, this is depicted in Figure 2.7, which highlights how the PDF changes as soon as a sum of sinusoidal waves is formed.

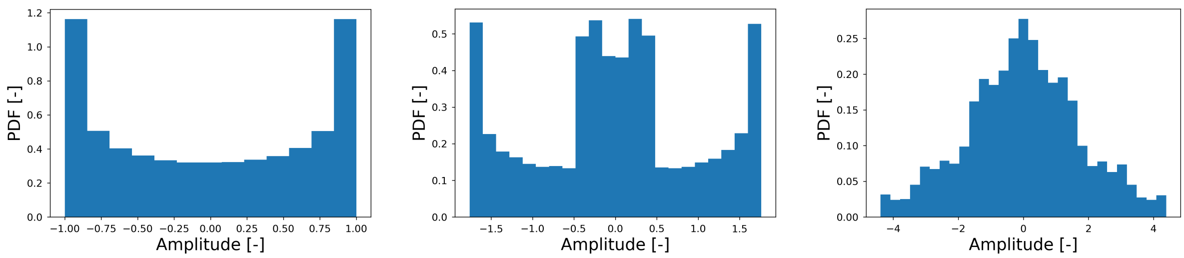

(a) One sinusoidal wave **(b)** Two sinusoidal waves **(c)** Six sinusoidal waves

Figure 2.7: PDFs for one sinusoidal wave, the sum of two and six, respectively.

2.5.2. Mean Absolute Error

The MAE is a commonly used statistical metric for measuring the accuracy and performance of approximations. It provides a straightforward measure of the average magnitude of errors between approximated and actual values without considering the direction of the errors. It can be calculated as presented in Equation 2.57.

$$MAE = \frac{1}{N}\sum_{i=1}^{N} |\hat{y} - y| \tag{2.57}$$

with y the real and $\hat{y}$ the approximated value.

When it comes to emphasizing the magnitude of errors, MAE is a useful tool. It calculates the absolute differences between approximated and actual values, providing an accurate representation of the average absolute deviation. Unlike other methods, MAE is robust to outliers and does not amplify the impact of larger errors. It treats each error equally, whether it is an overestimation or an underestimation, making it ideal for situations where both types of errors have similar implications. The interpretation of MAE is simple: the lower the MAE value, the better the prediction or approximation accuracy [51].

3
Methodology

This chapter serves to introduce the applied methods, building upon the theoretical foundation established in chapter 2. The subsequent sections outline the key steps and procedures involved in the research. To begin, section 3.1 delves into the solution of the mechanical model. This encompasses further simplifications of the model and an introduction to the FEM, which is used to solve the set of equations.

Subsequently, in section 3.2, the interconnection between the mechanical and optoelectrical models is elucidated. This section highlights the crucial link that connects the mechanical behavior of the floating structure to the optoelectrical performance of the PV modules.

Moving forward, section 3.3 elaborates on the different sea conditions considered in this research. The various sea states, which play a significant role in determining the behavior of the floating structure, are described in detail.

Finally, in section 3.4, the optoelectrical modeling approach is expounded upon. This section encompasses modeling in-plane irradiance, derivation of weather data, and determining a key parameter of interest: the power mismatch losses. The comprehensive explanation of the optoelectrical modeling process contributes to a deeper understanding of the overall system performance and its dependence on various factors. To enhance the comprehension of the entire process, a flowchart illustrating the main steps is included at the conclusion of this chapter.

3.1. Solution of the Mechanical Model

To address the challenges of the original model presented in Figure 2.1, simplifications are implemented in subsequent sections. In subsection 3.1.1, the beam is defined by considering the number of joints, the beam's length, materials, and mechanical properties, as well as the water depth of the fluid. The importance of damping zones is explained in subsection 3.1.2, highlighting their significance in solving the numerical problem.The final numerical formulation is presented in subsection 3.1.3, detailing the weak form of the problem. The choice of mesh stepsize and frequency is discussed in subsection 3.1.4, while the procedure for obtaining RAOs is highlighted in subsection 3.1.5. The resolution of the tilt, the output of the mechanical model, is addressed in subsection 3.1.6.

3.1.1. Simplifications to the Mechanical Model

Joints

The problem presented in section 2.1 entails a significant challenge: the computational time required to solve the PDEs for a beam with joints is substantially greater than for a continuous beam. This issue becomes particularly pronounced when considering the need to calculate the RAOs across a wide range of frequencies, which would have exceeded the time constraint of this project. Furthermore, the

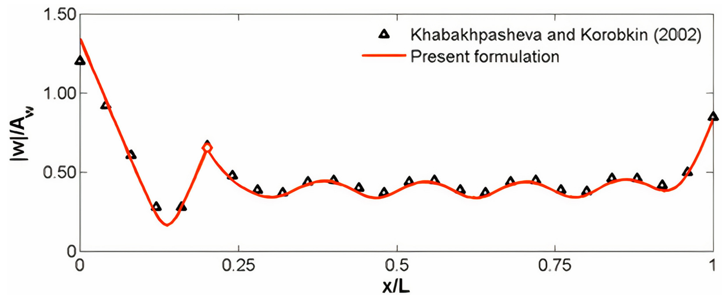

(a) Perfect hinge.

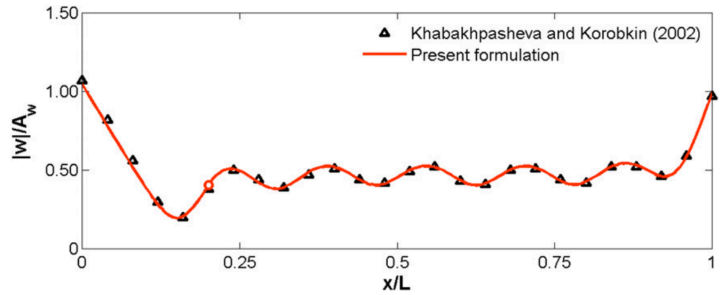

(b) Semi-rigid connection.

Figure 3.1: Normalized maximum deflection along a structure connected with a perfect hinge (top) and a semi-rigid connection (bottom) at $x/L = 0.20$. The legend indicates two different formulations. Figure from [52].

number of joints would have been an additional parameter to the entire setting, creating more combinations to be analyzed.

The research findings by Riyansyah et al. [52] can offer a solution to this problem. In their work, the authors introduce a new formulation to solve the behavior of a floating structure consisting of two beam elements and compare it to a previous study (black triangles in Figure 3.1). They also demonstrate the effect of changing the stiffness of the connection point between the two beam elements. The connection/joint in the figures is denoted by the red circle at $x/L = 0.20$. When the connection is a perfect hinge, i.e., unable to transfer any forces or moments from one beam element to the other, a spike/discontinuity is observed in Figure 3.1a at $x/L = 0.20$. However, when a highly stiff connection is present at $x/L = 0.20$ (see Figure 3.1b), this spike transforms into a continuous line. This discovery forms the foundation of Assumption 4 stated below. Consequently, the mathematical formulation of the continuous beam can effectively describe a structure consisting of small, individual pontoons connected via semi-rigid connections.

Assumption 4 The connection exhibits a semi-rigid behavior, thereby enabling the accurate modeling of the beam as a continuous structure.

Material

The study examined four different materials, each with unique characteristics in density and Young's modulus, as shown in Table 3.1. These materials include HDPE, commonly used in building floating pontoons, and glass fiber reinforced polymer, GFRP, known for its incredible strength and water resistance [53]. The research also looked into two more flexible materials: expanded polystyrene, EPS, which is also used in floating structures [54], and Polyvinyl chloride, PVC, with a higher density than EPS but a similar Young's modulus.

When considering materials with densities lower than that of water, the beam's cross-section exhibits a solid configuration, as depicted in Figure 2.2a. Conversely, for denser materials like GFRP and PVC, a hollow cross-section is proposed. This design choice serves to reduce the overall density of the structure, making it buoyant. The hollow structure not only decreases its mass but also reduces the geometrical moment of inertia, as illustrated in Equation 2.19. Introducing a new parameter, denoted

Stiffness →	**HDPE**	**GFRP**
	$E_b = 12 \cdot 10^9$ N/m^2	$E_b = 35 \cdot 10^9$ N/m^2
	$\rho_b = 250$ kg/m^3	$\rho_b = 1250$ kg/m^3
	EPS	**PVC**
	$E_b = 6.5 \cdot 10^6$ N/m^2	$E_b = 52 \cdot 10^6$ N/m^2
	$\rho_b = 15$ kg/m^3	$\rho_b = 1400$ kg/m^3
	Density $\rightarrow$	

Table 3.1: Materials under investigation. Arrows indicate increasing magnitude.

as γ_I, is thus advantageous, as explained in Equation 3.1.

$$\gamma_I = \frac{I_{hollow}}{I_{solid}} \tag{3.1}$$

To determine the geometrical properties of the hollow structure, the wall thickness is defined as a percentage p_{h_b} of the input parameter h_b, which represents the thickness of the beam. This allows rewriting Equation 2.19 as follows:

$$I_{hollow} = \frac{h_b^3 W - [(1 - 2\frac{p_{h_b}}{100})h_b]^3 (1 - 2\frac{p_{h_b}}{100})W}{12} \tag{3.2}$$

Through algebraic manipulations, the parameter γ_I can be expressed as a function of the chosen percentage p_{h_b} as presented in Equation 3.3. By selecting a suitable value for p_{h_b} that ensures that the overall density of the structure remains below that of water, the corresponding γ_I value can be directly obtained, effectively reducing the geometrical moment of inertia. The reduced density $\rho_{b_{reduced}}$ can be calculated by dividing the reduced entire mass of the hollow structure by the entire volume, including the encapsulated air with a density of 1.2 kg/m^3. The value of γ_I can then be directly used in the numerical formulation of the problem to reduce the geometric moment of inertia of the beam. The obtained values for the two denser materials, GFRP and PVC, are summarized in Table 3.2.

$$\gamma_I = \frac{I_{hollow}}{I_{solid}} = 1 - (1 - 2\frac{p_{h_b}}{100})^4 \quad \rightarrow \quad I_{hollow} = \gamma_I I_{solid} \tag{3.3}$$

Material	p_{h_b} [%]	$\rho_{b_{reduced}}$ [kg/m^2]	γ_I [-]
GFRP	25	937.80	0.9375
PVC	20	896.43	0.8704

Table 3.2: Reduced density of the structure and parameter γ_I.

Length

The length of a beam is a crucial factor that significantly impacts a structure's behavior. If the length is too short, the structure will have rigid body characteristics, while an excessively long length will result in increased computational time due to the need for additional finite elements. To determine the appropriate length for the structure, the spacing between wind turbines was considered, as many envision OFPV to be deployed between existing offshore wind turbines [55]. Typically, wind turbines should be within the range of $(6-10)D_R$ apart [3], D_R representing the rotor diameter of a wind turbine. Since the average rotor diameter of offshore wind turbines in 2019-2020 was around 160 m [56], the distance between two turbines would range from 960 m to 1600 m. To accommodate four to seven structures of 200 m each within this distance and leave enough space for maintenance vessels, a total length of 200 m was selected for the OFPV structure.

Water Depth

The significance of water depth becomes evident when considering the applicability of the linear wave theory, as illustrated in Figure 2.4. For the linear wave theory to be valid and Assumption 2 to hold, the water depth must meet specific criteria. Additionally, deeper water leads to longer waves at the same frequency, as given by the dispersion relationship presented in Equation 2.35. Consequently, longer waves contribute to the formation of lengthier damping zones at the inlet of the mechanical modeling. This, in turn, necessitates a greater amount of computational time for the simulations. A detailed discussion on this topic can be found in subsection 3.1.2.

In this research, a water depth of 30 m was selected for the simulations. This value is aligned with the findings of Engebretsen et al. [57], who highlight that large areas in the Dutch North Sea exhibit a water depth of approximately 30 m. Additionally, it is worth noting that several offshore wind farms, such as Ten noorden van de Waddeneilanden and Doordewind, are planned to be constructed in similar water depths [58]. Considering the vision of integrating OFPV systems within existing or future wind farms, a water depth of 30 m was deemed appropriate for this study.

To sum up, in this study, a continuous beam spanning 200 meters and composed of four different materials, each with unique mechanical properties, has been modeled. Every parameter discussed is summarized in Table 3.3. As a result of the simplifications, a mechanical model with simplified components was created, as presented in subsection 3.1.3.

Parameter	Value
Length L_b	200 m
Joints	none
E_b, ρ_b	**HDPE**
	$E_b = 12 \cdot 10^9$ N/m^2, $\rho_b = 250.00$ kg/m^3
	GFRP
	$E_b = 35 \cdot 10^9$ N/m^2, $\rho_b = 937.80$ kg/m^3
	EPS
	$E_b = 6.5 \cdot 10^6$ N/m^2, $\rho_b = 15.00$ kg/m^3
	PVC
	$E_b = 52 \cdot 10^6$ N/m^2, $\rho_b = 896.43$ kg/m^3
Height h_b	$\{0.1$ m$, 0.2$ m$, 0.3$ m$, ..., 1.9$ m$, 2.0$ m$\}$
Water depth d	30 m

Table 3.3: Summary of the simplifications of the mechanical model.

3.1.2. Damping Zones

As highlighted in subsection 2.1.1, no reflections of waves are allowed at the vertical boundaries, as these would lead to an aggregation of energy in the system. Thus, two damping mechanisms are introduced to dissipate the energy from the system. To reduce the size of the fluid domain with respect to the x-direction, the Sommerfield boundary condition is used at the outlet damping zone as stated in Equation 3.4, which satisfies the boundary condition specified in Equation 2.6.

$$\vec{n} \cdot \nabla \phi = ik\phi \tag{3.4}$$

For the inlet damping zone, where the waves are generated, a different approach is selected compared to the outlet boundary. In a study conducted by Kim et al. [59], a numerical analysis was performed using a three-dimensional wave tank to investigate various damping schemes. The authors derived five different methods that influence the boundary conditions on the free surface at Γ_d. Additionally, they proposed different ramp functions to avoid abrupt changes in the boundary conditions at the beginning of the damping zone.

Among the five methods, method 4 exhibits constant energy within the computational domain, thereby eliminating wave reflections, and is thus used in this research. Consequently, the kinematic boundary (see Equation 2.7) condition at the inlet damping zone Γ_d can be expressed in the frequency domain as:

$$0 = -i\omega\kappa - \frac{\delta\phi}{\delta z} + \mu_1(\kappa - \kappa^*) + \frac{\mu_2}{g}(\phi - \phi^*) \tag{3.5}$$

The values κ^* and ϕ^* represent the reference values for a scenario where there is no structure affecting the ideal wave propagation, as stated in Equation 2.51 and Equation 2.50. These ideal values are enforced in the inlet damping zone. In terms of the ramp function, the authors recommended a gradual incline at the start of the ramp function. Hence, shape 2 is used as a ramp function. This leads to the following expression for the parameters μ_1 and μ_2.

$$\mu_1(x) = \begin{cases} \mu_0[1 - sin(\frac{\pi}{2}\frac{x}{L_d})] & \omega \leq 3.5, \\ \mu_0[1 - sin(\frac{\pi}{2}\frac{x}{2\lambda})] & \omega > 3.5 \end{cases} \tag{3.6}$$

$$\mu_2(x) = k\mu_1(x) \tag{3.7}$$

with x the spatial x-coordinate, L_d the length of Γ_d and μ_0 the target damping coefficient, which is defined as $\mu_0 = max(2.85, \frac{10.26}{\omega^{0.76}})$, based on the damping zone's optimal performance.

The duration of computational time is linked to the length of the inlet damping zone. Longer zones require more mesh points, resulting in increased computational time. Based on an analysis of previous wave data, it has been noted that Jonswap spectra do not consist of waves with an angular frequency below 0.2 rad/s, even during the most severe sea conditions. Historical wave data show that for the lowest peak frequency, neither the wave spectral density nor the amplitude spectrum rise before 0.2 rad/s as depicted in Figure 3.2. With a water depth of 30 m, a wavelength of 528 m corresponds to an angular frequency of 0.2 rad/s. Thus, to enable the generation of waves, the inlet damping zone should surpass the longest wave. The length of the inlet damping zone has been established as 550 m to facilitate this.

3.1.3. Numerical Formulation

Based on the assumptions made in the previous subsection 3.1.1 a simplified mechanical model can be drawn, as presented in Figure 3.3.

To solve the PDEs in the frequency domain, as presented in subsection 2.4.1, a FEM is used. As the name suggests, a FEM is a method that breaks down a complex system/domain into smaller pieces, so-called finite elements, which are connected at nodes. These finite elements and nodes make up the mesh. In the FEM, the behavior of the overall system is determined by analyzing the behavior of each individual element. To solve the PDEs that describe the system's behavior (known as the strong form), a transformation to the weak form, also known as the integral form, is necessary. The weak form offers an advantage by reducing the required level of differentiability of functions. For instance, in the case of the governing equation for the beam, the required level of differentiability is reduced from four to

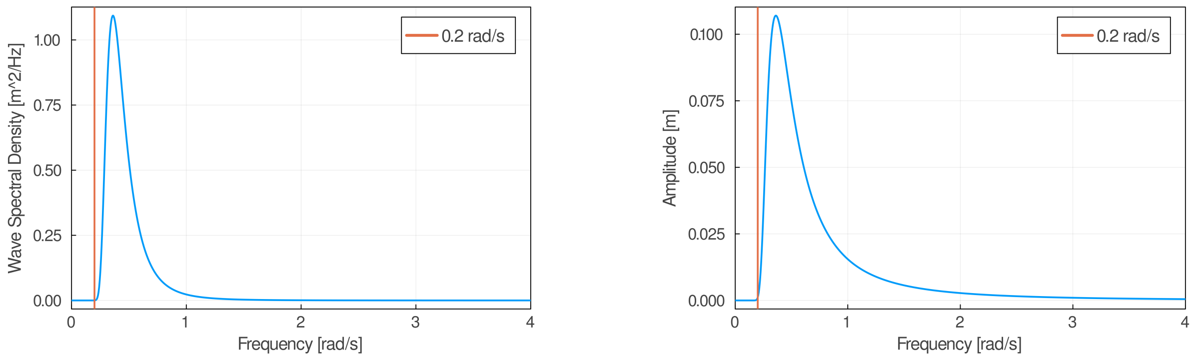

(a) Wave spectral density spectrum

(b) Amplitude spectrum

Figure 3.2: Wave spectral density and amplitude spectrum for the lowest peak frequency in historical data.

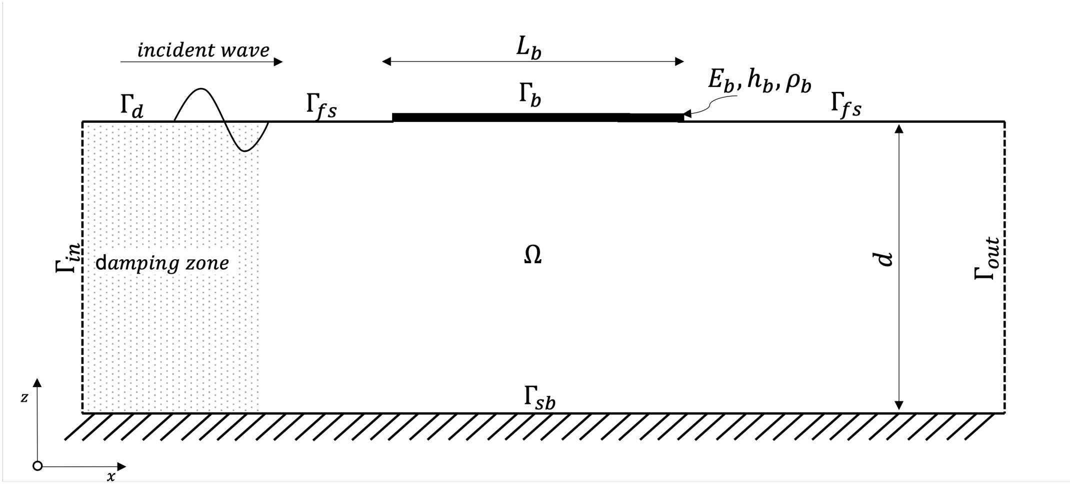

Figure 3.3: Simplified mechanical model with a continuous beam.

two. This can be seen in Equation 3.9. This transformation simplifies the mathematical representation. After the weak form is derived, the FEM process involves three main steps: discretization, interpolation, and assembly. Discretization divides the domain into finite elements. Interpolation approximates the behavior of each element based on known values at specific points. Assembly combines the individual element equations to form a system of equations representing the entire problem. This system of equations, represented in a matrix, is passed to a solver, which will solve the system directly or iteratively [60].

In the case of this research, a FEM model is written in the programming language *Julia*, using a FEM library called *Gridap*, which

> ”is a new Finite Element (FE) framework, exclusively written in the Julia programming language, for the numerical simulation of a wide range of mathematical models governed by partial differential equations (PDEs) [...] The main motivation behind Gridap is to find an improved balance between computational performance, user-experience, and work-flow productivity when working with FE libraries.” [61, p.1]

Weak and Discretized Form

To derive the weak form, a weight function w is multiplied with the Laplace equation and integrated over the entire domain Ω. Then, the resulting equation can be integrated by parts, which allows the substitution of the kinematic boundary conditions. Similarly, the dynamic boundary conditions for η and κ are multiplied with weight functions v and u, respectively, and integrated over the domain’s boundaries.

One can define the functional spaces $\mathcal{V}_\Omega$, $\mathcal{V}_{\Gamma_\eta}$, and $\mathcal{V}_{\Gamma_\kappa}$ for the domain Ω, the boundary Γ_b, and Γ_w, respectively, with $\Gamma_w = \Gamma_{fs} \cup \Gamma_d$, to find the solution for $[\phi, \eta, \kappa] \in \mathcal{V} \times \mathcal{V}_{\Gamma_\eta} \times \mathcal{V}_{\Gamma_\kappa}$ such that

$$B([\phi,\eta,\kappa],[w,v,u]) = l([w,v,u]) \quad \forall [w,v,u] \in \mathcal{V} \times \mathcal{V}_{\Gamma_\eta} \times \mathcal{V}_{\Gamma_\kappa} \tag{3.8}$$

with the bilinear form formulated as

$$\begin{aligned} B([\phi,\eta,\kappa],[w,v,u]) = &\int_\Omega (\nabla w \cdot \nabla \phi) d\Omega + \\ &\int_{\Gamma_{fs}} (\beta_{h_{fs}}(u + \alpha_{h_{fs}} w)(g\kappa - i\omega\phi) + i\omega w\kappa) d\Gamma_{fs} + \\ &\int_{\Gamma_d} (\beta_{h_{fs}}(u + \alpha_{h_{fs}} w)(g\kappa - i\omega\phi) + i\omega w\kappa - \mu_1 \kappa w - \frac{\mu_2}{g}\phi w) d\Gamma_d + \\ &\int_{\Gamma_b} (\eta v(-\omega^2 \frac{\rho_b h_b}{\rho_w} + g) + \Delta v \Delta \eta \frac{E_b I}{\rho_w} - i\omega v\phi + i\omega w\eta) d\Gamma_b + \\ &\int_{\Gamma_{out}} (ikw\phi) d\Gamma_{out} \end{aligned} \tag{3.9}$$

and the linear form as

$$\begin{aligned} l([w,v,u]) = &\int_{\Gamma_{in}} (w u_{in}) d\Gamma_{in} - \\ &\int_{\Gamma_d} (w\eta_d + \frac{1}{g} w\phi_d) d\Gamma_d \end{aligned} \tag{3.10}$$

with

$$\eta_d = \mu_1 \eta_{in} \quad \text{and} \quad \phi_d = \mu_2 \phi_{in} \tag{3.11}$$

and the stabilization terms

$$\beta_{h_{fs}} = 0.5 \quad \text{and} \quad \alpha_{h_{fs}} = -i\frac{\omega}{g}\frac{1-\beta_{h_{fs}}}{\beta_{h_{fs}}} \tag{3.12}$$

Equation 3.9 and Equation 3.10 do not only represent the weak form, but they already include the spatial discretization and interpolation steps. Due to the latter, stabilization terms that ensure the coercivity of the system are included in the formulation. For a detailed derivation of the weak form, the reader is referred to [62], and for further information regarding steps taken for spatial discretization and interpolation methods, to [37]. The two references also validate the model used in this research. Gridap constructs the numerical domain and FE space, where linear Lagrangian shape functions serve as reference elements, and assembles the affine finite element problem, which is ultimately solved. The complex paired functions for the beam's elevation η and slope η_x are obtained, which are then used to calculate the RAOs as introduced in subsection 2.4.2.

3.1.4. Stepsize of the Mesh and Frequency

As the stepsize of the mesh of the FEM, which should be fine enough for the shortest waves of the spectrum, and the stepsize of the frequency of the input spectrum are related, the derivation of the values for both is summarized in this section.

When deriving a one-sided frequency spectrum, such as the Jonswap spectrum, from a time signal, it is crucial to consider the following factors:

1. Number of frequencies and samples:
   To accurately represent all the frequencies from the original spectrum, the number of frequencies in the one-sided frequency spectrum derived from a time signal should be determined. This can be achieved by applying the equation as follows:

$$N_f = N_s/2 + 1 \tag{3.13}$$

   where N_f represents the number of frequencies in a frequency spectrum and N_s the total number of samples in the time signal.
2. Sample frequency and duration:
   The sample frequency f_s [Hz] determines how frequently the signal is sampled in the time domain. According to the Nyquist-Shannon sampling theorem [63], the f_s should be at least twice the maximum frequency present in the original frequency spectrum to avoid aliasing. This means that the sampling frequency should be chosen such that:

$$f_s \geq 2f_{max} \tag{3.14}$$

   where f_{max} is the highest frequency component in the frequency spectrum.

By considering a sampling frequency of 4 Hz, it is possible to calculate the maximum frequency that can be captured for the one-sided spectrum. This can be expressed as $f_{max} \leq 4/2 = 2$ Hz, or in angular frequency terms, $\omega_{max} = 12.57$ rad/s. Given that the time signal has a duration of 20 minutes and a sampling rate of 4 Hz, the total number of samples is determined to be 4800. The time period of 20 minutes was selected because it encompasses a duration in which every sinusoidal component of the wave spectrum has occurred. Utilizing the equation $N_f = N_s/2 + 1$, the number of frequencies can be computed, resulting in a value of 2401. Consequently, the step size of the frequency spectrum, represented as $d\omega$, can be calculated using the formula $d\omega = (\omega_{max} - \omega_0)/N_f$, where $\omega_0 = 0$ rad/s. The approximate value of $d\omega$ is determined to be 0.005 rad/s. If a longer time signal is chosen, it would result in an increase in the number of frequencies N_f leading to a higher computational demand. This methodology guarantees that the time signal accurately represents the frequency spectrum and vice versa. For a comprehensive overview, the corresponding values are summarized in Table 3.4.

Parameter	N_s [-]	f_s [Hz]	N_f [-]	$d\omega$ [rad/s]	ω_0 [rad/s]	ω_{max} [rad/s]
Value	4800	4	2401	≈0.005	0	12.57

Table 3.4: Overview of the parameters defining the frequency-time conversion.

The shortest wavelength present influences the determination of the FEM mesh size in the system. To accurately represent the shortest wavelength, the mesh size in the x-direction should be smaller than half of its length. Considering a maximum angular frequency of $\omega_{max} = 12.57$ rad/s, corresponding to a wavelength of approximately 0.38 m at a water depth of 30 m, the mesh size should ideally be less than 0.19 m. However, employing such a fine mesh would significantly increase computational time.

One potential solution is to increase the mesh size; however, this approach may not adequately capture short waves. Historical data has demonstrated that even spectra containing high peak frequencies exhibit limited wave activity at extremely high frequencies. The Jonswap spectral density and amplitude spectra of the historical datapoint with the highest peak frequency are depicted in Figure 3.4. One can see that the spectral density for high frequencies greater than 10 rad/s is close to 0. The amplitude spectrum exhibits values greater than 0 for high frequencies, but they are in the range of some millimeters. Thus, these can be neglected, leading to Assumption 5. Additionally, the RAOs of the structure in question display minimal responses at such frequencies as presented in chapter 4, see Assumption 6. Consequently, a mesh size of 0.25 m was deemed optimal.

Assumption 5 If high-frequency waves with frequencies above 10 rad/s are present in the wave amplitude spectrum, their amplitudes can be disregarded.

Assumption 6 The Response Amplitude Operator exhibits negligible or minimal response at high-frequency waves exceeding 10 rad/s.

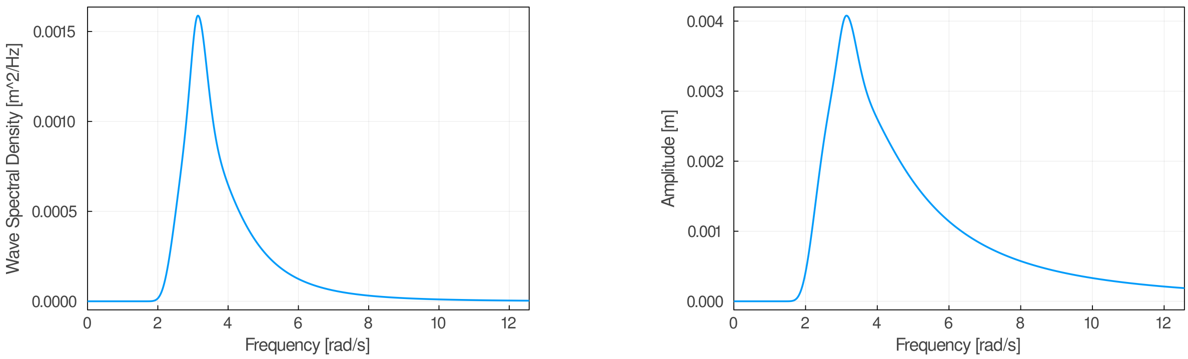

(a) Wave spectral density spectrum

(b) Amplitude spectrum

Figure 3.4: Wave spectral density and amplitude spectrum for the highest peak frequency in historical data.

3.1.5. Input Spectrum

To derive the RAOs for the amplitude and slope, as presented in equations 2.53 and 2.54, respectively, a constant input spectrum is utilized in the process. This input spectrum is illustrated in Figure 3.5. Adhering to the assumptions outlined in Assumption 5 and Assumption 6, only frequencies up to 10 rad/s are simulated. It is anticipated that higher frequency waves will not significantly impact the structural behavior. Additionally, as discussed in subsection 3.1.2, the lower bound for the angular frequency is determined by the length of the inlet damping zone, and it has been selected as 0.2 rad/s.

As presented in Table 3.4 N_f is set to 2401. However, simulating RAOs for such a large number of frequencies would lead to excessively long computational times. Therefore, a smaller number, specifically 211, was chosen for practical reasons, with the frequencies not evenly distributed across the entire range. The emphasis was placed on the lower frequencies, as the peaks of the wave spectra are typically found in this range. The objective was to capture the structural response in this critical region with greater accuracy, considering that even a small step $d\omega$ in frequency results in a significant change in amplitude. To expedite calculations for higher frequencies, the step size was increased. Interpolation techniques were employed to obtain the RAOs for the total number of frequencies, N_f, as required.

3.1.6. Resolution of the Tilt

With FEM analysis, one can assess the slope of a structure not only at the mesh nodes but also through interpolation in between. This implies that it is possible to obtain the slope at every point of interest, even with a mesh size of 0.25 m. Nonetheless, it is worth considering the suitable distance along the structure to average the slope.

To address this question, the tilt along the structure was examined under very rough sea conditions for various resolutions, as depicted in Figure 3.6 showing the first three meters for a 1 m thick beam made of HDPE. Different resolutions were considered, ranging from evaluating the tilt at every centimeter (resulting in a fine resolution) to averaging it over one meter and assuming it as constant (resulting in a coarse approximation).

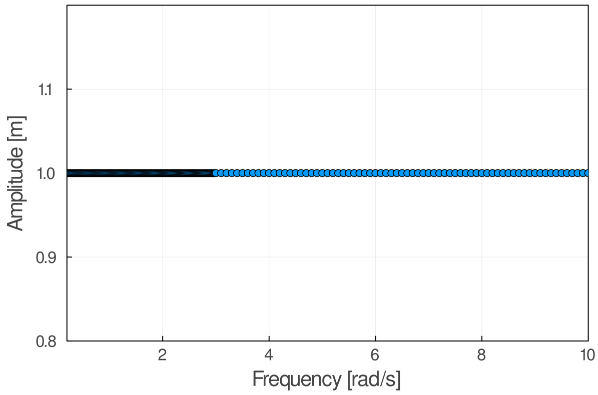

Figure 3.5: Constant Input Wave Spectrum. The higher density of markers for lower frequencies indicates a finer resolution.

To measure the approximation error, the MAE metrics was utilized. The comparison was made between the 1 m resolution and higher-resolution 1 cm data, which was considered the "correct" value. The MAE was calculated for each point on the structure, and it was found to be only 0.007°. The low error can be explained by the small changes in tilt observed on the y-axis in Figure 3.6. Assuming the tilt to be constant as the average between two points is a reasonable approximation.

This approach enables the assumption of a single constant value for the tilt of a PV module placed at every meter on the structure. By considering the average tilt between adjacent points, the complexity of the analysis is reduced while still providing a reasonable representation of the tilt variations along the structure.

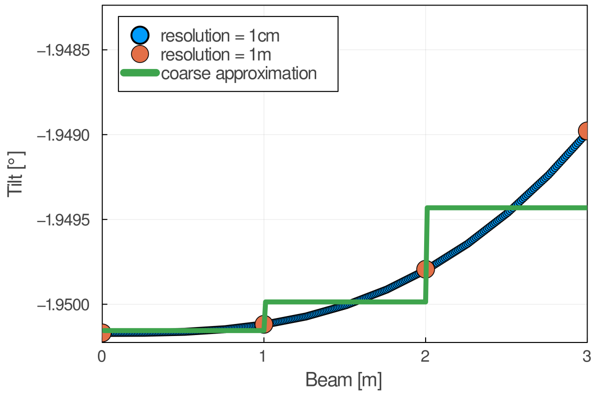

Figure 3.6: Approximation of the tilt for every meter along the structure.

3.2. Link between the Models

As discussed, the output of the FEM are the RAOs for the elevation and slope of the structure. To analyze the effects of the structure under specific sea conditions, the RAOs can be multiplied with a designated sea spectrum with random phases of each individual wave component, taking advantage of the system's linearity. The procedure for this multiplication is illustrated for the elevation of the first point on the structure in Figure 3.7. This approach enables the rapid analysis of the structure's response to various sea spectra, as there is no need to recalculate the RAOs each time.

To analyze the behavior of the structure under specific sea conditions, the response to a particular sea spectrum is obtained. To examine the temporal characteristics, the response is evaluated for all points on the structure and across all frequencies within the given sea spectrum. This process yields the time signal representing the structure's behavior. Specifically, the focus is on the structure's slope η_x. Hence, the analysis is performed exclusively for the slope component. The time signal of the slope behavior is obtained using Equation 3.15:

$$\eta_{x,i}(t) = \sum_{k=1}^{2401} A_{k,\eta_{x,i}} cos(\omega_{k,i} t + \epsilon_{k,i}) \quad \forall i \in \text{beam} \tag{3.15}$$

with A_{η_x} being the amplitude of the complex paired function η_x under certain sea conditions and the phaseshift ϵ.

Choosing a time signal duration that covers a sufficiently long period ensures that the structural response captures the full range of wave components in the wave spectrum. This approach provides a comprehensive understanding of the structural behavior without requiring further simulation time, as all relevant wave components have already been accounted for. In this research, the time signal was set to 20 minutes, as introduced in subsection 3.1.4.

The frequency-time conversion process yields a matrix as the result. The size of this matrix is determined by the number of rows, which corresponds to the total number of time instances considered, and by the number of columns representing the position on the beam. As the input to the optoelectrical is not the slope but the tilt θ, the following formula is applied.

$$\theta_i(t) = atan(\eta_{x,i}(t)) \tag{3.16}$$

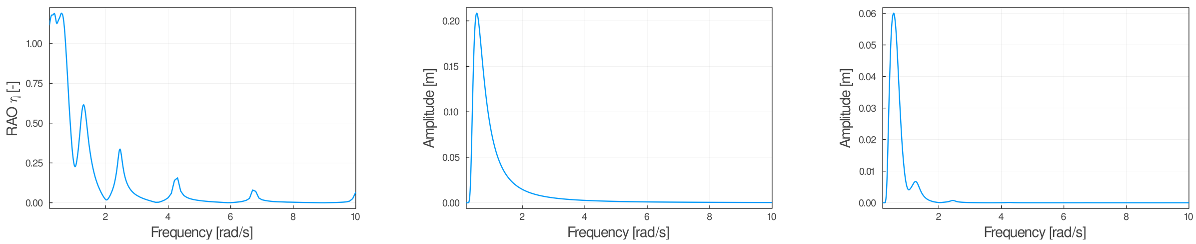

Figure 3.7: The obtained RAO for the elevation for the first point of the structure (left) is multiplied by the amplitude spectrum for a certain sea spectrum (center) and the obtained response to this certain spectrum (right).

3.3. Sea States

As discussed in section 3.2, the computational efficiency of calculating the response to a specific sea spectrum is advantageous since it eliminates the need to recalculate the RAOs for each individual sea spectrum. However, it is more meaningful to analyze the response under specific sea conditions that cover a range of sea spectra rather than analyzing individual sea spectra in isolation.

To classify these sea conditions, the Douglas sea scale [64] is used. The Douglas scale categorizes sea conditions into ten degrees, ranging from calm conditions with no waves to phenomenal conditions. However, this scale does not directly provide information about the significant wave height H_s and peak period T_p associated with a specific degree of sea condition. Rossi et al. [65] established a link between the Douglas scale and the significant wave height and peak period. Their work enables the determination of significant wave height and peak period corresponding to each degree of the Douglas scale.

In this research, four specific sea state conditions are considered, each representing a combination of significant wave height and peak period. A comprehensive overview of these sea state conditions, including kth percentiles derived from historical data, is presented in Table 3.5. The wave spectral density and amplitude spectra of the four sea states used in this research are depicted in Figure 3.8.

Douglas scale	sea state condition	H_s [m]	T_p [s]	ω_p [rad/s]	Percentile
3	slight	1.00	4.82	1.30	38th
4	moderate	2.00	6.11	1.03	80th
5	rough	3.00	7.59	0.83	95th
6	very rough	5.00	11.64	0.54	99th

Table 3.5: Sea state conditions and corresponding values for H_s, T_p and ω_p.

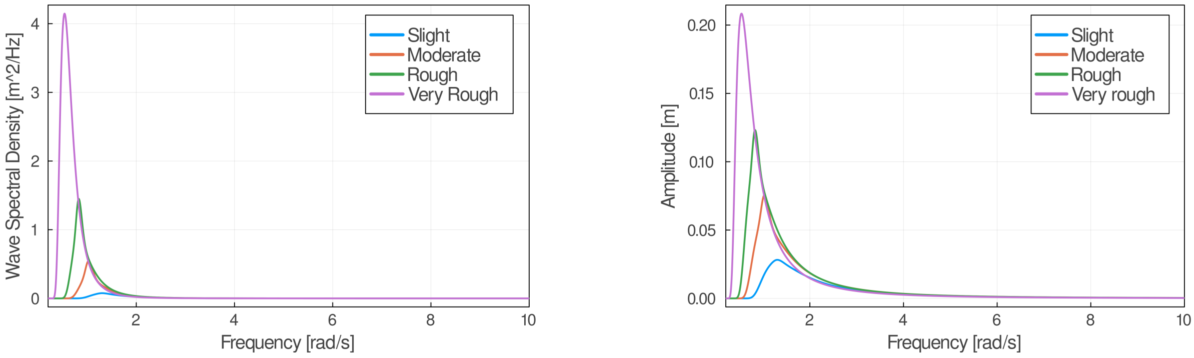

(a) Wave spectral density spectra.

(b) Amplitude spectra.

Figure 3.8: Wave spectral density and amplitude spectra for the four sea conditions as defined in Table 3.5.

3.4. Optoelectrical Model

Once the time series data for tilt measurements at each position along the beam is collected, the optoelectrical modeling phase begins. This is a critical step that involves examining the interconnections of the modules, particularly how the string is positioned on the floating structure in relation to wave propagation. A detailed exploration of this topic can be found in subsection 3.4.1. Additionally, the modeling process includes the comprehensive analysis of global irradiance and the careful selection of specific days for modeling purposes, as outlined in subsection 3.4.2. Furthermore, special attention is given to the distribution of irradiance along the structure, recognizing that modules connected within the same string experience different tilt angles at each time instant. This significant aspect is elucidated in subsection 3.4.3, providing valuable insights into the overall irradiance profile along the structure. The impact of varying irradiance levels on modules interconnected within the same string is also addressed in the discussion of power mismatch losses in subsection 3.4.4.

Assessing the efficiency of the system involves integrating the instantaneous power throughout a given day and month. This helps in comprehensively evaluating the DC electricity output of a specific string. A thorough investigation is needed to quantify the daily and monthly DC electricity losses due to instantaneous power mismatch losses. This is discussed in subsection 3.4.5.

The selection of a suitable PV module is an important aspect of the optoelectrical modeling process. In this context, a flexible PV module was chosen due to its unique characteristics, which facilitate its placement on a floating structure without impeding the structure's deformation. The flexibility of this chosen PV module ensures that the deformation of the floating structure is solely governed by its mechanical properties, without any additional resistance added by the modules themselves. The module's (GA-F200T) [66] characteristics under STC are presented in Table 3.6.

3.4.1. Orientation of the Modules' String on the Structure

The complications surrounding the orientation of the string connecting the modules in series in relation to the direction of wave propagation are best elucidated through Figure 3.9. This figure serves as a visual aid, providing a comprehensive depiction of the two extreme cases: when the string lies perpendicular or parallel to the direction of the waves.

Parameter	Value
Maximum Power P_{max} [$\mathrm{W_p}$]	200
Open Circuit Voltage V_{oc} [V]	20.8
Short Circuit Current I_{sc} [A]	12.05
Fillfactor FF [-]	0.7977
Voltage at maximum power point V_{mpp} [V]	17.6
Current at maximum power point I_{mpp} [A]	11.36
Number of cells N_S [-]	32
Ideality factor n [-]	1.2

Table 3.6: PV module's characteristics under STC.

The primary focus of this research lies in understanding and quantifying the power mismatch losses that arise due to variations in irradiance levels among series-connected modules. In the scenario where wave propagation is perpendicular to the string, as illustrated in Figure 3.9a from a side view perspective, it becomes evident that the modules interconnected by a single string experience identical tilts. This alignment ensures consistent irradiance levels across these modules.

However, when the direction of wave propagation aligns parallel to the string, a side-view perspective reveals that the modules along the string exhibit varying tilts, resulting in different irradiance levels. Consequently, this research assumes a parallel alignment between the direction of wave propagation and the string when addressing module and string orientation.

It is worth noting that when the direction of wave propagation and the string are at an angle, there is a gradual convergence that causes more and more modules to tilt in the same way. This trend continues until the modules are aligned perpendicularly in relation to the direction of wave propagation, eliminating any power mismatch losses. However, for the purposes of this research, only the extreme parallel case is being analyzed and investigated to maintain focus.

Within this research, the selection encompasses two distinct azimuths for the modules: South and East. In the case where the modules' azimuth is set to South, the wave dynamics will result in tilts facing either toward the South or the North, in accordance with the aforementioned assumption regarding wave propagation direction. Conversely, for the East orientation, the modules will undergo oscillations between East and West orientations. Notably, angles falling between these extreme orientations were not considered, as this study primarily concentrates on investigating the outcomes in such extreme scenarios. Oscillations leading to tilts oriented away from the sun, either during the morning or afternoon (East-West) or at noon (South-North), are anticipated to generate the most significant losses. This anticipation is attributed to the fact that such orientations result in diminished solar exposure during crucial periods of the day, adversely affecting the overall efficiency and performance.

3.4.2. Irradiance Modeling

In-plane Irradiance

In this research, the application of the Perez model has been chosen, and the modeling process has been executed using the open-source pvlib library [67] to obtain the in-plane irradiance. This comprehensive library offers a range of essential calculations as presented in section 2.2. The utilization of pvlib simplifies the procedure by providing matrix operations. Consequently, the tilt array obtained from the mechanical model, which captures all tilt variations during an hour, can be directly inputted. However, to pair this 2D array (rows represent the time signal, the columns the position on the beam) with the hourly weather data, it must be expanded to incorporate a third dimension representing the year's hours. This process necessitates substantial computational power due to the resulting large dataset.

Given the demanding computational requirements, this research adopts a focused approach, specifi-

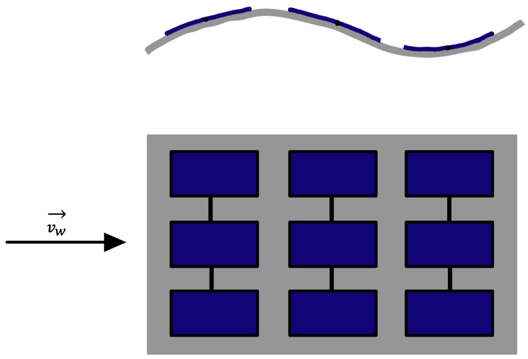

(a) Perpendicular

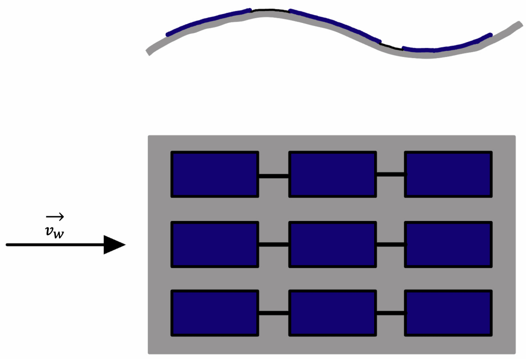

(b) Parallel

Figure 3.9: String's orientation in relation to the direction of wave propagation $\vec{v}_w$ in a top and side view.

cally targeting specific days throughout the year that illustrate the worst or extreme cases. To initiate the investigation, days were selected from both July and December, encompassing varying weather conditions, including sunny and cloudy/overcast days. These days serve as representative samples for in-depth analysis, allowing for a comprehensive understanding of the system's performance under different scenarios. For this study, it was assumed that the sea conditions would remain constant throughout the entire day, resulting in the consideration of the same tilt variations for every hour of that day.

Albedo

In accordance with Equation 2.25, the calculation of the diffuse radiation component requires the specification of an albedo coefficient. Indeed, in a perfectly calm sea, the water surface would exhibit mirror-like characteristics, reflecting a significant portion of the incident radiation [68]. However, it is important to acknowledge that such ideal conditions are rarely encountered in real-world scenarios. The albedo is linked to the prevailing sea state and the behavior of the water surface itself. In this research, for the sake of simplification and practicality, a constant value for the albedo coefficient is assumed. A value of 0.06 is selected for the albedo, as supported by observations from previous studies [69].

Weather Data

Weather data were obtained from a meteorological weather station near the coast, with coordinates 53°24'42.0"N, 6°11'57.0"E. The specific data of interest, namely the GHI, was provided by KNMI - Koninklijk Nederlands Meteorologisch Instituut [70]. Applying the BRL model [71], which facilitates a decomposition approach, the components of DNI and DHI are derived from the weather data. Despite the weather data not originating from an offshore location, it is presumed that the irradiance profiles observed along the coast are comparable to those encountered in offshore settings, providing a reasonable representation.

The selection of days for analysis in this study was based on two primary factors: the clearness index and the ratio of DNI to GHI. The clearness index ranges from 0 to 1, with 0 representing a completely overcast sky and 1 indicating perfect sunshine [72]. The ratio of DNI to GHI is considered due to its significance in Equation 2.20. When the direct component of irradiance constitutes a substantial proportion of the overall GHI, any change in module tilt results in a more pronounced variation of the cosine term in Equation 2.21. This, in turn, affects the in-plane irradiance more significantly. Conversely, if the direct irradiance component is considerably lower and DHI higher, changes in the cosine term do not lead to substantial variances in in-plane irradiance. Based on these, the irradiance profiles of the chosen days for July and December are presented in Figure 3.10 and Figure 3.11, respectively. All three components of Equation 2.26 are illustrated in the irradiance profiles. The selected sunny day in December exhibited a relatively low average clearness index. This was primarily due to increasing cloud cover in the afternoon, resulting in a higher proportion of diffused irradiance, as seen in Figure 3.11a. It should be noted that no sunnier days in December were found within the available dataset.

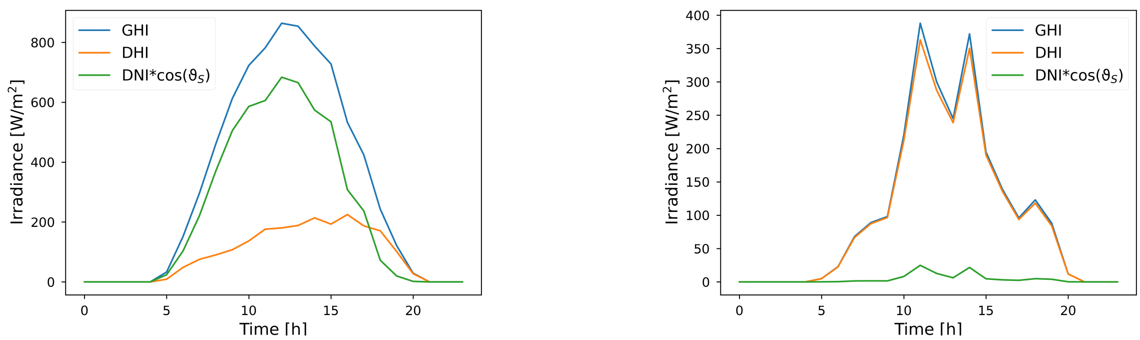

(a) Sunny, average clearness index of 0.7.

(b) Cloudy, average clearness index of 0.2.

Figure 3.10: Irradiance profiles of a sunny and cloudy day in July.

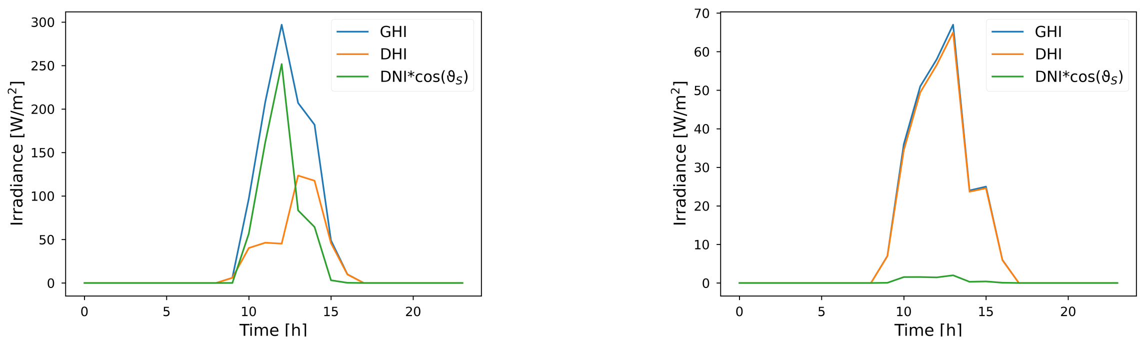

(a) Sunny, average clearness index of 0.5.

(b) Cloudy, average clearness index of 0.2.

Figure 3.11: Irradiance profiles of a sunny and cloudy day in December.

3.4.3. Irradiance Distribution

The irradiance modeling process, as detailed in subsection 3.4.2, yields the irradiance values for each point along the beam at every second throughout the specified day. To provide a visual representation, Figure 3.12a showcases the in-plane irradiance along the beam for two randomly chosen seconds, namely t1 and t2. This illustration considers specific parameters: a 1-meter thick beam constructed from HDPE, a sunny July day facing Eastwards, and a calm sea state.

Observing the graph, it is apparent that the irradiance levels vary along the structure for both t1 and t2. However, what distinguishes these instances is the range, specifically the difference between the maximum and minimum irradiance values and the magnitudes of the irradiance level itself. It can be visualized in a histogram in Figure 3.12b. One can see the difference in the range and magnitude for these two morning-time instances. It is important to note that the range and magnitude vary for each time instance throughout the day. This range becomes crucial in calculating the power mismatch losses, as outlined in subsection 3.4.4.

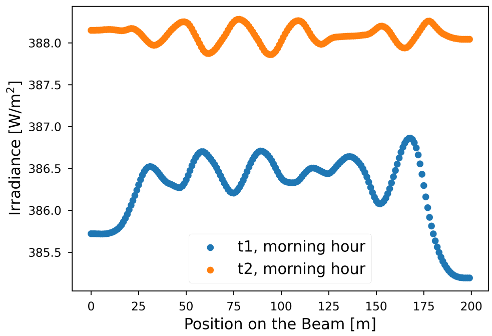

(a) Irradiance at each point.

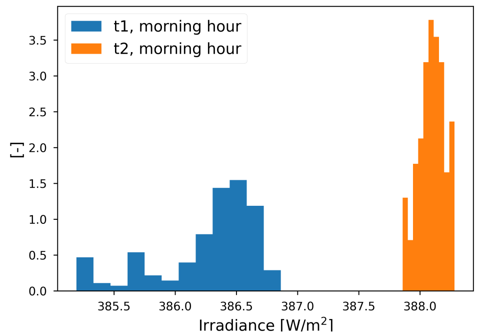

(b) Irradiance distributions.

Figure 3.12: Irradiance at each point for two morning time instances (left) and the irradiance distributions for these time instances (right).

3.4.4. Power Mismatch Losses

In the domain of PV strings, power mismatch losses can arise when series-connected PV modules receive varying levels of irradiance. This discrepancy in irradiance can be attributed to factors such as shading, soiling, module degradation, or structural irregularities. In the context of this research, the mismatch arises from the different tilts and orientations of the series-connected modules positioned along the structure. A graphical representation is provided in Figure 3.13. The figure serves as an example where four PV modules connected in series experience different irradiance levels.

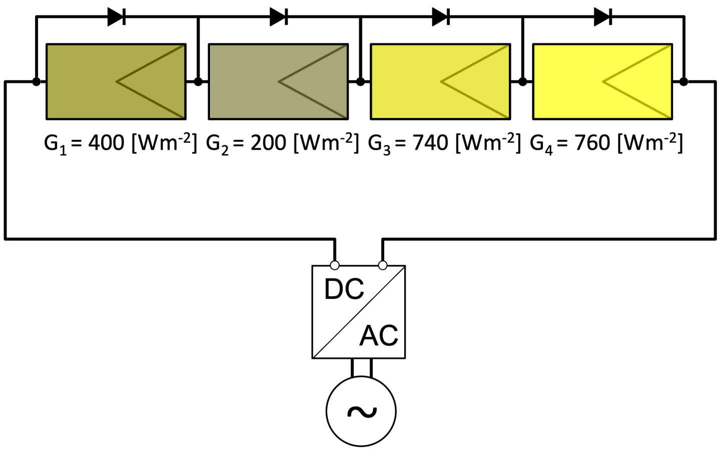

Figure 3.13: Different irradiance levels on 4 PV modules connected in series to one inverter [73].

To address the power mismatch losses, it is assumed that all modules within a string are connected to a single inverter with one maximum power point tracker (MPPT), resulting in a power output denoted as P_{sys}. P_{sys} is calculated by approximating the current-voltage (I-V) curve of the series-connected modules. The case for four modules is shown in Figure 3.15. By approximating the I-V curve of PV modules with different irradiance levels and hence different maximum power points with rectangles, one can find the pair (V_i, I_i) that outputs the highest power for the entire string. By comparing this value to the ideal case P_{ideal}, where each module has its own micro MPPT and operates at its maximum power point, the induced power losses P_{losses} can be calculated using the equation expressed in Equation 3.17. A schematic for P_{ideal} is shown in Figure 3.14.

$$P_{losses} = (1 - \frac{P_{sys}}{P_{ideal}}) \cdot 100\% \tag{3.17}$$

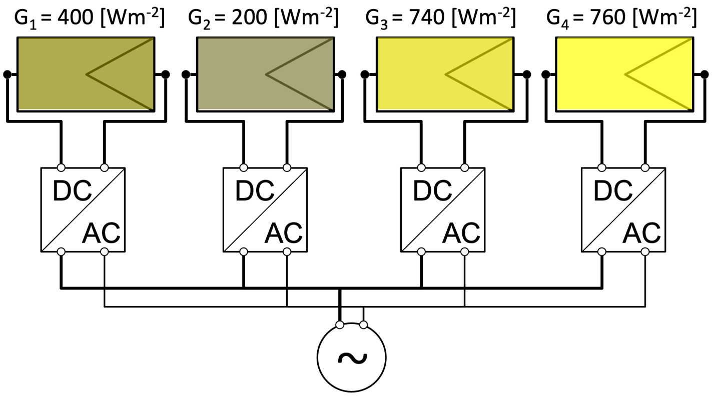

Figure 3.14: Different irradiance levels on four PV modules connected to micro inverters with their own MPPTs [73].

Moreover, it is assumed that all modules along the structure are connected in series without the presence of sub-strings. This configuration represents the most extreme case, where even the modules positioned at the edges of the structure — points that experience significant variations in tilts and consequently different irradiance levels (as observed in Figure 3.12a) — are connected to the string. Introducing sub-strings, such as excluding the first and last several meters of the structure, would result in reduced losses. However, for the purpose of worst-case analysis, it is assumed that every point along the structure is included in the calculation.

To determine the power output of each individual module based on the irradiance level, Equation 2.29 is applied to each module along the structure, considering the characteristics of the module as stated in Table 3.6. As the module temperature was not specifically modeled in this research for practical reasons, Equation 2.32 was not utilized. Because the focus of this research is solely on comparing systems with and without micro MPPTs rather than comparing inland and offshore PV systems, the enhanced performance of modules due to lower temperatures, which would be expected in an offshore installation, is disregarded. Thus, the temperature effect is neglected.

It is important to note that, for further analysis, only sunny days are considered. A closer examination of the power mismatch losses distribution reveals that, for every second within an hour, the induced losses on cloudy days are approximately one order of magnitude lower than those on sunny days. This observation is depicted in Figure 3.16. Once again, this illustration considers specific parameters, including a 1-meter thick beam made of HDPE, a day in July, an Eastward-facing azimuth for the string, and a calm sea state.

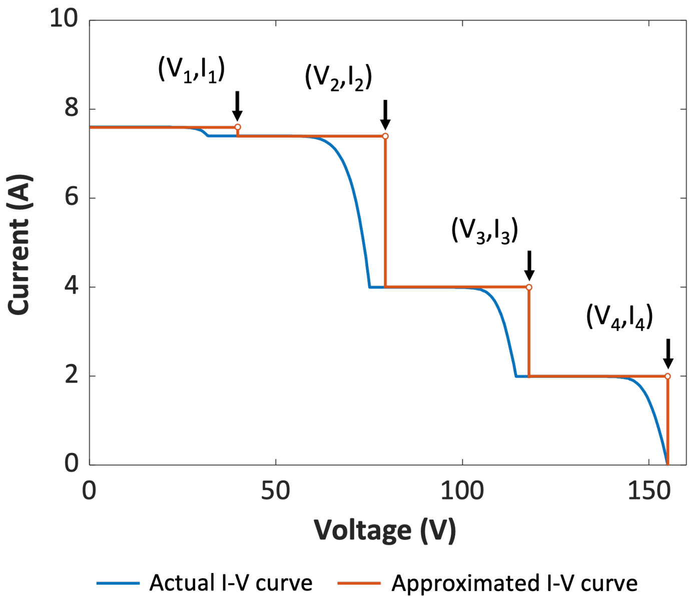

Figure 3.15: Approximation of the I-V curve of in-series connected modules [73].

This power mismatch loss discrepancy can be partially explained by the absence of DNI during overcast weather conditions. As mentioned earlier, DNI is multiplied by the cosine term in Equation 2.21, which is sensitive to changes in module tilt. However, when DNI is low, the impact of this cosine term change is less pronounced. On the other hand, the diffused and reflected in-plane irradiance components are not as sensitive to changes in module tilt. Therefore, further analysis excludes cloudy days due to their comparatively lower induced power mismatch losses.

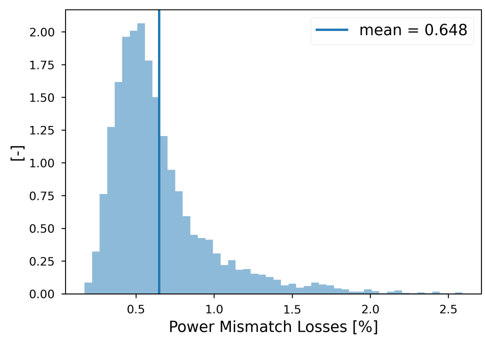

(a) Sunny

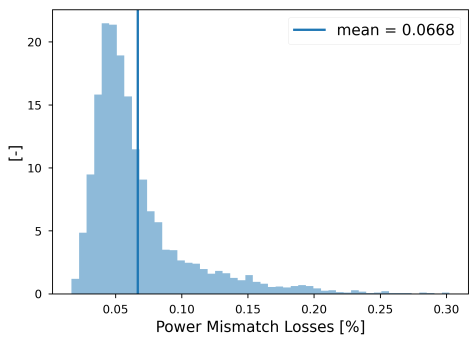

(b) Cloudy

Figure 3.16: Power mismatch losses during 8-9 in the morning for a sunny and cloudy day in July.

3.4.5. Daily and Monthly DC Electricity Losses

Taking the instantaneous power output and integrating it over the entire day, neglecting any other losses, yields the daily DC electricity output. This is highlighted in Equation 3.18.

$$E_{DC,sys,day} = \sum_{h=1}^{24} \sum_{t=1}^{3600} P_{sys,h,t} \cdot 1[s] \tag{3.18}$$

For the most promising material choices, the monthly DC electricity output is calculated for December and July according to Equation 3.19.

$$E_{DC,sys,month} = \sum_{d=1}^{N_d} E_{DC,sys,d} \tag{3.19}$$

with N_d the number of days in July and December, respectively.

One can also compare the total electricity losses caused by power mismatch losses over an entire period by applying Equation 3.20.

$$E_{DC,losses} = (1 - \frac{E_{DC,sys}}{E_{DC,ideal}}) \cdot 100\% \tag{3.20}$$

with $E_{DC,ideal}$ the integrated P_{ideal} over the period of interest.

At this point, a summary of all the remaining parameters and the resulting number of combinations to be analyzed is given in Table 3.7. Furthermore, a flowchart containing the main steps, which were thoroughly described in this chapter is presented in Figure 3.17.

Thickness [m]	Material	Sea State	String's Azimuth	Month	**Combinations**
$0.1, 0.2, ..., 1.9, 2.0$	HDPE	Slight	South	July	**1280**
	GFRP	Moderate	East	December	
	EPS	Rough			
	PVC	Very rough			

Table 3.7: Possible combinations of parameters to be analyzed.

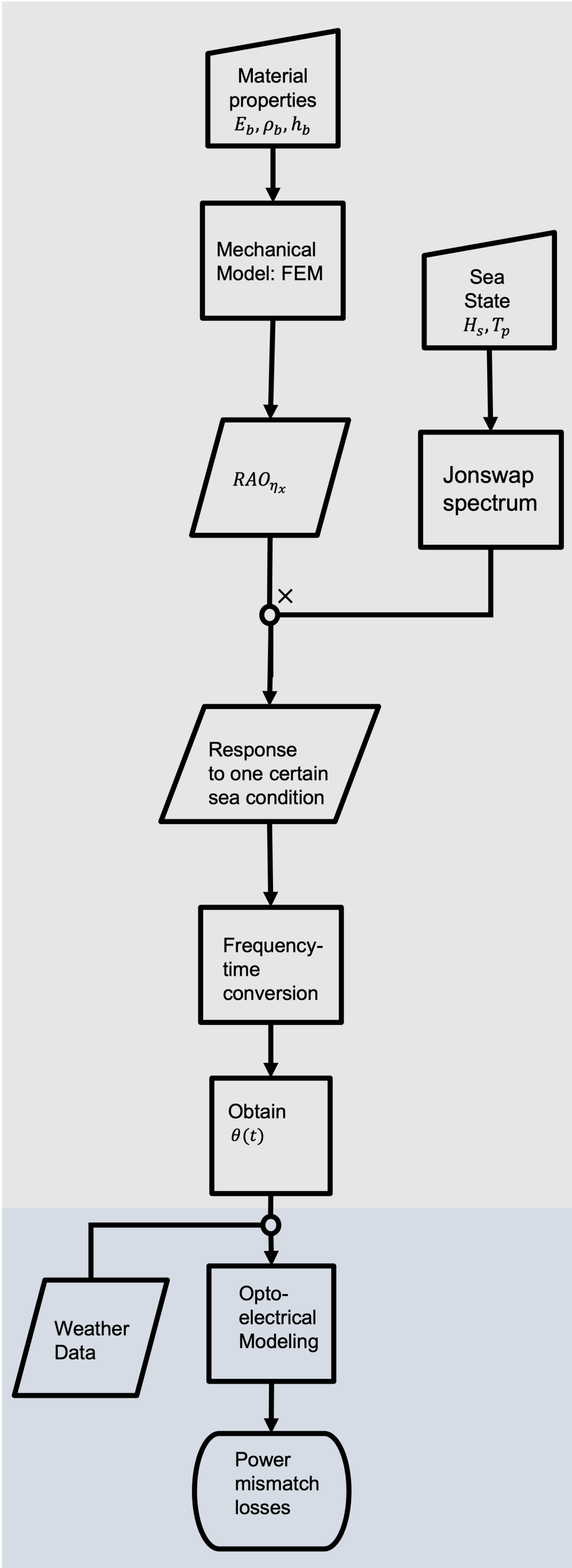

Figure 3.17: Flowchart of the entire process. The grey background includes every step described in sections 3.1 to 3.3, and the light blue background refers to section 3.4.

4 Mechanical Results and Discussion

This chapter is dedicated to the presentation and analysis of the outputs derived from the mechanical modeling. The mechanical response of the structure, considering the variation in parameters, holds significant importance. As such, the RAOs of η are provided in section 4.1. It is worth noting that the RAOs of η_x play a crucial role in the subsequent optoelectrical modeling; however, due to their limited visual representation value, they have been included in the appendix.

Additionally, the chapter delves into examining the tilt variation along the structure under specific sea conditions in section 4.2. By analyzing the tilt profiles, valuable insights are gained regarding the behavior and performance of the structure in response to the prevailing sea condition.

4.1. Response Amplitude Operators

The RAO depends on both frequency and position along the structure, giving rise to a three-dimensional representation as illustrated in Figure 4.1a. This plot serves as a visual demonstration and focuses on the characteristics of a 1.5m thick structure made of HDPE. In addition, two isolines are depicted to provide further insights. The first isoline represents a constant frequency of 1 rad/s (approximately corresponding to a wavelength of 60m), showcased in Figure 4.1b. The second isoline corresponds to the front end of the structure, as depicted in Figure 4.1c.

The findings obtained in this study are consistent with the existing literature, as it is commonly observed that the RAO values exceed unity, indicating that the elevation of the structure surpasses the amplitude of the incident waves. Additionally, the wavy pattern depicted in Figure 4.1b illustrates that different points along the structure experience varying oscillation amplitudes. The isoline displayed in Figure 4.1b effectively represents the contour or boundary line of the maximum deflection, providing valuable insights into the structural response under specific frequency conditions. Figure 4.1c offers valuable insights into the frequencies at which the structure, or more specifically, a specific point on the structure, is excited. Notably, at higher frequencies, minimal excitation is observed, except for isolated spikes. This phenomenon can be attributed to the excitation occurring near or at multiples of the eigenfrequencies, as described in Equation 2.55. However, it is important to note that the amplitude of the amplification diminishes as the number of multiples increases.

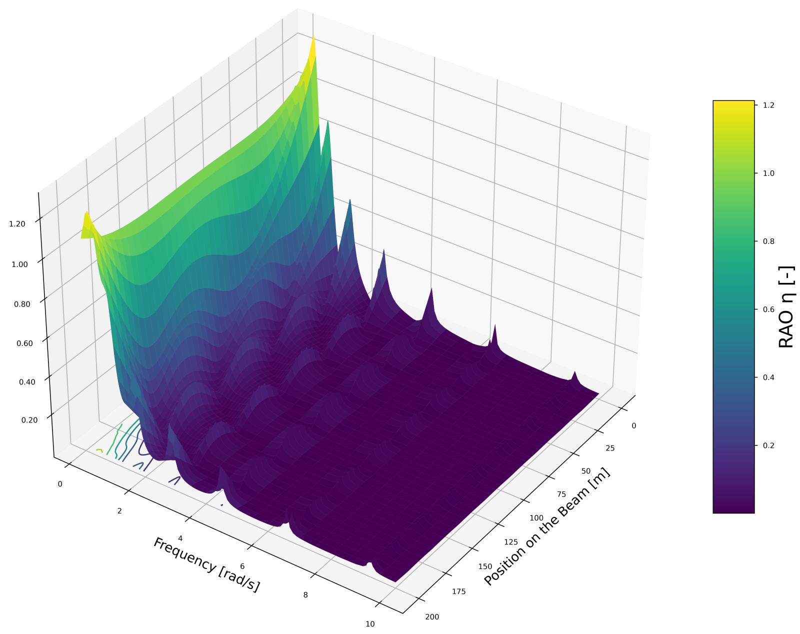

(a) 3D RAO for all frequencies and positions on the beam.

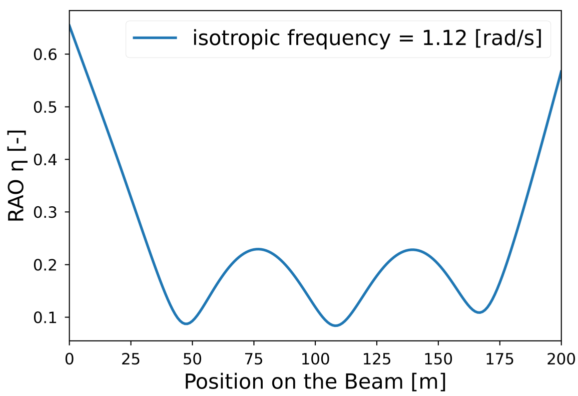

(b) Isotropic frequency.

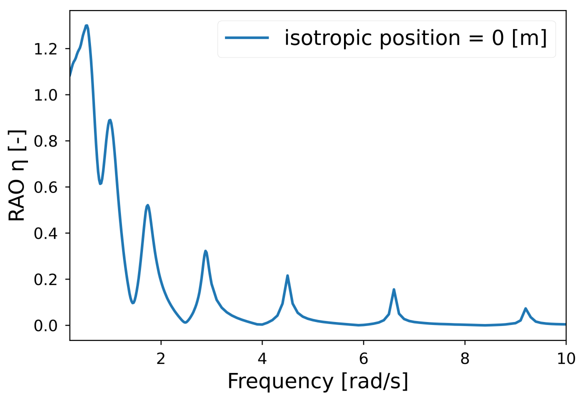

(c) Isotropic position.

Figure 4.1: 3D RAO for a 1.5 thick RAO made of HDPE, including two isolines.

In order to facilitate a thorough comparison of the RAOs, contour plots are utilized as the visual representation. Specifically, the focus is on HDPE and EPS materials due to their distinct Young's modulus magnitudes. RAOs for other thicknesses and materials can be found in section A.1. Within the context of HDPE, Figure 4.2 showcases four contour plots, each corresponding to a different thickness. A notable observation is that the response along the structure at high frequencies tends to be minimal across all thicknesses. However, for thicker beams, a narrower range of frequencies and points experience lower excitation. This phenomenon can be attributed to the increased strength and resistance to deformation exhibited by thicker structures, resulting in fewer points being excited. It is worth mentioning that despite increasing the thickness, the contour plots indicate that responses greater than unity persist, particularly at the edges. This suggests that even with a significantly thick structure, complete stabilization along the entire length remains unreachable.

In contrast, EPS exhibits distinct behavior, as demonstrated in Figure 4.3. A thin EPS structure displays high excitations across a broader frequency range. Notably, within each color area, there are no noticeable gradients or peaks, indicating that every point along the structure oscillates with a similar amplitude. As the thickness of the EPS structure increases, the material gains strength, resulting in smaller areas of intense excitation that shift towards longer waves/lower frequencies.

Interestingly, the pattern observed in the 1m thick EPS structure (Figure 4.3c) closely resembles that of the 0.1m thick beam made of HDPE. This can be attributed to the relationship described by Equation 2.55, where an increase in EPS thickness leads to a shift in the Eigenfrequencies (ω_n). When the EPS thickness is set to 1m and the HDPE one to 0.1m, the ratio of $\omega_n(HDPE)/\omega_n(EPS)$ is approximately 1, indicating that the Eigenfrequencies lie in close proximity. Consequently, a similar behavior is observed. It is worth noting that increasing the thickness can effectively compensate for the material's inherent lack of strength.

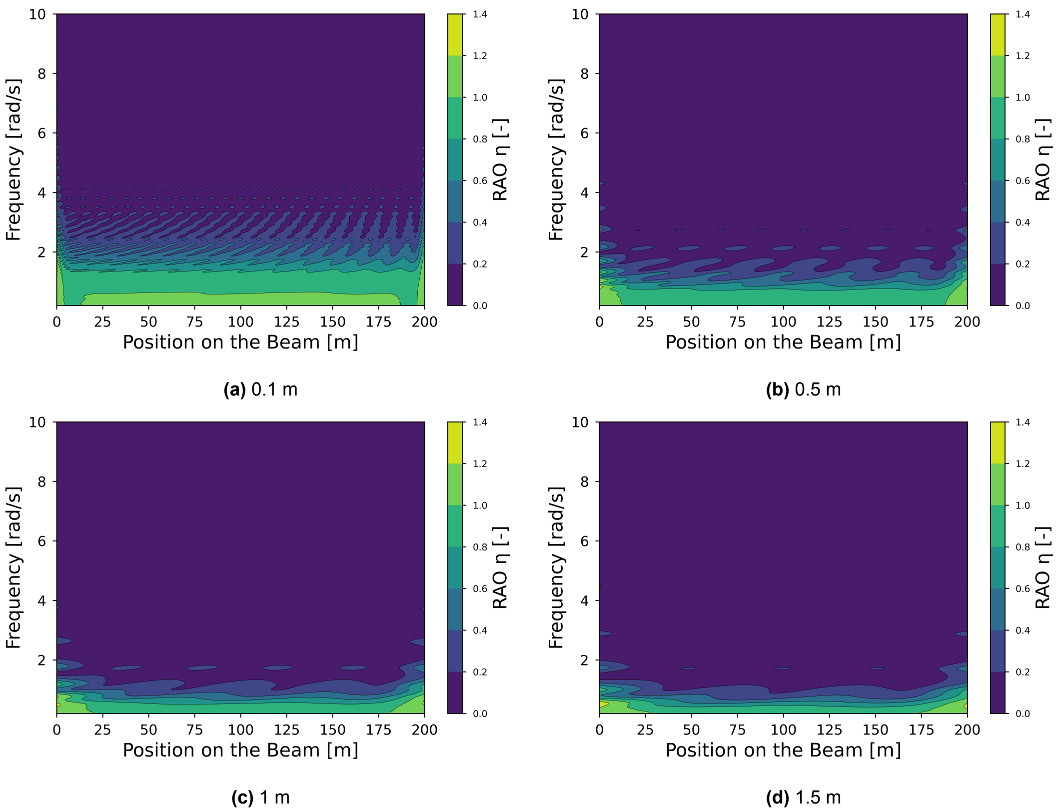

(a) 0.1 m

(b) 0.5 m

(c) 1 m

(d) 1.5 m

Figure 4.2: Contour plots of RAOs for HDPE and different thicknesses of the beam.

Increasing the thickness of the material can indeed result in enhanced structural strength, enabling it to withstand wave-induced forces more effectively and reducing structural excitation. However, as demonstrated in chapter 5, an increase in thickness does not directly lead to improved performance in terms of less power mismatch losses within the PV string. This aspect will be thoroughly explored

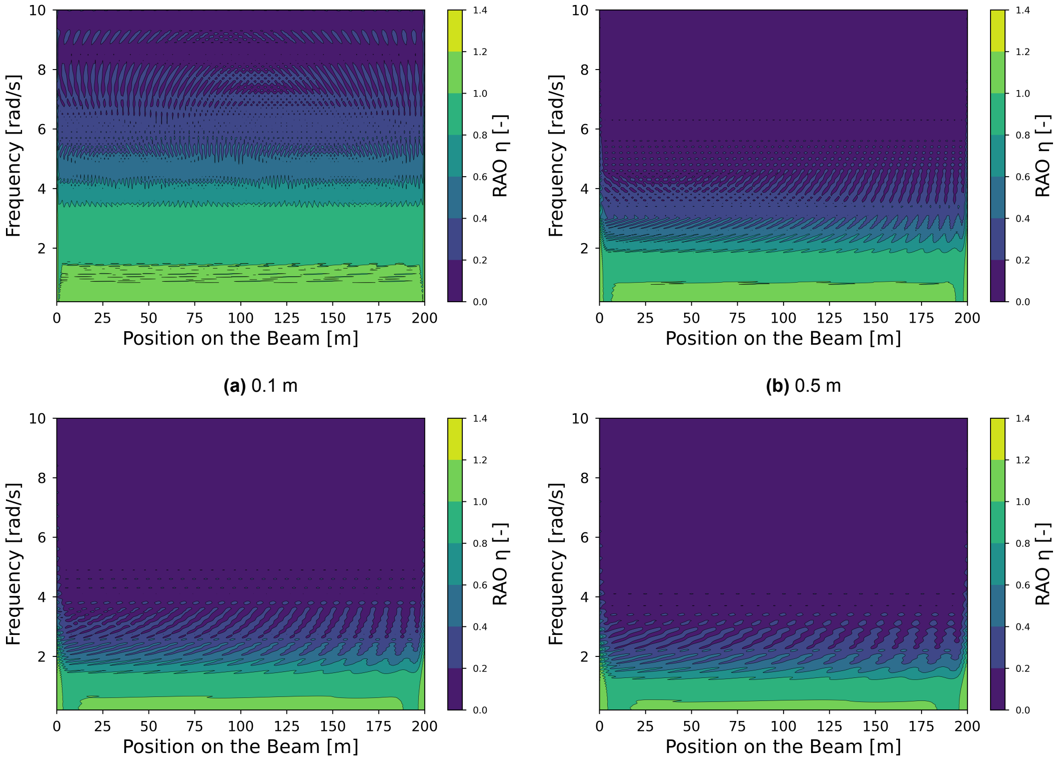

(a) 0.1 m
(b) 0.5 m
(c) 1 m
(d) 1.5 m

Figure 4.3: Contour plots of RAOs for EPS and different thicknesses of the beam.

and analyzed in the relevant chapter. It is important to note that the primary focus of this thesis is not the optimization of a floating structure's mechanical or dynamic performance but rather the reduction of power mismatch losses. Consequently, when optimizing for the latter objective, a comprehensive approach is required, incorporating both the analysis of RAOs and optoelectrical modeling.

4.2. Tilt Variation

The tilt signal, resulting from the superposition of multiple sinusoidal waves, exhibits a normal distribution of tilt at each point along the beam, as discussed in subsection 2.5.1. This characteristic allows for creating a three-dimensional plot, visually representing the normal distribution of tilt for each point on the beam. In this case, the focus is on a 1.5m HDPE beam, similar to the context discussed in section 4.1. However, it is important to note that the tilt time signal depends on the selected sea state, contrasting with the analysis of RAOs. For the purpose of illustration, both calm and rough sea states are depicted in Figure 4.4 and Figure 4.5, respectively.

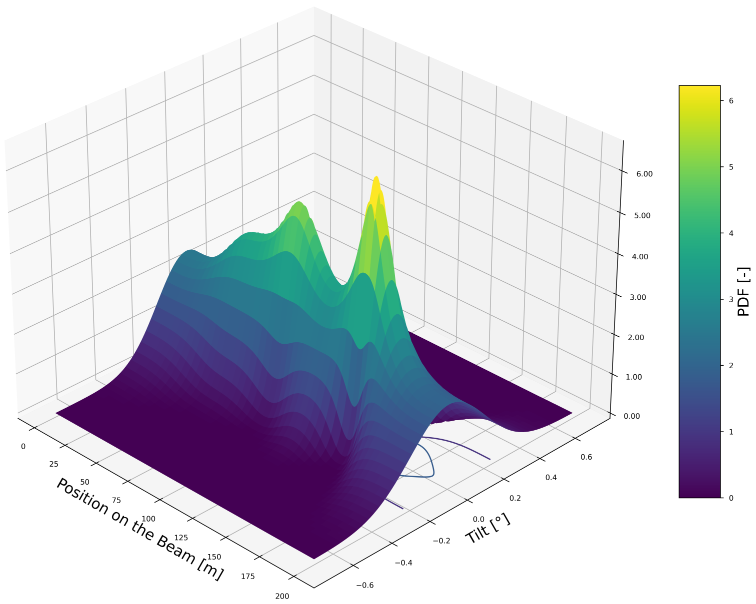

Figure 4.4: Normal distributions of the tilt for each point on a 1.5m thick structure made of HDPE under calm sea conditions.

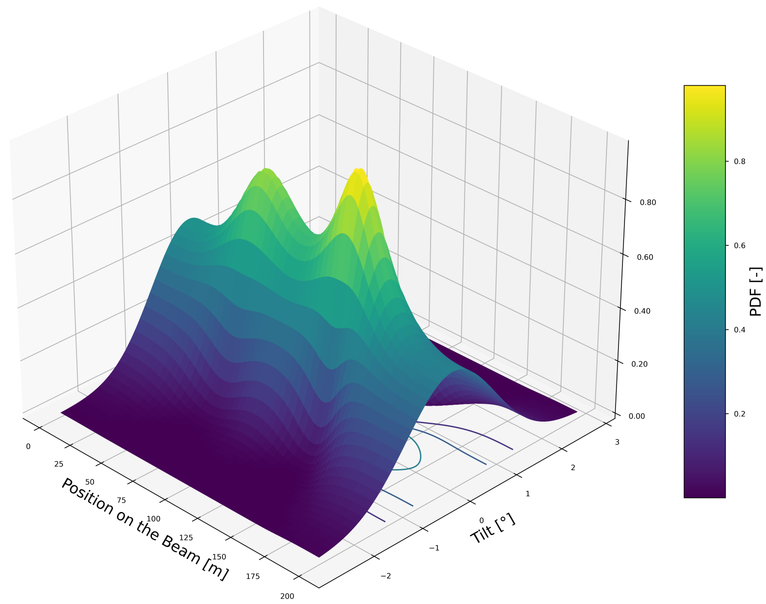

Figure 4.5: Normal distributions of the tilt for each point on a 1.5m thick structure made of HDPE under rough sea conditions.

The brightness of color in the tilt distributions directly corresponds to the peak magnitude, indicating a higher peak with a narrower distribution and smaller standard deviation. Consequently, points experiencing higher peaks will have reduced variations in tilt. In a calm sea state, the y-axis range demonstrates minimal tilts due to the limited excitation caused by calm conditions. Conversely, a rough sea state amplifies the range of tilts, as larger and higher waves generate a wider spectrum of tilt values.

The peaks observed in the graphs signify points with minimal oscillation, while the valleys, for instance, at the edges, exhibit a greater variation in tilts, aligning with the RAOs presented in section 4.1. Since the mean of the normal distributions is centered at 0, the crucial parameter to consider is the standard deviation. Consequently, plotting only the standard deviation as a function of spatial position and increased beam thickness becomes suitable. For the HDPE material under calm and rough sea states, this relationship is depicted in Figure 4.6 and Figure 4.7, respectively. The entire set of plots for all sea states and material is depicted in Appendix A.

The analysis of Figure 4.6 and Figure 4.7 reveals that an increase in thickness results in a reduction in the standard deviation of the tilt. However, it is important to note that this reduction is not linear. In other words, increasing the thickness from 0.1m to 0.2m leads to a more significant decrease in the standard deviation than the reduction observed when increasing the thickness from 1.0m to 1.1m. This non-linear relationship indicates that the impact of thickness on reducing tilt variability diminishes as the thickness increases. A similar trend can be observed in the case of a rough sea state in Figure 4.7,

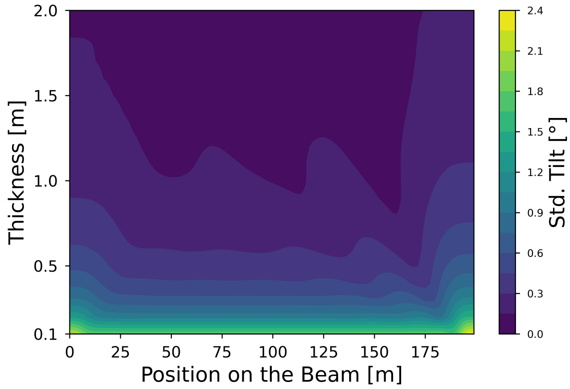

Figure 4.6: Standard deviation of the tilt for varying thicknesses for a structure made of HDPE under calm sea conditions.

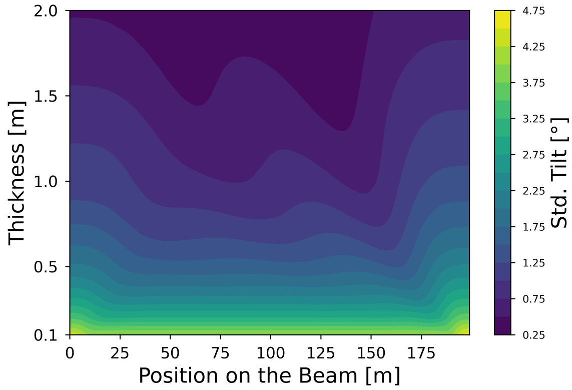

Figure 4.7: Standard deviation of the tilt for varying thicknesses for a structure made of HDPE under rough sea conditions.

although the effect is shifted to thicker structures.

An additional observation can be made by envisioning horizontal lines to represent beams of specific thicknesses across the tilt standard deviation plots. These horizontal lines intersect different color areas, which correspond to the previously mentioned peaks and valleys in the three-dimensional tilt distribution plots. This finding suggests that certain points within the structure exhibit greater stability in terms of tilt oscillations compared to their neighboring points. In other words, there are regions along the beam where the tilts are more consistent and less prone to variation.

It is crucial to avoid making incorrect assumptions based solely on tilt variation, particularly in relation to potential power mismatch losses. The tilt distributions depicted are statistical representations encompassing all the tilts experienced by each point on the structure. However, these distributions do not provide information about the specific tilt values at any given time instance along the structure. Power mismatch can only be expected if the tilts at different points along the structure differ at a particular time instance.

Nevertheless, fewer variations in tilt indicate that the points on the structure tend to be more stable around a tilt angle of 0 degrees. This stability offers an opportunity to optimize, for instance, the mounting tilt of the PV module in a manner that avoids negative tilts, changing the orientation as explained in subsection 3.4.1. By strategically adjusting the mounting tilt, it is possible to minimize the occurrence of unfavorable tilt angles, ultimately improving the overall power output of an individual PV module.

5
Optoelectrical Results and Discussion

As expounded upon in the preceding chapter, various parameters can influence the power mismatch along the string. Consequently, the impact of an individual parameter is scrutinized in the following sub-chapters while holding the remaining parameters constant. Additionally, the thickness is varied in each section, complementing the analysis of the respective parameter. Consequently, in each section, the effects of the specific parameter and the influence of thickness can be observed. Including the variation of the thickness offers a broader perspective on the impact of the respective parameter. It enables the observation of how changes in thickness can amplify or mitigate the effects of the parameter under investigation.

First, the analysis focuses on the impact of sea state on power mismatch losses and daily energy losses, as discussed in section 5.1. Next, the influence of seasons is presented in section 5.2. Subsequently, the effects of changing the string's orientation are examined. This is followed by the evaluation of the material choice in section 5.4. Finally, monthly energy losses are calculated and presented based on the most promising materials in section 5.5. It is important to note that the individual sections solely serve as plot examples. The Appendix B must be referred to for a comprehensive list of various combinations and effects.

5.1. Effect of the Sea State

Four distinct sea states were subjected to analysis, wherein each sea state pertains to the excitation of the beam at different frequencies and amplitudes. Consequently, variations in behavior can be anticipated based on the differing sea states. The distribution of daily power mismatch losses, pertaining to a sunny day in July, across different thicknesses and sea states, is illustrated in Figure 5.1. The parameters that remain constant and unchanging for this particular scenario are the orientation of the modules, which is Eastward-facing, and the chosen material, which is HDPE.

After analyzing the data, a few conclusions can be drawn. Firstly, when the thickness of the beam is increased, the power mismatch losses decrease. This can be attributed to the fact that a thicker beam enhances the beam's bending stiffness. Consequently, the beam will not deform as much, resulting in fewer module tilt variations. However, it is worth noting that at some point, the power mismatch loss increases as the beam's thickness is increased. For example, during the sea state ”very rough”, the sea spectrum may align with or be close to one of the beam's eigenfrequencies. Under these circumstances, a beam with a thickness of 1.6m will display increased power mismatch losses. Similarly, for different sea states, the optimal beam thickness may vary.

Secondly, it can be observed that the lowest losses occur during a slight sea state. It is worth noting that a rough sea does not always result in higher power mismatch losses. Interestingly, thinner beams experience lower power mismatch losses in a very rough sea compared to a moderate one. This is due to the unique dynamics caused by frequency and amplitude shifts in the waves. When the sea is

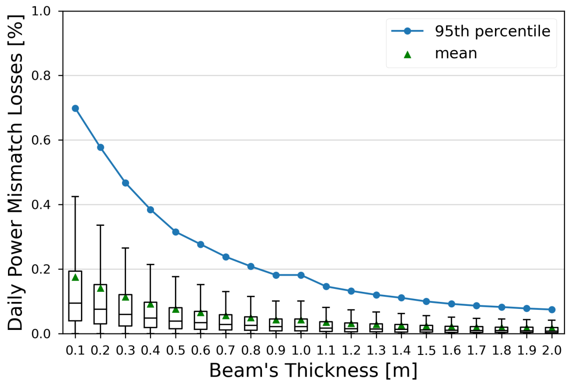

(a) Slight

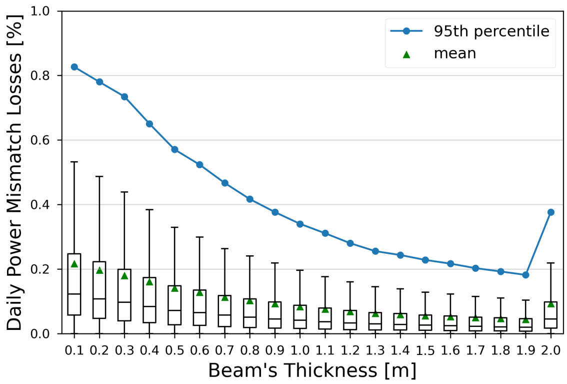

(b) Moderate

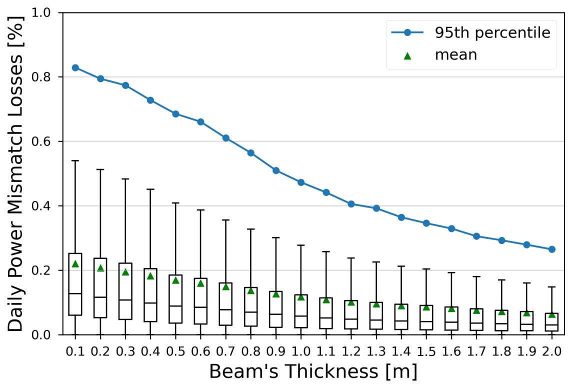

(c) Rough

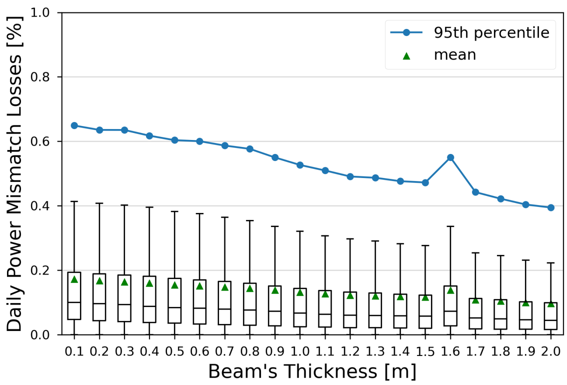

(d) Very rough

Figure 5.1: Effect of the sea state: Power mismatch losses during a sunny day in July for different sea states. String's azimuth is East. Box plots exclude the outliers. 95th percentile and mean include the outliers.

rough, the Jonswap spectrum shifts towards lower frequencies, making longer and higher waves more dominant. They greatly affect the structure's deformation. In this scenario, a thin structure provides minimal resistance to the waves' pressure, allowing it to conform to their shapes with ease. Therefore, all modules along the string tilt similarly, aligning with the prevailing wave conditions at each time instant.

Thirdly, it is worth noting that the behavior of the 95th percentile curve differs for varying beam thicknesses in different sea states. Specifically, during slight and moderate sea states, the slope of the curve is not constant as the beam thickness increases. As the beam thickness surpasses a certain threshold (excluding the small spike observed at 1m for the slight sea state), the slope of the curve starts to flatten. This observation implies that increasing the beam's thickness beyond a certain point does not result in proportional reductions in power mismatch losses. In other words, the benefits obtained from increasing the thickness reach a saturation point, beyond which further increases do not yield significant additional decreases in power mismatch losses.

Finally, it is important to address the significant presence of outliers in the box plots representing the daily power mismatch losses. To illustrate this, consider Figure 5.2, which displays the hourly power mismatch losses during a sunny day in July for a 0.1 thick beam made of HDPE, oriented towards the East, under slight sea conditions. During the early morning hours, the power mismatch experiences substantial variations caused by the extremely low sun's elevation and azimuth angle, leading to a greater range of the boxplot for 5 am. These hourly data points, when aggregated to create the dataset for the daily box plot, contribute to the appearance of outliers when examining the data points over the entire day.

By analyzing Figure 5.2, a distinct trend can be observed: the most negligible power mismatch losses

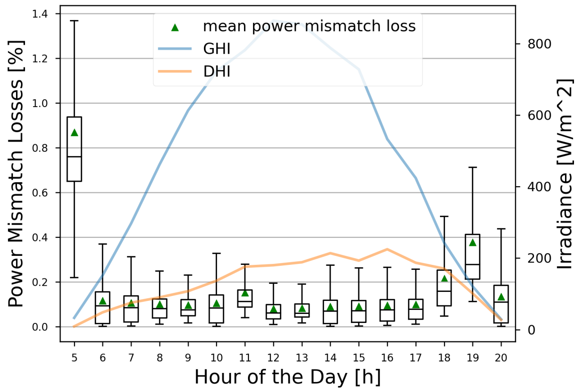

Figure 5.2: Effect of the sea state: Hourly power mismatch and energy losses for a 0.1m thick beam during a sunny day in July, facing East, slight sea state and HDPE.

occur at noon. This timeframe aligns with the highest levels of irradiance, which means that power mismatch losses during this time could result in a genuine loss of electricity. On the other hand, during the morning hours, when irradiance levels are low, the power mismatch losses do not lead to significant electricity loss. Based on these findings, one can reconsider the implications of Figure 5.1 from a different angle. When calculating the overall energy yield for an entire day, it is essential to consider the positive impact of low power mismatch losses during high irradiance periods. Therefore, one can look at the total daily DC electricity output for the ideal case, the real case, and the applied losses for different sea states in Figure 5.3.

Analyzing the orange curves, which represent the ideal scenarios where each module has its own MPPT tracker, in Figure 5.3, it can be observed that the curve raises in the beginning and remains relatively constant as the thickness increases, except for occasional spikes. An increase in thickness results in reduced variations in tilt. This lack of tilt variations affects the ideal electricity output since each module operates independently at its maximum power point and does not experience many unfavorable tilts facing away from the sun. It also impacts the actual production (blue curves in Figure 5.3) because modules along the structure experience similar tilts at any given time, in addition to the effects described in relation to the orange curve. The blue and orange curves converge, meaning that the daily electricity losses caused by power mismatch losses decrease, as can be seen by the blue dots in Figure 5.3.

Comparing Figure 5.1 and Figure 5.3, interesting patterns emerge that illustrate the relationship between power mismatch losses and total daily energy losses. Both figures show similar trends, indicating a correlation between the two metrics. Furthermore, electricity losses tend to increase when the sea spectra closely match the structure's natural frequencies, which increases the variability of power mismatch losses. However, it is essential to highlight the differences in the severity of the power mismatch losses. Despite the relatively high values of the 95^{th} percentile and the average values constantly above 0.1% and reaching 0.8%, the total energy losses remain below 0.16% for all beam thicknesses and sea states. They even go down below 0.02%. This discrepancy is due to the influence of factors mentioned above: high irradiances and minimal power mismatch at certain times: When solar irradiance is highest, the effects of power mismatch losses are effectively mitigated at this time of day. The combination of abundant solar radiation and minimal mismatch ensures that the resulting electricity losses are relatively low. As a result, total electricity losses remain below the 0.16% threshold throughout the day across a range of irradiance and sea state conditions. Hence, it is crucial to minimize power mismatch losses in times of high levels of irradiance to avoid high daily energy losses.

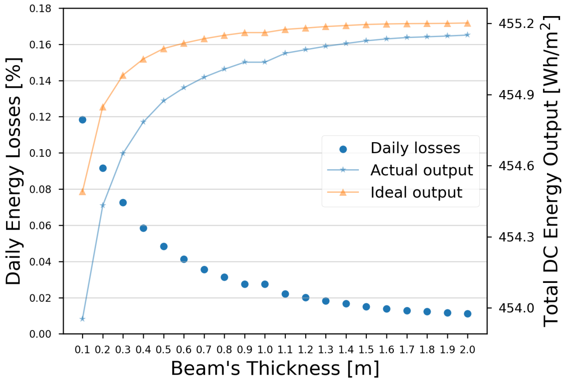

(a) Slight

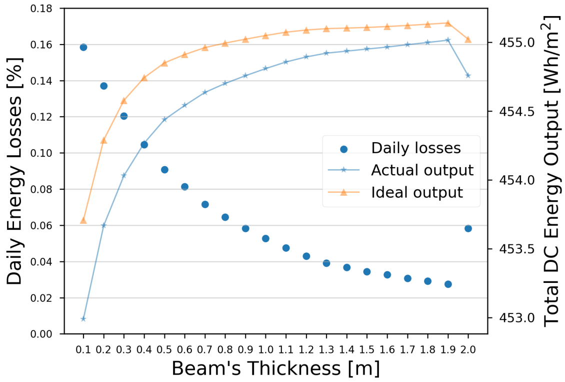

(b) Moderate

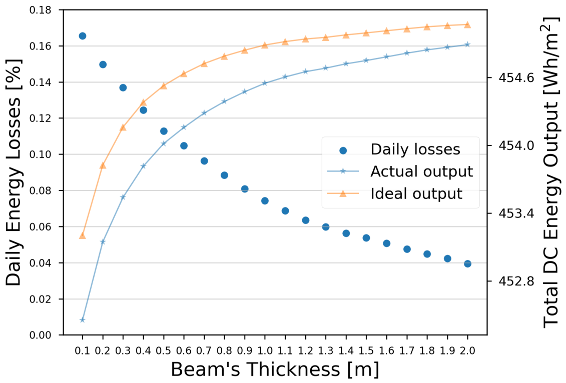

(c) Rough

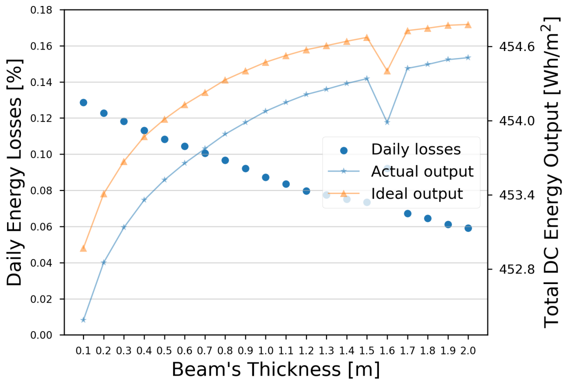

(d) Very rough

Figure 5.3: Effect of the sea state: DC energy losses due to power mismatch losses as a function of the beam's thickness during a sunny day in July for different sea states. String's azimuth is East.

5.2. Seasonal Effects

This section explores the impact of seasonal changes on system performance, specifically comparing the performance of a sunny day in July with that of a sunny day in December. The analysis maintains consistency by keeping certain parameters constant, such as a slight sea state, the use of HDPE material, and East orientation. Figure 5.4 shows the daily energy losses for summer and winter.

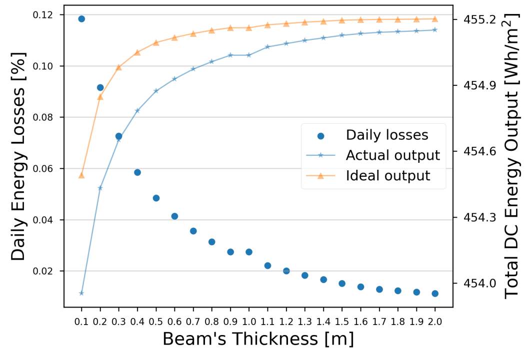

(a) Summer

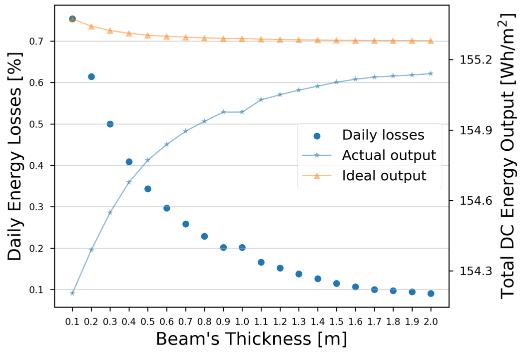

(b) Winter

Figure 5.4: Seasonal effects: Daily energy losses in summer and winter for varying thickness, facing East and slight sea conditions. Be aware of the difference in y-axis levels.

The two graphs demonstrate a comparable reduction in electricity losses as the structure's thickness increases. The structural dynamics primarily influence the curve representing the energy losses due to power mismatch. However, the orange curves, which represent the daily DC electricity output in the case of individual MPPTs, display a different trend for thin beams.

For thin beams, the oscillating nature of the structure leads to increased sensitivity to tilt variations, particularly during summer. This is evident in the orange curve shown in Figure 5.4a, where it rises sharply and then flattens out. In contrast, the orange curve in Figure 5.4b remains relatively constant. The reason for this discrepancy lies in the sun's position throughout the day. During summer, the oscillations of a thin structure often result in the modules facing away from the sun in the late morning when the sun is still in the East and irradiance is relatively high. Furthermore, the sun's azimuth aligns with the orientation of the string.

Increasing the thickness of the structure enhances the stability of the individual modules, reducing the angles at which they face away from the sun. Consequently, this increases the overall DC electricity output of the individual modules. Similar effects can be observed in the early evening. In winter, however, as the sun rises in the southeast at an angle to the string's orientation, the reduced oscillations due to increased thickness between the East and West orientations do not have a similar effect. This is because the sun's beams already hit the modules at an angle.

Furthermore, there is a difference in the order of magnitude between the two seasons. In the summer, electricity losses due to power mismatch lead up to 0.12%, while in winter, they are six times higher, ranging up to 0.75% for the worst-case beam thickness. This discrepancy can be attributed to the lower position of the sun on the horizon during winter. Even minor tilt changes during winter can cause significant variations in in-plane irradiance due to the sun's lower position, in contrast to when the sun is positioned higher on the horizon during summer.

5.3. Effect of the Orientation

This section examines the effect of the modules' azimuth, specifically the azimuth of the strings, on power mismatch losses and daily energy losses. The material under analysis is HDPE. The chosen sea state for evaluation is "slight" and the month is December.

First, refer to the daily energy output and losses illustrated in Figure 5.5. It can be observed that the curves exhibit similar shapes. For both orientations, the total electricity production in the ideal scenario reaches similar values. Additionally, the daily energy losses decrease as the thickness increases. However, there are differences in the magnitudes of these energy losses. Specifically, for the East orientation, the losses lie roughly between 0.10% and 0.75%. In contrast, for the South orientation, the losses are between 0.4% and 2.50%, roughly half of the former.

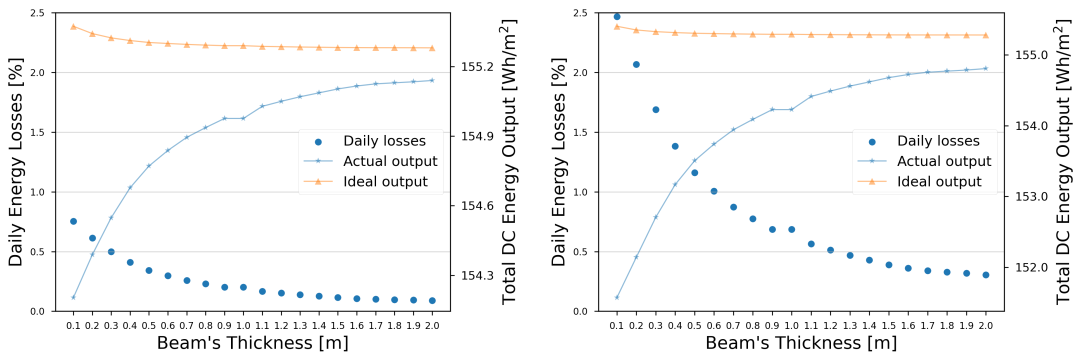

(a) East

(b) South

Figure 5.5: Effect of the orientation: Daily energy losses for various thicknesses for two different azimuths in winter for slight sea conditions.

In order to understand the cause for the difference, Figure 5.6 shows the hourly energy losses, the power mismatch distribution along the string and the irradiance during the day for a 0.1m thick beam under slight sea conditions in winter.

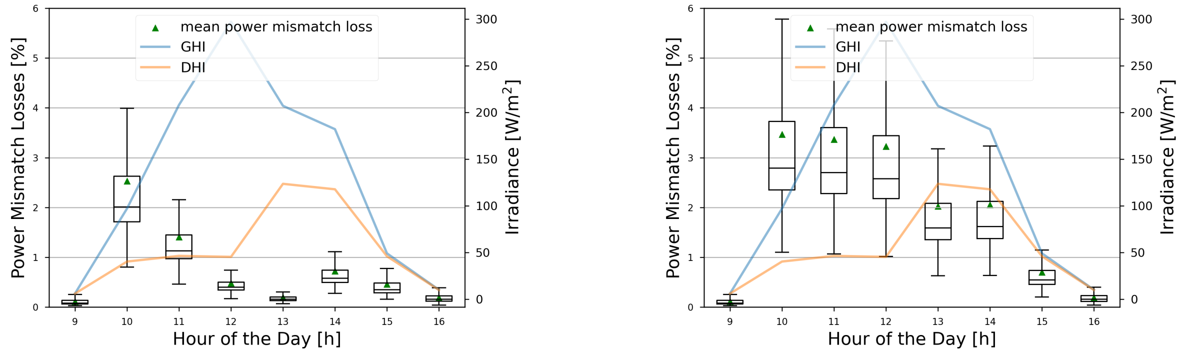

(a) East **(b)** South

Figure 5.6: Effect of the Orientation: Hourly power mismatch and energy losses for a 0.1m thick beam, slight sea state, and HDPE in winter.

The East orientation exhibits broader distributions of power mismatch losses across a greater number of daylight hours compared to the South orientation. Notably, these hours correspond to periods of relatively high irradiance levels. While the power mismatch losses for the South configurations are more pronounced during the peak noon hours when irradiance levels are at their highest, these losses are offset by compensatory gains experienced during the late morning and afternoon periods. It is important to note, however, that the chosen day exhibited slight overcast conditions during the afternoon, as indicated by the GHI and DHI data. Consequently, the losses induced during noon could potentially be compensated to a greater extent in the afternoon, thereby leading to reduced daily energy losses.

The effect of orientation on power mismatch losses is expected to be less significant during summer due to the higher position of the sun and the occurrence of higher irradiance levels in the afternoon and evening. This enables the possibility of recovering losses incurred in the morning/evening by compensating through gains made during the midday period and vice versa. The findings in Figure 5.7 support this anticipation, as the losses due to power mismatch for both orientations do not exceed 0.12%.

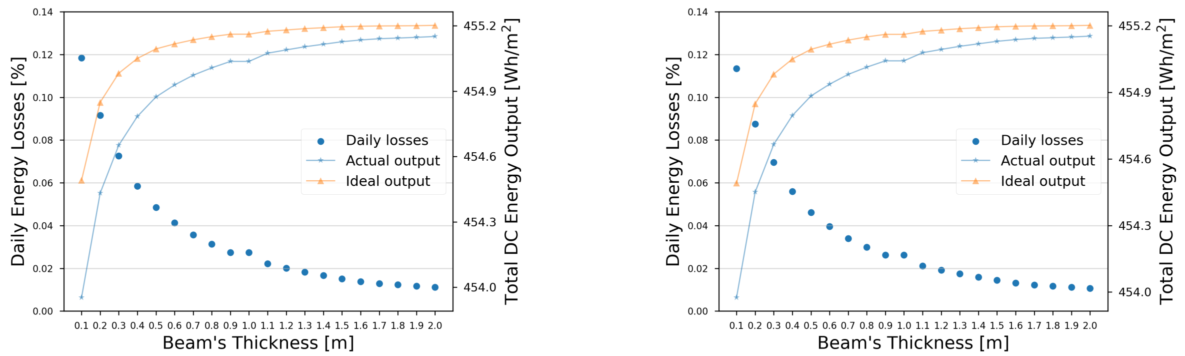

(a) East **(b)** South

Figure 5.7: Effect of the Orientation: Daily energy losses and total DC energy output for various thicknesses for two different azimuths in summer for slight sea conditions.

5.4. Effect of the Material Choice

This section focuses on analyzing the influence of material choice on the structure. Material selection plays a crucial role in determining the behavior of the structure, particularly in relation to eigenfrequencies and wave-induced effects. The parameters set for this analysis are as follows: South orientation and the month of December, as this combination has shown the highest daily energy losses due to power mismatch losses. Figure 5.8 illustrates the effect of varying the beam thickness on the daily energy loss due to power mismatch for all four materials and slight sea state.

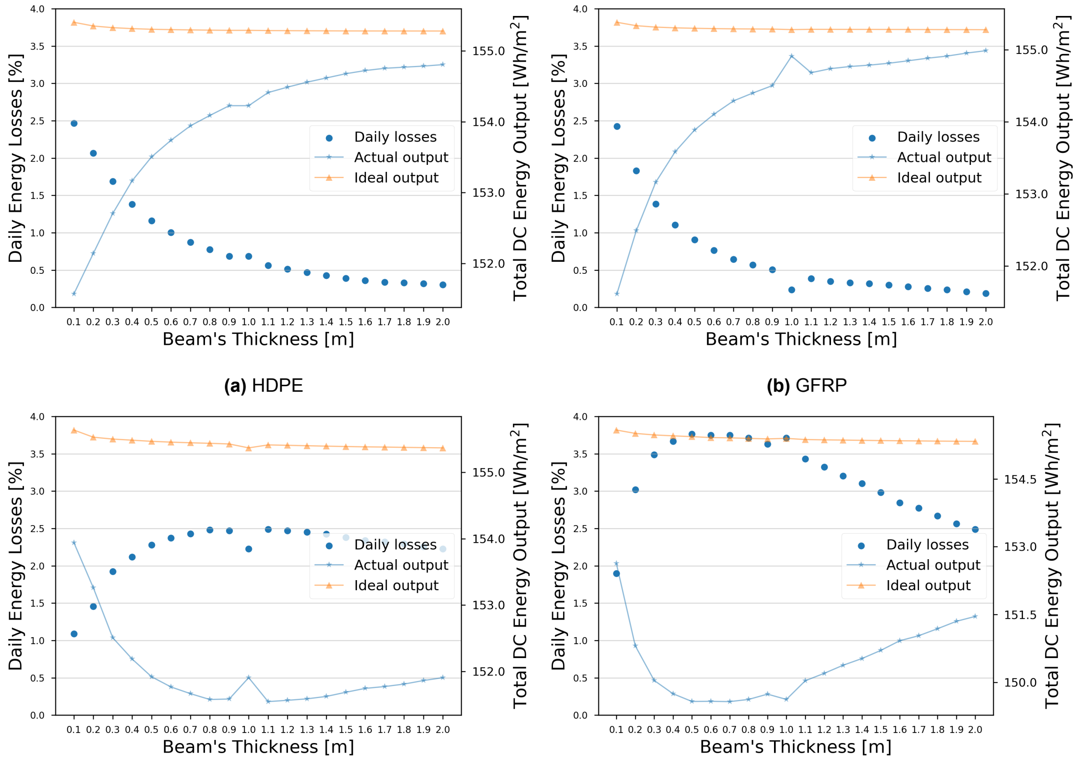

(a) HDPE **(b)** GFRP

(c) EPS **(d)** PVC

Figure 5.8: Effect of the material choice: Electricity losses due to power mismatch losses during a sunny day in December for a slight sea condition. String's azimuth is South.

Figure 5.8 shows that the behavior of HDPE and GFRP on the waves is similar, as the resulting curves for energy losses are much alike. Furthermore, the curves for EPS and PVC look different compared to the ones from HDPE and GFRP. One possible reason is the different order of magnitude of the materials Young's modulus and mechanical properties. There are several points to highlight.

Analysis reveals interesting patterns regarding the effect of thickness on daily energy losses for each material and sea condition. Both HDPE and GFRP demonstrate a consistent decrease in energy losses with increasing thickness, with the exception of occasional spikes. In contrast, EPS and PVC exhibit different trends. Initially, there is an increase in energy losses followed by a period of stagnation and, eventually, a minor decrease. Intriguingly, it is observed that thin structures made of EPS and PVC achieve minimal daily energy losses. These structures lack the mechanical properties to resist the forces exerted by long waves but are seemingly capable of mitigating the impact of smaller waves within the wave spectrum. Hence, these structures conform to the shape of the long waves and suppress the short ones. This leads to a more uniform tilt along the beam and, as a result, less power mismatch and induced energy losses.

The investigation into material density as a parameter in the simulation has yielded intriguing findings. For GFRP and HDPE, the density of the material does not appear to have a significant impact on the observed outcomes. The results related to electricity losses show minimal divergence. In contrast, PVC and EPS exhibit distinct behavior due to their significantly lower Young's modulus compared to HDPE and GFRP. Notably, the density difference of 60 times between PVC and EPS does result in a difference in electricity losses. This suggests that density also plays a role in influencing the magnitude of electricity losses, although the impact of Young's modulus is greater: For materials with high Young modulus, like HDPE and GFRP, density does not have a significant effect on the losses. However, for materials with lower Young modulus, like EPS and PVC, energy losses of considerably higher magnitude can be observed as the density of the material increases.

5.5. Monthly Energy Losses

Monthly simulations were conducted to evaluate the performance of different parameters in minimizing daily energy losses. In subsection 5.5.1, results of an optimal choice of the given parameters are presented, whereas suboptimal parameters are analyzed in subsection 5.5.2. Considering the inclusion of overcast days in the monthly simulations, particularly in December, it is anticipated that the losses will be lower when compared to simulations solely based on sunny days, based on explanations in subsection 3.4.2.

5.5.1. Optimal parameters

After considering all the results from previous subsections, the optimal simulations focused on a thin EPS structure with a thickness of 0.1 m and a thicker GFRP structure with a thickness of 1 m. The choice of a 0.1 m EPS structure was motivated by the observation that all sea states exhibited minimal daily energy losses with this thickness. Thus, it was deemed a promising parameter for reducing energy losses. In contrast, selecting a 1m thickness for the GFRP structure was based on two key factors: firstly, minimizing the electricity losses due to power mismatch, and secondly, the material costs. After examining Figure 5.8b, a flattening trend after some threshold is revealed. This indicated that increasing the thickness further would not significantly reduce electricity losses. However, it is important to note that thicker materials generally incur higher material costs, making the 1m GFRP structure a reasonable compromise between energy efficiency and cost-effectiveness.

These simulations are carried out for the months of July and December, considering both East and South orientations and all four sea states. This results in a total number of 32 simulations. The simulation results are presented in Figure 5.9.

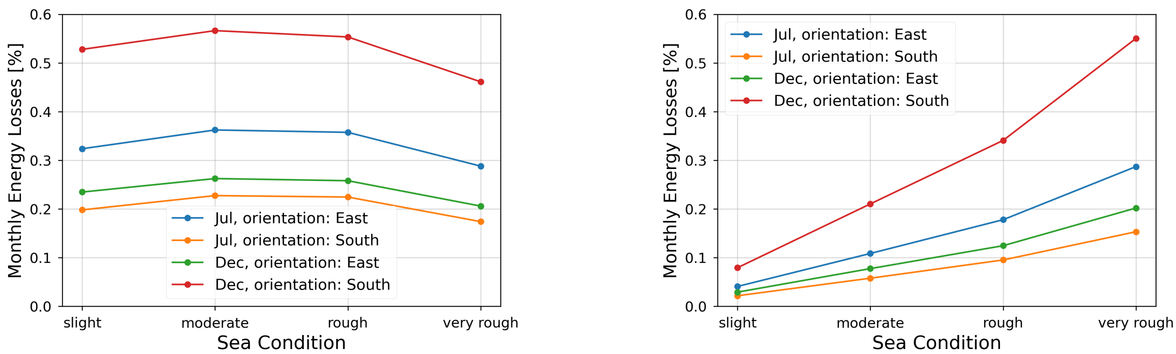

(a) EPS **(b)** GFRP

Figure 5.9: Monthly energy losses for EPS and GFRP for all sea states with optimal parameters.

Firstly, all the energy losses recorded in the two figures are below 0.6%, indicating relatively efficient energy utilization. However, there are noticeable differences among the different scenarios and parameters examined. Regarding absolute performance, GFRP exhibits lower energy losses than EPS. GFRP records the highest monthly loss of 0.55% in December, whereas EPS can reach monthly losses as high as 0.56%. The findings suggest that the GFRP structure demonstrates superior capabilities in supporting the PV modules compared to EPS. This advantage holds true for all sea conditions. In fact, the GFRP structure outperforms EPS by approximately 50% in all sea conditions except for very rough conditions, which are unlikely to occur frequently based on historical data. These results highlight the enhanced performance and suitability of deploying a structure with a high Young's modulus.

Furthermore, the analysis indicates that the worst-case scenario occurs when the string's azimuth faces South in December. This implies that combining a Southern orientation with the winter season increases energy losses due to power mismatch. The East orientation performs better in the winter months than the South orientation. In contrast, in the summer months, the East orientation exhibits higher energy losses than the South orientation. This demonstrates that the sun's position relative to the string's azimuth over a given period has a more pronounced influence on energy losses than the sea state itself, for the case of optimal parameters of a flexible structure. In the context of GFRP, the influence of orientation is only notable in December's moderate, rough, and very rough sea states. Surprisingly, altering the orientation from East to South within these sea states leads to greater losses compared to a change in the sea state. This observation highlights the significance of orientation as a contributing factor. To illustrate, under moderate sea conditions in December, losses amount to approximately 0.075% when facing the East. However, when facing the South, the losses exceed 0.21%. Notably, the highest losses for the East orientation occur during very rough sea conditions, but only 0.2%.

5.5.2. Suboptimal parameters

For this simulation, a 0.9m thick EPS and 0.1m thick GFRP structure are under investigation because these parameters have shown high daily energy losses in the previous chapter. Furthermore, choosing suboptimal parameters represents a case in which the design of the floating structure prioritized factors such as withstanding wave forces rather than specifically optimizing for optoelectrical performance. The results of the monthly energy losses are visualized in Figure 5.10.

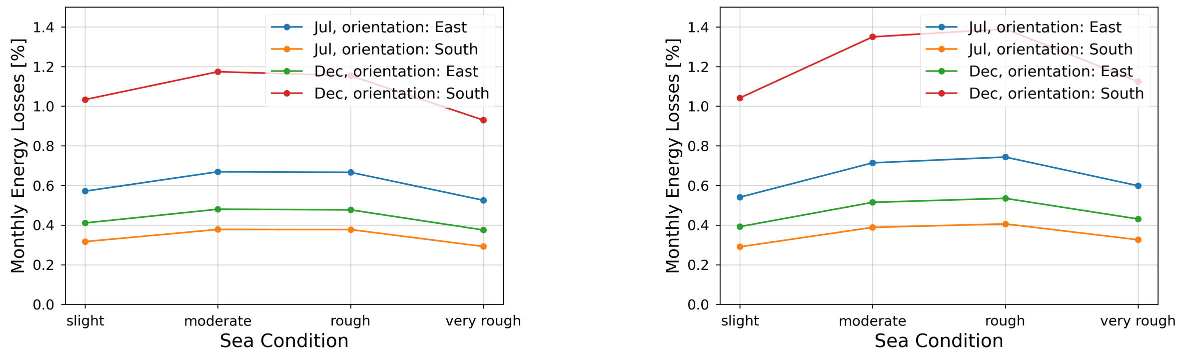

(a) EPS **(b)** GFRP

Figure 5.10: Monthly energy losses for EPS and GFRP for all sea states with suboptimal parameters.

As a result of suboptimal input parameters, the monthly electricity losses have experienced an increase for both materials under examination. Notably, the highest losses recorded for EPS amount to 1.17% during the month of December, particularly under moderate sea conditions and with South orientation. On the other hand, the GFRP configuration exhibits energy losses of 1.39% under rough conditions.

Furthermore, when comparing the response of GFRP to the optimal parameters presented in Figure 5.9b, an interesting observation emerges. The shape of the function depicting energy losses changes significantly. In the case of optimal parameters, the losses increase with the severity of the sea state. However, this trend does not hold true for a suboptimal, thin structure choice as depicted in Figure 5.10b. Surprisingly, the curve for both GFRP and EPS exhibits a similar shape. This similarity suggests that their dynamic behavior is comparable.

To delve deeper into the underlying dynamics, the ratio of the natural eigenfrequencies of the two structures for these specific thicknesses can be examined using Equation 2.55. Notably, the calculated ratio is close to 1, indicating that a thin GFRP structure behaves similarly to a thick EPS structure regarding its dynamic response. This observation suggests that by examining, for instance, the RAO of a newly introduced material and identifying similarities with established structures, one could potentially infer the magnitude of electricity losses caused by power mismatch without performing the entire optoelectrical modeling.

Irrespective of sea conditions, both EPS and GFRP materials exhibit inferior performance when the strings are oriented towards the South during winter. This finding further strengthens the notion that energy losses incurred during noon can not be offset by the late morning and afternoon hours in winter. On the contrary, during the summer season, if the strings face South, both materials demonstrate better performance across all sea conditions. During the summer, it is possible to compensate for any losses incurred during the noon period by making up for them in the morning or afternoon. In summer, the curves depicting energy losses for July reveal a closer alignment between East and South orientations than in winter. This suggests that during summer, the choice of string azimuth does not offer substantial room for minimizing losses.

In summary, for both EPS and GFRP materials, the most favorable outcome in terms of minimizing monthly energy losses caused by power mismatch losses can be seen during the summer season when the string's azimuth is set to face South.

The suggested outcomes of monthly energy losses due to power mismatch, below 1.4% for suboptimal parameter choices of EPS and GFRP, appear to contradict the results presented in [35], which report losses of up to 9%. This discrepancy can be attributed to two possible causes.

Firstly, Dörenkämper et al. [35] conducted their study at two locations very close to the coast and one offshore location situated in the Dogger Bank, known for its shallow water conditions. These locations do not reflect the deep water conditions assumed in this thesis. The behavior of waves in shallow water differs, as they tend to break, leading to distinct wave characteristics.

Secondly, the model employed by Dörenkämper et al. [35] uses a rigid body representation to describe the change in tilt, implying a lack of flexibility or bending in the structure. In contrast, this study incorporates a VLFS model, which considers the bending behavior of the structure. Given the nature of a long structure, rigid behavior is not exhibited, and bending is accounted for.

Interestingly, a comparative case study conducted in the Maldives, where the most occurring significant wave height is 1.2m [74], corroborates the findings of this study, demonstrating power mismatch losses below 0.92% [75]. These results align more closely with the outcomes obtained in the present study for a slight sea state.

Lastly, this study primarily focused on worst-case scenarios to assess the system's performance under challenging conditions. For instance, the PV modules were also placed at the highly oscillating edges within the string, maximizing the exposure to wave-induced tilt variations. Additionally, the wave propagation was assumed to align perfectly with the string, representing a scenario that deepens the effects of wave motion on the power mismatch along the string. Furthermore, a constant (severe) sea state was considered throughout an entire day or month. After analyzing the system's behavior under extreme conditions, a careful assessment was done to gain insights into its performance in adverse scenarios. It is worth noting that when operating conditions are less severe or intermittent and wave-induced motion is not as impactful, the system's performance is expected to improve. Hence, it is essential to interpret the study's findings with the knowledge that the system's actual performance may be better under normal operating conditions.

6 Conclusion

The primary objective of this thesis was to investigate the influence of waves on power mismatch losses along a PV string installed on a floating structure. To achieve this goal, a model for a VLFS was developed and solved utilizing a FEM implemented in the Gridap package in the programming language Julia. Subsequently, the pvlib open-source package was utilized to calculate the irradiance along the structure for specific days and months, determining power mismatch losses.

As introduced in section 1.2, the main research question is:

- **How does power mismatch contribute to daily and monthly energy losses in offshore floating photovoltaic (OFPV) systems deployed in deep water environments?**

To obtain an answer to the main research question, subquestions have been formulated, which are answered below.

- How can the floating structure be accurately modeled to reflect real-world installations?

To accurately model floating structures in line with real-world installations, this research took a distinctive approach that diverged from recent literature. Instead of relying on rigid body mechanics to represent a floating pontoon, a VLFS was utilized, incorporating the major assumption described in assumption 4. This approach allowed for the representation of floating structures consisting of interconnected pontoons. To analyze the behavior of the structure under specific frequencies, a FEM was deployed to solve the system of PDEs in the frequency domain. This enabled the examination of the structure's response to individual frequencies, considering that the sea is composed of a spectrum of sinusoidal waves with different frequencies. By employing a frequency-based approach, each frequency could be analyzed individually, providing valuable insights into the structural behavior. In this study, the Jonswap spectrum, known for accurately representing the wave conditions in the North Sea, was employed as the sea spectrum for deep water conditions. To comprehensively analyze the behavior of the floating structure, four different sea spectra of varying severity were employed, namely ”slight”, ”moderate”, ”rough” and ”very rough”.

- What is the interaction between waves and the structure, and how does it affect the system's performance?

The interaction between waves and the structure was modeled using the Bernoulli-Euler beam theory, where the water pressure acted as a distributed load on the beam. This wave input caused the beam to rise and bend in response. To quantify this interaction, the unitless RAOs were calculated for the elevation η and the slope η_x, as presented in chapter 4. The RAOs provide valuable information on the extent to which different points on the structure are excited by specific frequencies. It was observed that stiffer materials, characterized by higher Young's modulus, exhibited amplification of excitation only within a narrow range of thicknesses and primarily at the edges of the structure. On the other hand, more flexible materials demonstrated amplification across a broader range of thicknesses. Generally, for thicker structures, the RAOs indicated lower values, suggesting increased stability. It is worth mentioning that to draw accurate conclusions about power mismatch losses, additional optoelectrical modeling is necessary. Nevertheless, by comparing the RAOs of newly introduced material with a material that has undergone optoelectrical modeling, assumptions and preliminary conclusions can be made based on the similarity observed in the RAOs. Furthermore, it was observed that the RAOs for a thick, flexible material exhibited similarities to those of a thin, stiff material.

- What are the implications of varying tilts along the structure on power production, and how can these losses be quantified?

Due to the wave input, the structure oscillated, with each point experiencing a different amplitude as given by the RAOs. As a result of these oscillations, points on the structure tilted, deviating from a stationary angle of 0°. The oscillations caused variations in the in-plane irradiance along the structure. At any given time, different points along the structure experienced varying tilt angles, leading to different irradiance levels. The magnitude and range of these irradiance levels differed at each time instant, as highlighted in subsection 3.4.2 and also a function of the PV modules orientation. Consequently, the different irradiance levels resulted in varying power outputs for each PV module installed on the structure. To simulate the worst-case scenario, all modules were assumed to be connected in series, including those at the edges of the structure, which experienced the greatest variations in tilt. Additionally, the wave propagation was assumed to align with the string. The power mismatch was calculated by comparing the system with one central inverter with a system in which each PV module had its own microinverter. By integrating the instantaneous power output for both cases, the daily and monthly energy losses due to power mismatch were calculated. It was shown that power mismatch losses could be reduced substantially by the correct orientation of the modules/string.

- How do changes in material parameters, such as density and stiffness, impact power mismatch and energy losses?

Four different materials were included in this research, covering a range of densities and stiffnesses. Regarding the reduction of daily and monthly energy losses due to power mismatch, the findings revealed that a thick, stiff material performed better than a thin, more flexible one in terms of monthly losses, regardless of the sea state. However, under specific circumstances, the more flexible material exhibited lower power mismatch losses than the stiff one, as demonstrated in subsection 5.5.2. Regarding daily losses, the research indicated that increasing the material's stiffness had a greater impact on reducing power mismatch than increasing the density. This highlights the significance of material properties, particularly stiffness, in optimizing the performance of floating photovoltaic systems and minimizing energy losses due to power mismatch.

The results of this research effectively address the main research question, revealing that power mismatch losses can be almost negligible when appropriate material parameters are selected, particularly in summer for every sea state. However, during winter months, monthly energy losses exceeding 1% due to power mismatch can occur. Additionally, the findings highlight the significant impact of orientation during winter months in reducing power mismatch losses, whereas this effect is less pronounced during summer. Furthermore, it was observed that, for certain material parameters, an increase in sea state severity did not necessarily result in higher power mismatch losses. Lastly, the findings indicated that either a thick structure with a stiff and dense or a thin structure with a flexible and light material minimized energy losses due to power mismatch.

7
Recommendations

In this chapter, recommendations are provided for improving the modeling of OFPV systems. The recommendations are categorized into two sections: mechanical modeling, as discussed in section 7.1, and optoelectrical modeling, addressed in section 7.2. These recommendations are intended to improve the accuracy and reliability of the modeling approaches used in OFPV system analysis, ultimately leading to more comprehensive and precise predictions of system behavior.

7.1. Mechanical Modelling

- The fundamental premise underlying this thesis is the assumption stated in assumption 4, which posits that a continuous beam model can effectively represent a structure comprising multiple beam elements interconnected by semi-rigid joints. In order to gain deeper insights into the influence of these joints on the structural behavior and to achieve a more accurate representation of real-world installations, it is necessary to incorporate multiple joints into the simplified model described in subsection 3.1.1. The mathematical formulation for this enhanced model has already been presented; the only consideration remaining is the computational time required for its solution. Furthermore, in order to streamline the analysis and reduce the complexity of the model, it is advisable to limit the number of material choices to two (stiff vs. rigid) or the number of thicknesses, thereby minimizing the number of possible combinations.
- In order to capture the full three-dimensional behavior of the structure, the use of Poisson-Kirchhoff plate equations is recommended. Additionally, incorporating the direction of wave propagation in the model allows for a more accurate representation of the dynamic interactions between the structure and the waves.
- It is recommended to perform a detailed structural analysis of the optimized structures presented in this study, focusing specifically on the optimal thicknesses determined. This analysis should encompass a thorough investigation of the loads exerted on the structure itself, the mooring, and the anchoring system. This information will contribute significantly to evaluating the feasibility and effectiveness of the proposed beam parameters, ensuring their ability to withstand the applied loads and operate reliably in the intended environmental conditions.

7.2. Optoelectrical Modeling

- In this research, the temperature of the PV modules was not explicitly modeled due to its minimal influence on power mismatch losses, which are expressed as relative values. However, it is important to acknowledge that when conducting future research aimed at comparing the energy yield of an OFPV system with a land-based one, the temperature effect should be taken into consideration. The temperature has a significant impact on the performance and efficiency of PV modules, and accounting for this factor is crucial for a comprehensive and accurate assessment of the energy production potential of OFPV systems.
- In this study, the albedo was assumed to be constant. However, future research could enhance the modeling approach by considering the variability of the albedo factor in relation to the sea

surface agitation. The agitation of the sea surface, influenced by factors such as wind speed and wave conditions, can affect the reflectivity of the water, leading to variations in albedo.

- A rotation mechanism would enable the rotation of the structure and adjust the orientation of the PV modules to track the movement of the sun throughout the day. By including a tracking mechanism, the model can account for the dynamic changes in solar irradiance and optimize the performance of the PV modules. This is particularly interesting when comparing the energy production of OFPV systems to land-based ones.

List of Figures

List of Tables

References

[1] IPCC. *Summary for Policymakers. Policymakers*. doi:10.1017/9781009157926.001. Cambridge, UK and New York, NY, USA.

[2] M. Schmela. *EU Market Outlook for Solar Power*. ISBN: 9789464669015. 2022.

[3] R. J. A. M. Stevens et al. “Combining economic and fluid dynamic models to determine the optimal spacing in very large wind farms: Combining economic and fluid dynamic models to determine the optimal spacing in very large wind farms”. In: *Wind Energy* 20.3 (Mar. 2017), pp. 465–477. ISSN: 10954244. DOI: 10.1002/we.2016. URL: https://onlinelibrary.wiley.com/doi/10.1002/we.2016 (visited on 06/12/2023).

[4] S. Z. Golroodbari and W. Sark. “Simulation of performance differences between offshore and land□based photovoltaic systems”. In: *Progress in Photovoltaics: Research and Applications* 28.9 (Sept. 2020), pp. 873–886. ISSN: 1062-7995, 1099-159X. DOI: 10.1002/pip.3276. URL: https://onlinelibrary.wiley.com/doi/10.1002/pip.3276 (visited on 08/22/2022).

[5] A.-M. Chirosca, L. Rusu, and A. Bleoju. “Study on wind farms in the North Sea area”. In: *Energy Reports* 8 (Dec. 2022), pp. 162–168. ISSN: 23524847. DOI: 10.1016/j.egyr.2022.10.244. URL: https://linkinghub.elsevier.com/retrieve/pii/S2352484722021795 (visited on 06/26/2023).

[6] EU-SCORES. *EU-SCORES: Eropean Scalable Offshore Renewable Energy Source*. EU-SCORES. 2023. URL: https://euscores.eu/ (visited on 06/26/2023).

[7] W. B. Group, ESMAP, and SERIS. *Where Sun Meets Water: Floating Solar Market Report*. Washington, DC, 2019.

[8] H. Ziar. “Floating Solar Stations”. In: *10 breakthrough ideas in energy for the next 10 years* Nr. 2 (June 3, 2021), pp. 30–43.

[9] S. H. Kim et al. “Design and Installation of 500-kW Floating Photovoltaic Structures Using High-Durability Steel”. In: *Energies* 13.19 (2020), p. 4996. DOI: 10.3390/en13194996.

[10] U. Gupta. “The case for floating PV on hydroelectric facilities”. In: *pv magazine India* (Jan. 18, 2021). URL: https://www.pv-magazine-india.com/2021/01/18/the-case-for-combining-floating-solar-pv-with-hydroelectric-power-plants/ (visited on 06/24/2023).

[11] S.-H. Kim et al. “Application of Floating Photovoltaic Energy Generation Systems in South Korea”. In: *Sustainability* 8.12 (Dec. 17, 2016), p. 1333. ISSN: 2071-1050. DOI: 10.3390/su8121333. URL: http://www.mdpi.com/2071-1050/8/12/1333 (visited on 06/24/2023).

[12] S. Rai-Roche. “Keppel, Ocean Sun to pilot membrane-based floating PV project in Singapore”. In: *PV Tech* (July 19, 2022). URL: https://www.pv-tech.org/keppel-ocean-sun-win-membrane-floating-solar-pv-system-contract-in-singapore/ (visited on 06/24/2023).

[13] M. Ikhennicheu et al. “Analytical method for loads determination on floating solar farms in three typical environments”. In: *Solar Energy* 219 (May 2021), pp. 34–41. ISSN: 0038092X. DOI: 10.1016/j.solener.2020.11.078. URL: https://linkinghub.elsevier.com/retrieve/pii/S0038092X20312664 (visited on 08/30/2022).

[14] A. G. Aberle et al. “Field experience and performance analysis of floating PV technologies in the tropics”. In: *Progress in Photovoltaics* 26.12 (Dec. 1, 2018). MAG ID: 2810234504, pp. 957–967. DOI: 10.1002/pip.3039.

[15] H. Pouran et al. “Environmental and technical impacts of floating photovoltaic plants as an emerging clean energy technology”. In: *iScience* (Oct. 1, 2022), pp. 105253–105253. DOI: 10.1016/j.isci.2022.105253.

[16] S. Desai, M. Wagh, and N. Shinde. “A Review on Floating Solar Photovoltaic Power Plants”. In: *International Journal of Scientific and Engineering Research* 6 (June 1, 2017), pp. 789–794.

[17] A. Ghigo et al. “Design and Analysis of a Floating Photovoltaic System for Offshore Installation: The Case Study of Lampedusa”. In: *Energies* (2022). DOI: 10.3390/en15238804.

[18] K. Trapani and D. L. Millar. “Floating photovoltaic arrays to power the mining industry: A case study for the McFaulds lake (Ring of Fire)”. In: *Environmental Progress & Sustainable Energy* 35.3 (2016), pp. 898–905. DOI: https://doi.org/10.1002/ep.12275. URL: https://aiche.onlinelibrary.wiley.com/doi/abs/10.1002/ep.12275.

[19] Iberdrola. *Floating Photovoltaic Solar Energy*. URL: https://www.iberdrola.com/innovation/floating-photovoltaic (visited on 01/12/2023).

[20] F. Koppes. *A world’s first: offshore floating solar farm installed at the Dutch North Sea*. Oceans of Energy. Dec. 11, 2019. URL: https://oceansofenergy.blue/2019/12/11/a-worlds-first-offshore-floating-solar-farm-installed-at-the-dutch-north-sea/ (visited on 01/12/2023).

[21] A. Garanovic. *Oceans of Energy gets Bureau Veritas’ nod of approval for offshore floating solar system*. Offshore Energy. Jan. 10, 2023. URL: https://www.offshore-energy.biz/oceans-of-energy-gets-bureau-veritas-nod-of-approval-for-offshore-floating-solar-system/ (visited on 01/13/2023).

[22] Swimsol. *World’s first offshore floating solar at sea 2014 Maldives*. 2015. URL: https://swimsol.com/solar-projects/worlds-first-floating-solar-platform-at-sea/ (visited on 06/23/2023).

[23] L. Cooke. “How floating solar panels are helping the Maldives ditch diesel fuel”. In: *Inhabitat - Green Design, Innovation, Architecture, Green Building | Green design & innovation for a better world* (Mar. 29, 2018). URL: https://inhabitat.com/how-floating-solar-panels-are-helping-the-maldives-ditch-diesel-fuel/ (visited on 01/13/2023).

[24] SolarDuck. *SolarDuck unveils design of its offshore floating solar Technology – SolarDuck*. Apr. 30, 2021. URL: https://solarduck.tech/solarduck-unveils-design-of-its-offshore-floating-solar-technology/ (visited on 01/13/2023).

[25] B. Santos. “RWE und Solar Duck kombinieren Offshore-Windpark mit Photovoltaik in der Nordsee”. In: *pv magazine Deutschland* (Nov. 14, 2022). URL: https://www.pv-magazine.de/2022/11/14/rwe-und-solar-duck-kombinieren-offshore-windpark-mit-photovoltaik-in-der-nordsee/ (visited on 01/13/2023).

[26] SolarDuck. *SolarDuck will build Japan’s first offshore floating solar demonstrator in Tokyo Bay – SolarDuck*. Dec. 12, 2022. URL: https://solarduck.tech/solarduck-will-build-japans-first-offshore-floating-solar-demonstrator-in-tokyo-bay/ (visited on 01/13/2023).

[27] OceanSun. *SPIC has commissioned world’s first offshore wind and floating solar powerplant in, Shandong, China, utilizing the patented Ocean Sun technology | Ocean Sun*. Nov. 1, 2022. URL: https://oceansun.no/spic-has-commissioned-worlds-first-offshore-wind-and-floating-solar-powerplant-in-shandong-china-utilizing-the-patented-ocean-sun-technology/ (visited on 01/13/2023).

[28] A. Habibic. *Bluewater to further develop flexible floating offshore solar concept*. Offshore Energy. Nov. 30, 2022. URL: https://www.offshore-energy.biz/bluewater-to-further-develop-flexible-floating-offshore-solar-concept/ (visited on 01/13/2023).

[29] H. Cleijne et al. *North Sea Energy Outlook*. Arnhem, 2020, p. 92. URL: https://www.dnv.com/Publications/north-sea-energy-outlook-192287 (visited on 07/23/2022).

[30] R. Cazzaniga et al. “Floating photovoltaic plants: Performance analysis and design solutions”. In: *Renewable & Sustainable Energy Reviews* 81 (Jan. 1, 2018). MAG ID: 2623630156 S2ID: 3cd3f811eba623611739b29c4a20e5f2bb47448e, pp. 1730–1741. DOI: 10.1016/j.rser.2017.05.269.

[31] H. Liu, A. Kumar, and T. Reindl. “The Dawn of Floating Solar—Technology, Benefits, and Challenges”. In: *WCFS2019. Lecture Notes in Civil Engineering.* Vol. 41. Singapore: Springer Singapore, 2020, pp. 373–383. URL: https://doi.org/10.1007/978-981-13-8743-2_21 (visited on 08/30/2022).

[32] M. Grech et al. “Floating photovoltaic installations in maltese sea waters”. In: 32nd European Photovoltaic Solar Energy Conference and Exhibition. Munich, June 2016, pp. 1964–1968.

[33] S. Oliveira-Pinto and J. Stokkermans. “Assessment of the potential of different floating solar technologies – Overview and analysis of different case studies”. In: *Energy Conversion and Management* 211 (May 1, 2020). MAG ID: 3013778279, p. 112747. DOI: 10.1016/j.enconman.2020.112747.

[34] N. Monaco. “Offshore floating PV yield considering wave effect”. masterthesis. EWI, TU Delft. URL: https://repository.tudelft.nl/islandora/object/uuid%3Af7342d60-6f07-404b-867e-7fc3ca73fb43?collection=education.

[35] M. Dörenkämper et al. “Influence of wave induced movements on the performance of floating PV systems”. In: *36th European Photovoltaic Solar Energy Conference and Exhibition*. EU PVSEC. France, 2019, pp. 1759–1762.

[36] D. K. Sree et al. “Fluid-structural analysis of modular floating solar farms under wave motion”. In: *Solar Energy* 233 (Feb. 2022), pp. 161–181. ISSN: 0038092X. DOI: 10.1016/j.solener.2022.01.017. URL: https://linkinghub.elsevier.com/retrieve/pii/S0038092X22000202 (visited on 08/12/2022).

[37] O. Colomes Gene, Akkerman, and F. Verdugo. “A monolithic Finite Element formulation for the hydroelastic analysis of Very Large Floating Structures”. In: *International Journal for Numerical Methods in Engineering* (2022). DOI: 10.48550/arxiv.2206.12410.

[38] A. H. M. Smets et al. *Solar energy: the physics and engineering of photovoltaic conversion, technologies and systems*. Cambridge, England: UIT Cambridge, 2016. 462 pp. ISBN: 978-1-906860-32-5.

[39] R. Perez et al. “A new simplified version of the perez diffuse irradiance model for tilted surfaces”. In: *Solar Energy* 39.3 (1987), pp. 221–231. ISSN: 0038092X. DOI: 10.1016/S0038-092X(87)80031-2. URL: https://linkinghub.elsevier.com/retrieve/pii/S0038092X87800312 (visited on 06/07/2023).

[40] P. Ineichen. *Global irradiance on tilted and oriented planes: model validations*. Univeristy of Geneva, 2011.

[41] R. G. Dean and R. A. Dalrymple. *Water wave mechanics for engineers and scientists*. Advanced series on ocean engineering v. 2. Singapore ; Teaneck, NJ: World Scientific, 1991. 353 pp. ISBN: 978-981-02-0420-4.

[42] K. Sadeghi, G. J. Dzayi, and Z. Alothman. “An overview of generation, theories, formulas and application of sea waves”. In: *Academic Research International* 8(4) (Dec. 2017).

[43] “The Marine Environment”. In: *The Maritime Engineering Reference Book*. Ed. by A. F. Molland. Elsevier, 2008, pp. 1–42. ISBN: 978-0-7506-8987-8. DOI: 10.1016/B978-0-7506-8987-8.00001-9. URL: https://linkinghub.elsevier.com/retrieve/pii/B9780750689878000019 (visited on 06/08/2023).

[44] A. Pecher and J. P. Kofoed, eds. *Handbook of Ocean Wave Energy*. Vol. 7. Ocean Engineering & Oceanography. Cham: Springer International Publishing, 2017. ISBN: 978-3-319-39888-4. DOI: 10.1007/978-3-319-39889-1. URL: http://link.springer.com/10.1007/978-3-319-39889-1 (visited on 06/09/2023).

[45] K. Hasselmann et al. “Measurements of wind-wave growth and swell decay during the Joint North Sea Wave Project (JONSWAP)”. In: *Ergänzungsheft zur Deutschen Hydrographischen Zeitschrift Reihe A* Nr. 12 (1973). Publisher: Deutches Hydrographisches Institut. URL: https://repository.tudelft.nl/islandora/object/uuid%3Af204e188-13b9-49d8-a6dc-4fb7c20562fc (visited on 06/09/2023).

[46] C. C. C. Service. *Welcome to the Climate Data Store*. Welcome to the Climate Data Store. 2021. URL: https://cds.climate.copernicus.eu/cdsapp#!/home (visited on 06/09/2023).

[47] Y. Goda. *Random Seas And Design Of Maritime Structures (3rd Edition)*. Google-Books-ID: 1EQyDwAAQBAJ. World Scientific Publishing Company, June 23, 2010. 733 pp. ISBN: 978-981-310-102-9.

[48] A. Andrianov. “Hydroelestic analyis of very large floating structures”. PhD thesis. Delft: TU Delft.

[49] *Normal distribution*. In: *Wikipedia*. Page Version ID: 1157742125. May 30, 2023. URL: https://en.wikipedia.org/w/index.php?title=Normal_distribution&oldid=1157742125 (visited on 06/09/2023).

[50] W. W. LaMorte. *Central Limit Theorem*. 2016. URL: https://sphweb.bumc.bu.edu/otlt/mph-modules/bs/bs704_probability/BS704_Probability12.html (visited on 06/09/2023).

[51] A. Géron. *Hands-on machine learning with Scikit-Learn, Keras, and TensorFlow: concepts, tools, and techniques to build intelligent systems*. Second edition. Beijing [China] ; Sebastopol, CA: O’Reilly Media, Inc, 2019. 819 pp. ISBN: 978-1-4920-3264-9.

[52] M. Riyansyah, C. Wang, and Y. Choo. “Connection design for two-floating beam system for minimum hydroelastic response”. In: *Marine Structures* 23.1 (Jan. 2010), pp. 67–87. ISSN: 09518339. DOI: 10.1016/j.marstruc.2010.01.001. URL: https://linkinghub.elsevier.com/retrieve/pii/S095183391000002X (visited on 06/01/2023).

[53] I. Shakir Abbood et al. “Properties evaluation of fiber reinforced polymers and their constituent materials used in structures – A review”. In: *Materials Today: Proceedings* 43 (2021), pp. 1003–1008. ISSN: 22147853. DOI: 10.1016/j.matpr.2020.07.636. URL: https://linkinghub.elsevier.com/retrieve/pii/S2214785320357618 (visited on 02/20/2023).

[54] U. F. Products. *Dock Floats & Marine Flotation | Geofoam, Styrofoam, EPS & Polystyrene | Universal Foam Products*. 2023. URL: https://universalconstructionfoam.com/products/dock-floats-and-marine-flotation/ (visited on 06/12/2023).

[55] TNO. *Floating solar panels*. tno.nl/en. 2022. URL: https://www.tno.nl/en/sustainable/renewable-electricity/sustainable-solar-land-water/floating-solar-panels/ (visited on 06/20/2023).

[56] IRENA. *Future of wind: Deployment, investment, technology, grid integration and socio-economic aspects (A Global Energy Transformation paper)*. Abu Dhabi: Internation Renewable Energy Agency, 2019. URL: https://www.irena.org/-/media/Files/IRENA/Agency/Publication/2019/Oct/IRENA_Future_of_wind_2019.pdf (visited on 06/12/2023).

[57] E. Engebretsen, S. K. Haver, and D. Myrhaug. “Extreme Wave Condition at Doggerbank”. In: *Journal of Offshore Mechanics and Arctic Engineering* 138.4 (Aug. 1, 2016), p. 041601. ISSN: 0892-7219, 1528-896X. DOI: 10.1115/1.4033564. URL: https://asmedigitalcollection.asme.org/offshoremechanics/article/doi/10.1115/1.4033564/375303/Extreme-Wave-Condition-at-Doggerbank (visited on 06/20/2023).

[58] M. v. A. Zaken. *Offshore wind energy*. Last Modified: 2022-08-26T17:52 Publisher: Ministerie van Algemene Zaken. July 26, 2017. URL: https://www.government.nl/topics/renewable-energy/offshore-wind-energy (visited on 06/20/2023).

[59] M. W. Kim, W. Koo, and S. Y. Hong. “Numerical analysis of various artificial damping schemes in a three-dimensional numerical wave tank”. In: *Ocean Engineering* 75 (Jan. 2014), pp. 165–173. ISSN: 00298018. DOI: 10.1016/j.oceaneng.2013.10.012. URL: https://linkinghub.elsevier.com/retrieve/pii/S0029801813003818 (visited on 03/08/2023).

[60] A. Harish. *What Is FEM & FEA Explained | Finite Element Method*. SimScale. Oct. 24, 2016. URL: https://www.simscale.com/blog/what-is-finite-element-method/ (visited on 06/13/2023).

[61] S. Badia and F. Verdugo. “Gridap: An extensible Finite Element toolbox in Julia”. In: *Journal of Open Source Software* 5.52 (Aug. 26, 2020), p. 2520. ISSN: 2475-9066. DOI: 10.21105/joss.02520. URL: https://joss.theoj.org/papers/10.21105/joss.02520 (visited on 06/13/2023).

[62] D. Regout. “Hydroelastic Analysis of a Multi-Module Very Large Floating Structure”. masterthesis. CiGT, TU Delft, 2021. URL: https://repository.tudelft.nl/islandora/object/uuid%3A838e2e14-d0e8-49dc-bad4-e7e132b248bc (visited on 11/21/2022).

[63] C. Shannon. “Communication in the Presence of Noise”. In: *Proceedings of the IRE* 37.1 (Jan. 1949), pp. 10–21. ISSN: 0096-8390. DOI: 10.1109/JRPROC.1949.232969. URL: http://ieeexplore.ieee.org/document/1697831/ (visited on 06/15/2023).

[64] E. H. Owens. “Sea conditions”. In: M. Schwartz. *Beaches and Coastal Geology*. New York, NY: Springer US, 1982, pp. 722–722. ISBN: 978-0-87933-213-6. URL: https://link.springer.com/10.1007/0-387-30843-1_397 (visited on 06/16/2023).

[65] G. B. Rossi et al. “Comparison of Spectrum Estimation Methods for the Accurate Evaluation of Sea State Parameters”. In: *Sensors* 20.5 (Mar. 5, 2020), p. 1416. ISSN: 1424-8220. DOI: 10.3390/s20051416. URL: https://www.mdpi.com/1424-8220/20/5/1416 (visited on 05/08/2023).

[66] BosswerkGmbH. *GreenAkku*. 2023. URL: https://greenakku.de/Solarmodule/Flexible-Solarmodule/Bosswerk-Sphere-Hoch-Flexibles-Solarmodul-ETFE-200Wp::4499.html (visited on 06/17/2023).

[67] W. F. Holmgren, C. W. Hansen, and M. A. Mikofski. “pvlib python: a python package for modeling solar energy systems”. In: *Journal of Open Source Software* 3.29 (Sept. 7, 2018), p. 884. ISSN: 2475-9066. DOI: 10.21105/joss.00884. URL: http://joss.theoj.org/papers/10.21105/joss.00884 (visited on 06/19/2023).

[68] S. Golroodbari and W. Van Sark. “On the effect of dynamic albedo on performance modelling of offshore floating photovoltaic systems”. In: *Solar Energy Advances* 2 (2022), p. 100016. ISSN: 26671131. DOI: 10.1016/j.seja.2022.100016. URL: https://linkinghub.elsevier.com/retrieve/pii/S2667113122000043 (visited on 06/19/2023).

[69] G. Sinnett and F. Feddersen. “Observations and parameterizations of surfzone albedo”. In: *Methods in Oceanography* 17 (Dec. 2016), pp. 319–334. ISSN: 22111220. DOI: 10.1016/j.mio.2016.07.001. URL: https://linkinghub.elsevier.com/retrieve/pii/S2211122016300044 (visited on 06/19/2023).

[70] KNMI. *API Developer portal*. 2023. URL: https://developer.dataplatform.knmi.nl/apis (visited on 06/19/2023).

[71] J. Boland, J. Huang, and B. Ridley. “Decomposing global solar radiation into its direct and diffuse components”. In: *Renewable and Sustainable Energy Reviews* 28 (Dec. 2013), pp. 749–756. ISSN: 13640321. DOI: 10.1016/j.rser.2013.08.023. URL: https://linkinghub.elsevier.com/retrieve/pii/S1364032113005637 (visited on 06/19/2023).

[72] NASA. *Derived Parameters*. 2021. URL: https://power.larc.nasa.gov/docs/methodology/energy-fluxes/derived-parameters/ (visited on 06/19/2023).

[73] J. Ortiz Lizcano et al. “Bypass Dioes and Mismatch Losses”. Lecture Notes. Lecture Notes. TU Delft, 2023.

[74] G. Rinaldi et al. “Assessment of extreme and metocean conditions in the Maldives for OTEC applications”. In: *International Journal of Energy Research* 43.13 (2019), pp. 7316–7335. ISSN: 1099-114X. DOI: 10.1002/er.4762. URL: https://onlinelibrary.wiley.com/doi/abs/10.1002/er.4762 (visited on 06/24/2023).

[75] N. Ravichandran, B. Panneerselvam, and Nagavinothini Ravichandran. “Comparative assessment of offshore floating photovoltaic systems using thin film modules for Maldives islands”. In: *Sustainable Energy Technologies and Assessments* 53 (Oct. 1, 2022), p. 102490. ISSN: 2213-1388. DOI: 10.1016/j.seta.2022.102490. URL: https://www.sciencedirect.com/science/article/pii/S2213138822005409 (visited on 01/23/2023).

A

Further Mechanical Results

A.1. RAOs

A.1.1. RAO for the Elevation

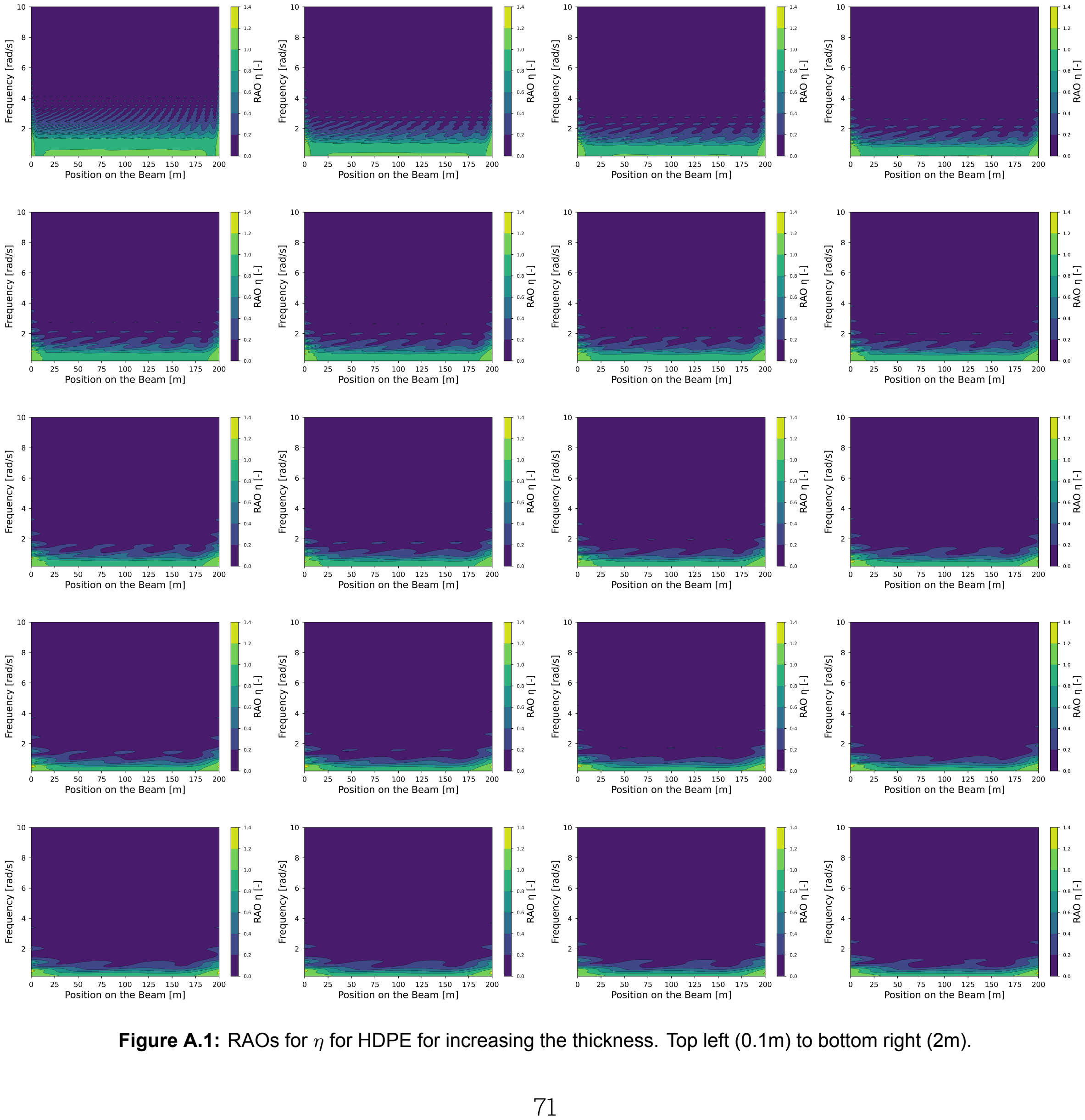

Figure A.1: RAOs for η for HDPE for increasing the thickness. Top left (0.1m) to bottom right (2m).

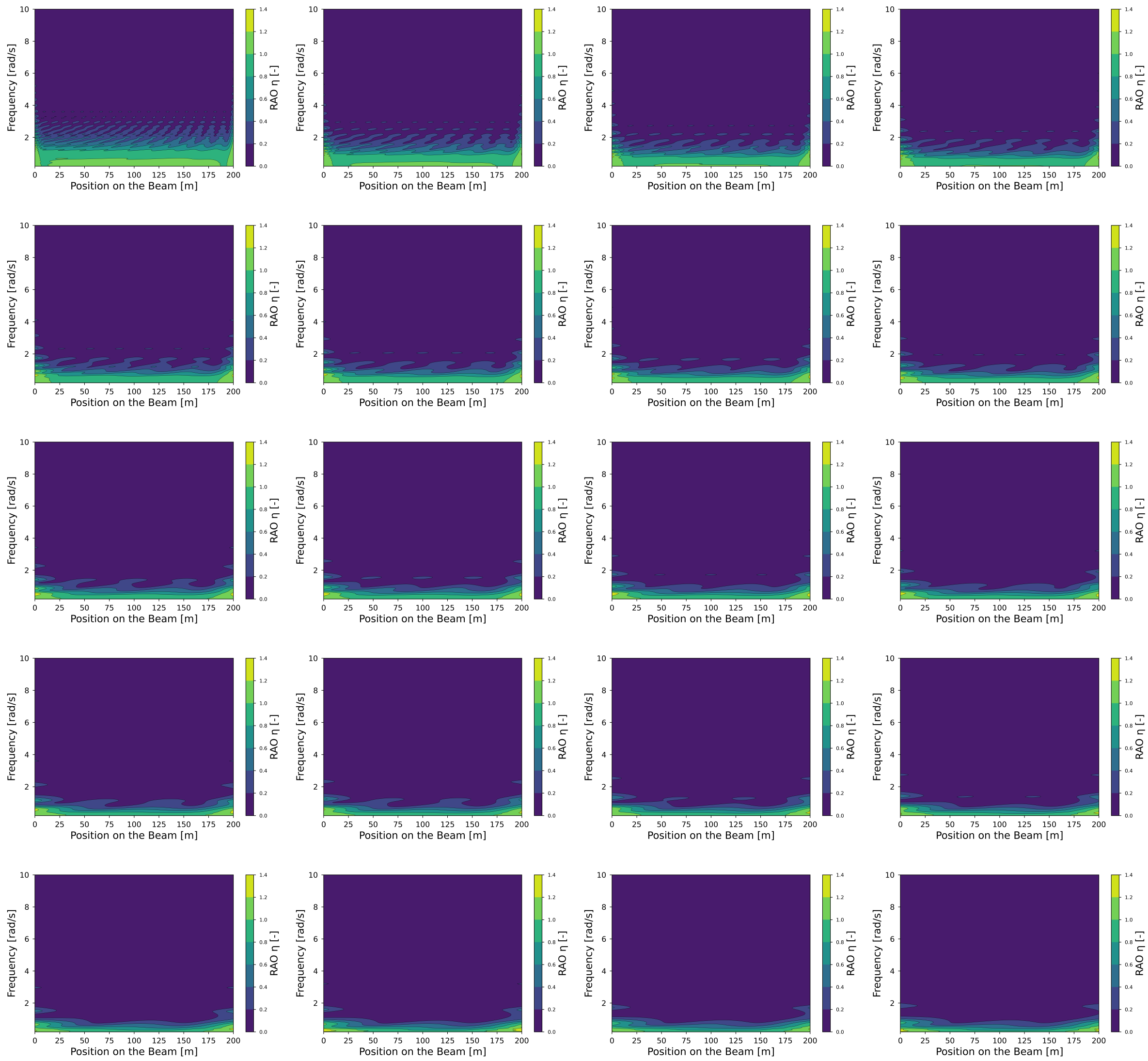

Figure A.2: RAOs for η for GFRP for increasing the thickness. Top left (0.1m) to bottom right (2m).

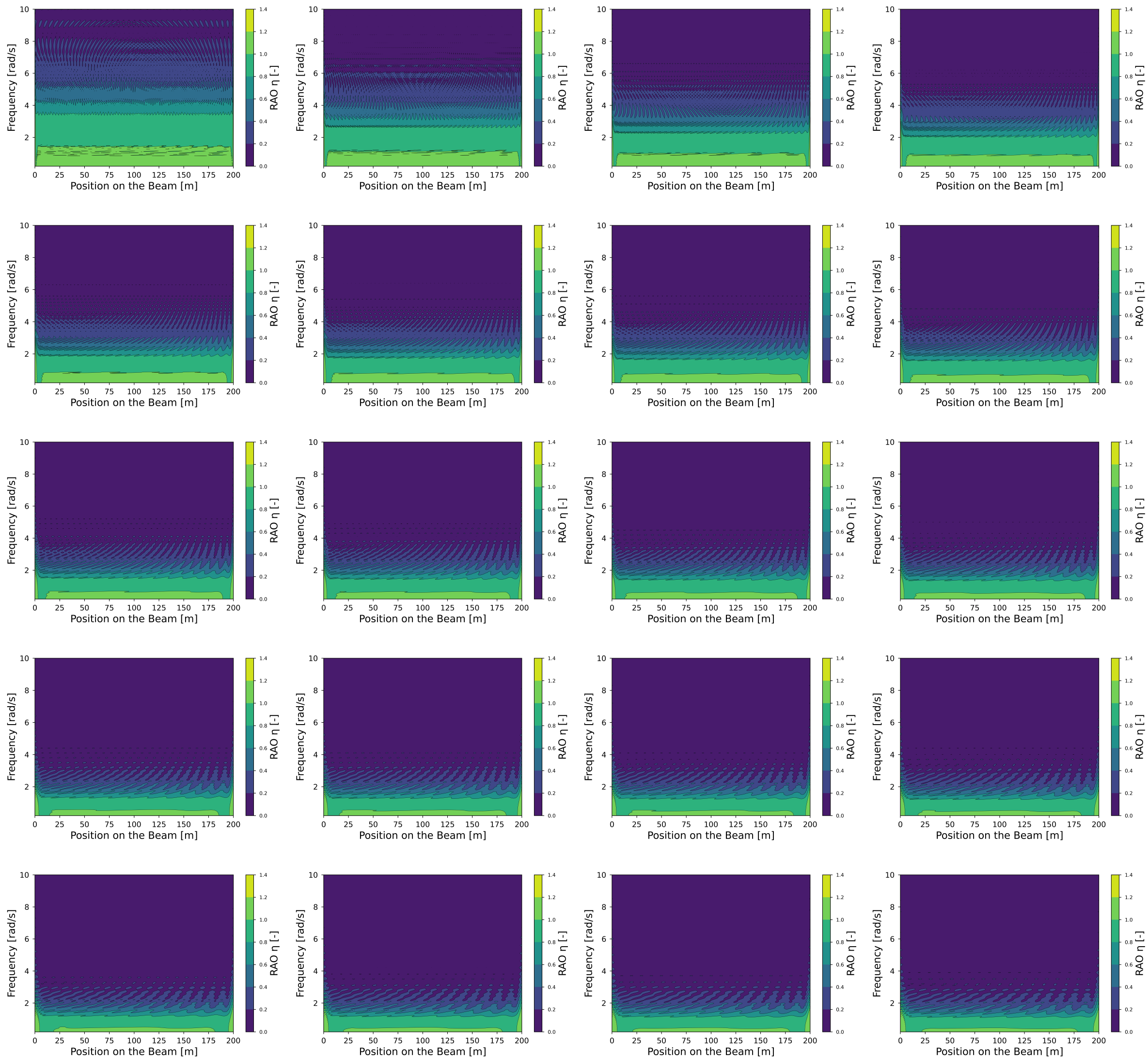

Figure A.3: RAOs for η for EPS for increasing the thickness. Top left (0.1m) to bottom right (2m).

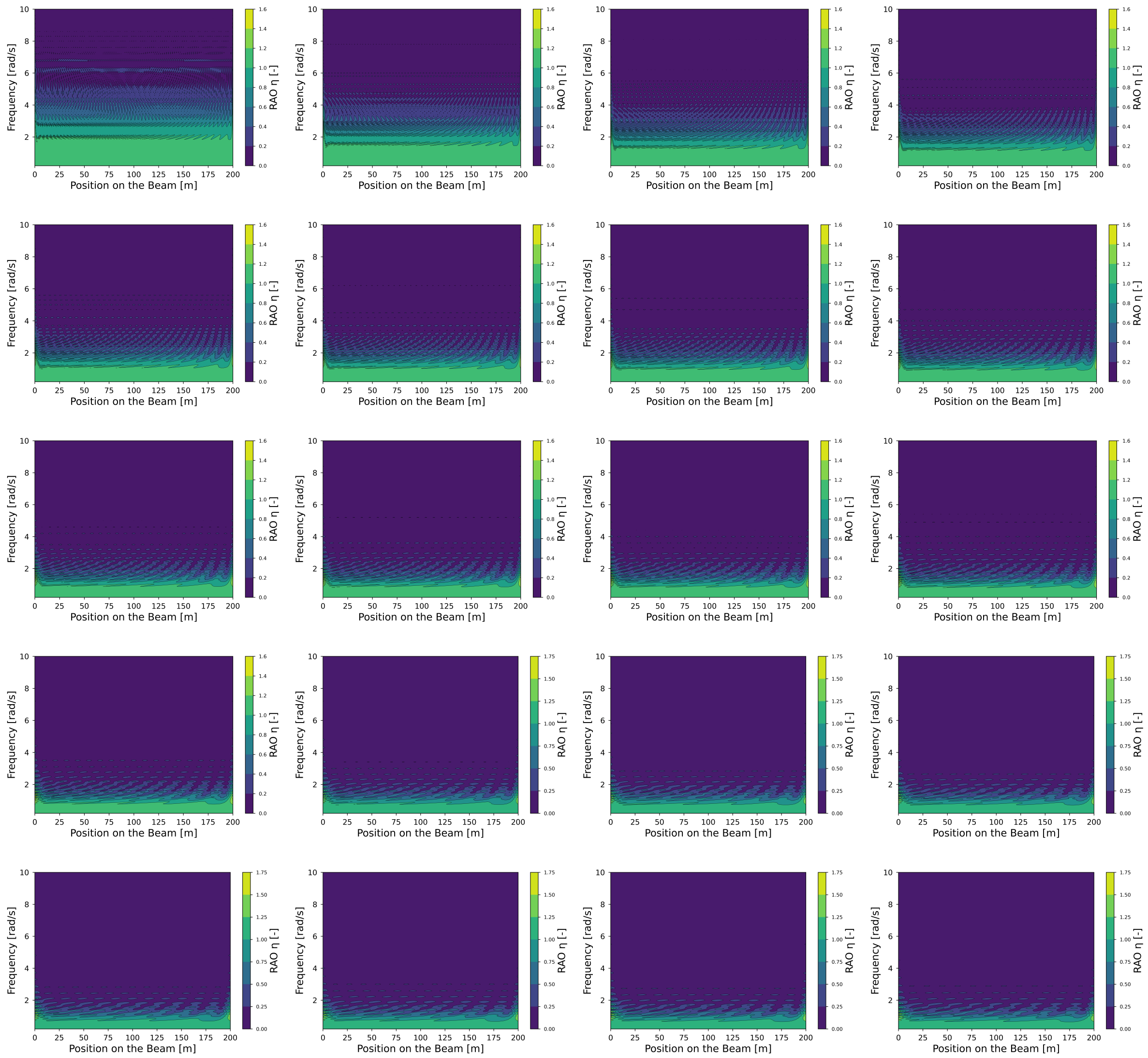

Figure A.4: RAOs for η for PVC for increasing the thickness. Top left (0.1m) to bottom right (2m).

A.1.2. RAO for the Slope

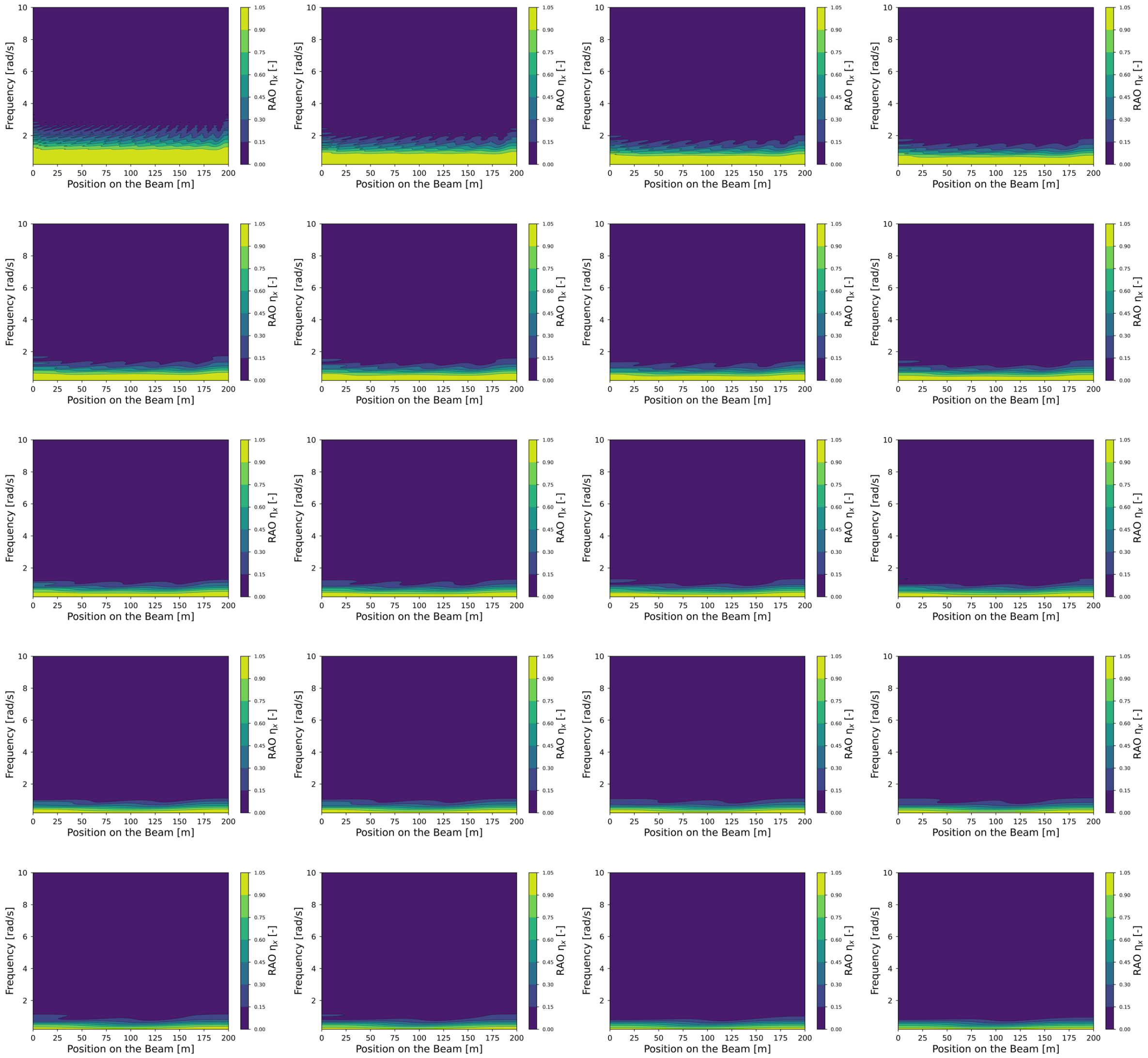

Figure A.5: RAOs for η_x for HDPE for increasing the thickness. Top left (0.1m) to bottom right (2m).

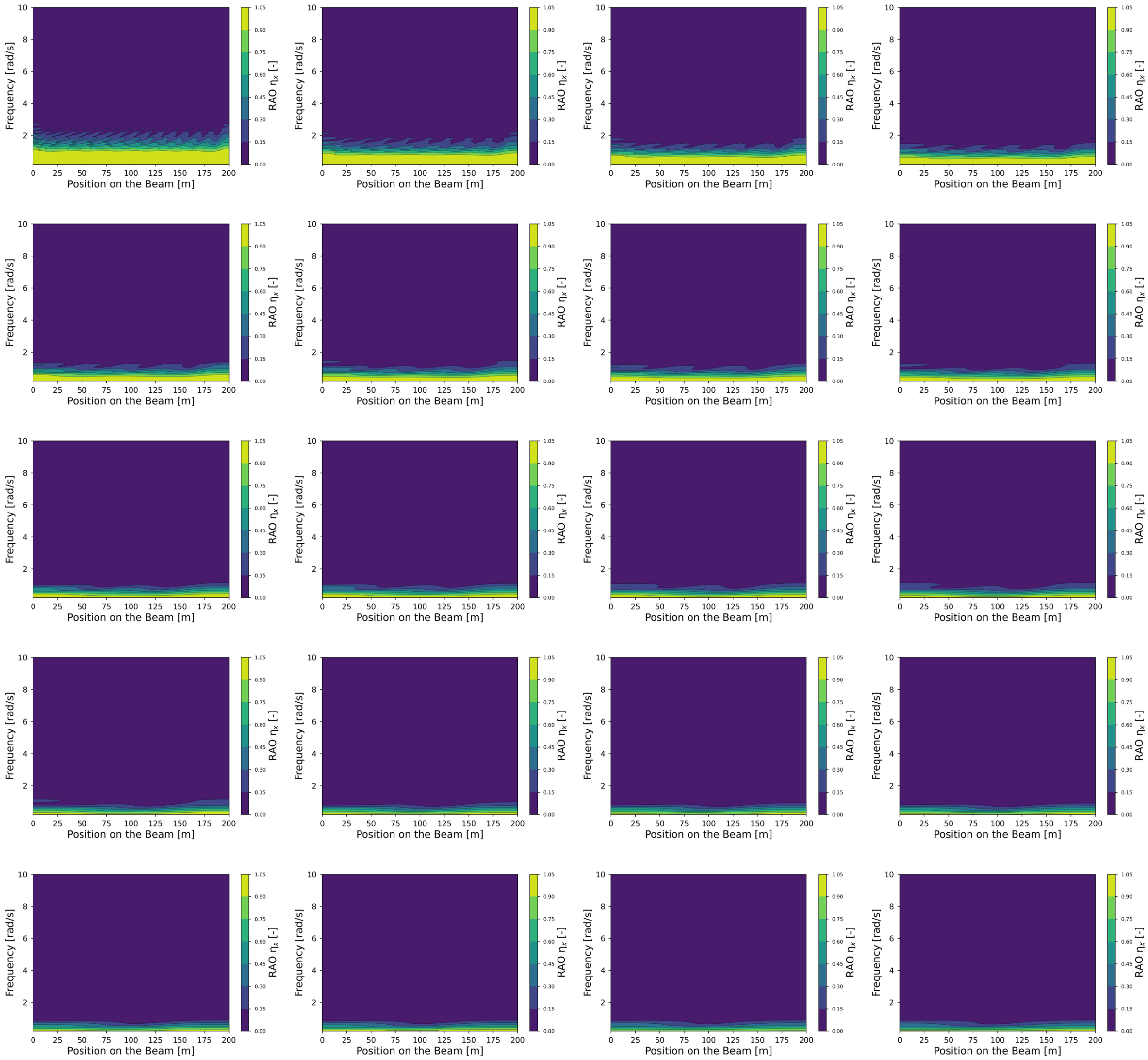

Figure A.6: RAOs for η_x for GFRP for increasing the thickness. Top left (0.1m) to bottom right (2m).

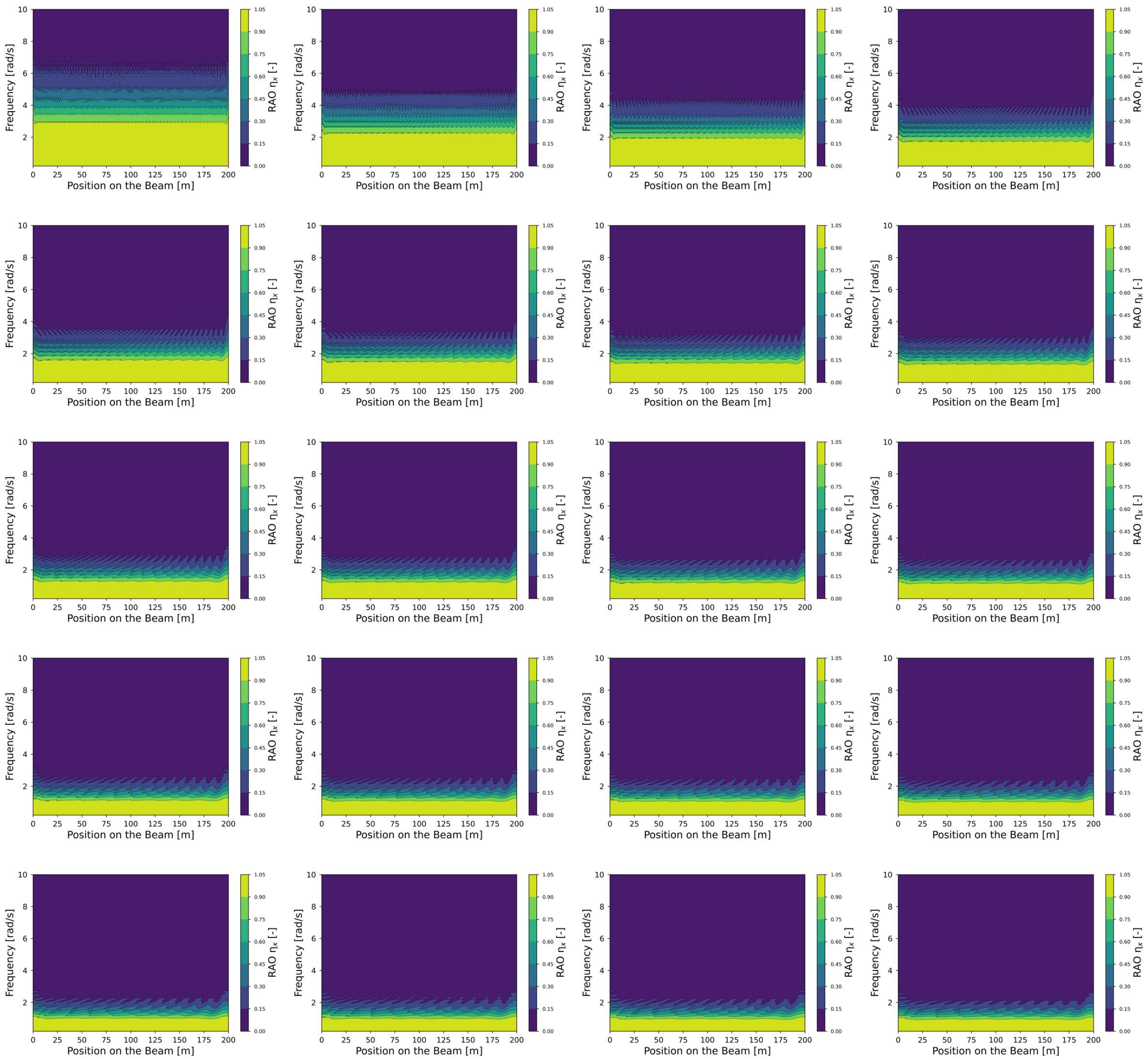

Figure A.7: RAOs for η_x for EPS for increasing the thickness. Top left (0.1m) to bottom right (2m).

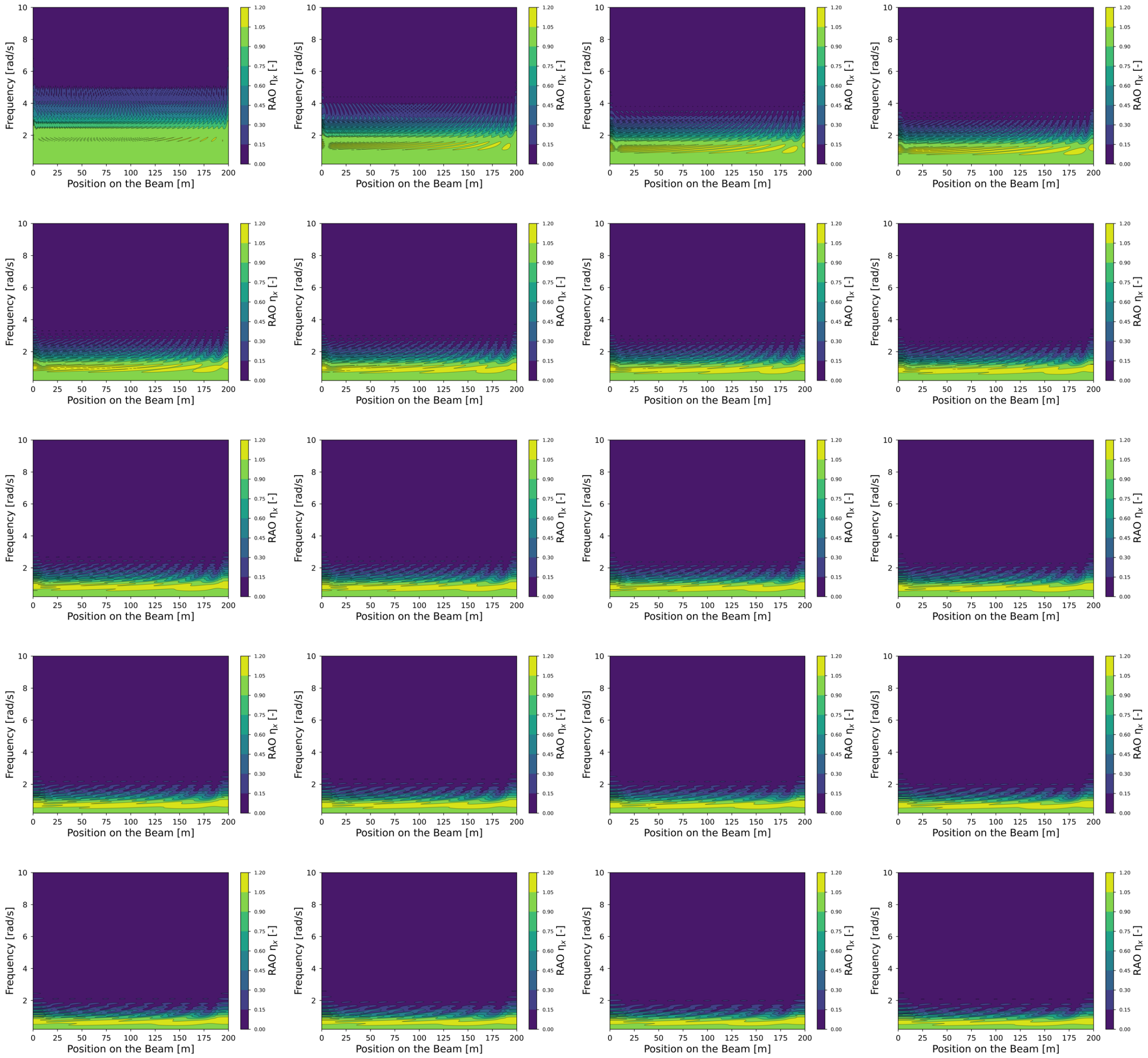

Figure A.8: RAOs for η_x for PVC for increasing the thickness. Top left (0.1m) to bottom right (2m).

A.2. Standard Deviation of the Tilt

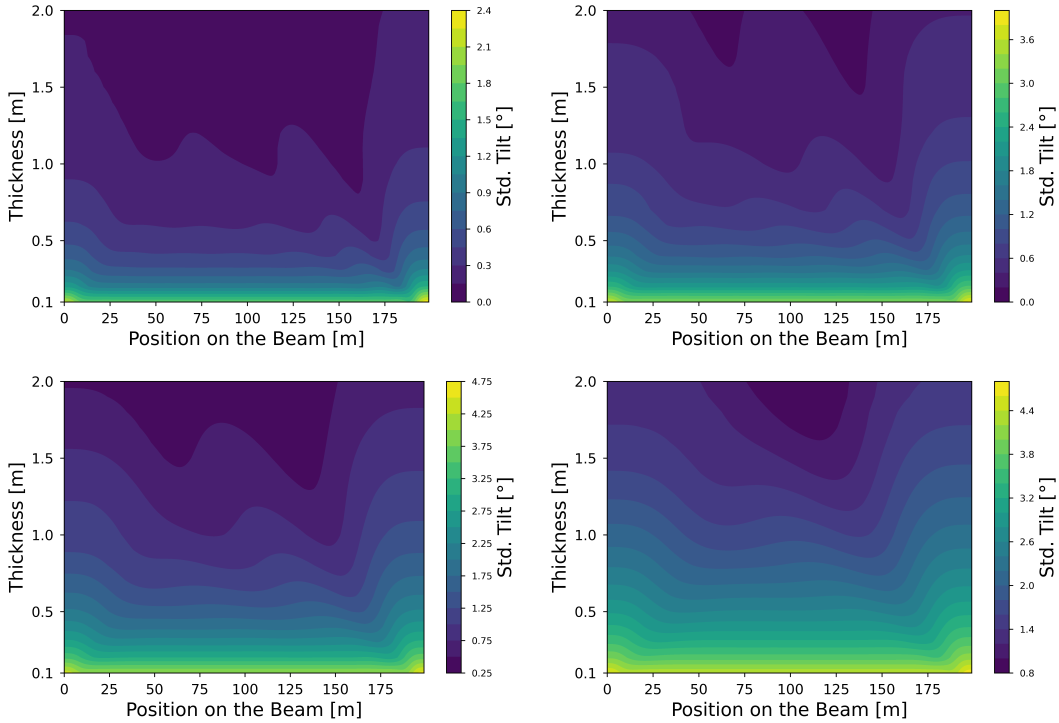

Figure A.9: Standard deviation of the tilt for a calm (top left), moderate (top right), rough (bottom left) and very rough (bottom right) sea for HDPE

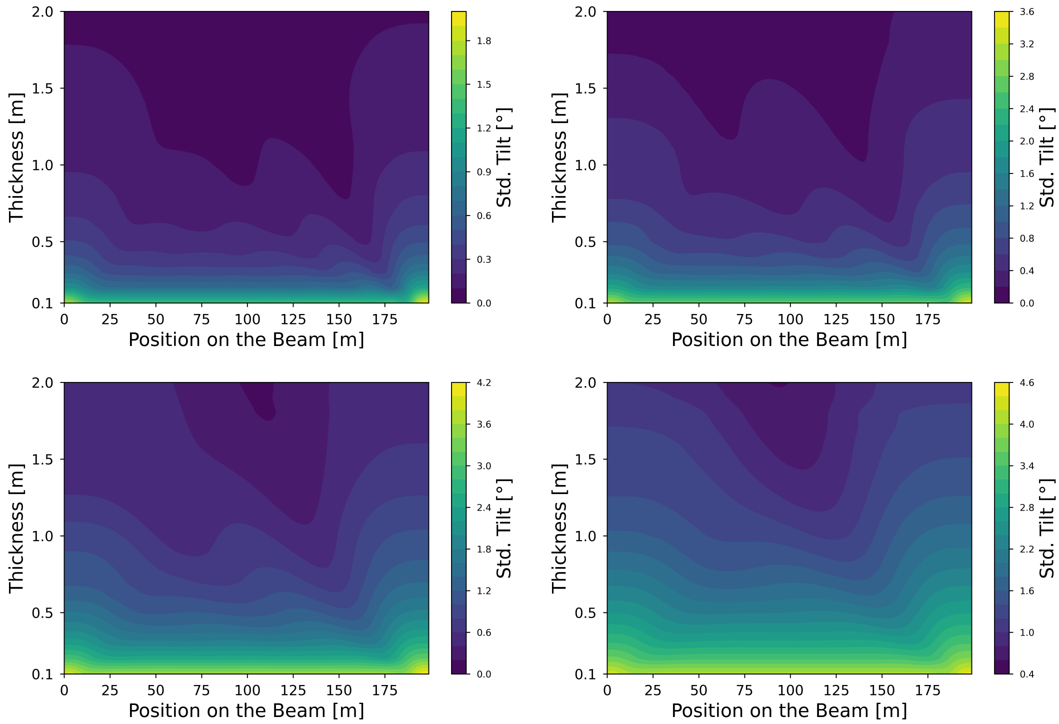

Figure A.10: Standard deviation of the tilt for a calm (top left), moderate (top right), rough (bottom left) and very rough (bottom right) sea for GFRP

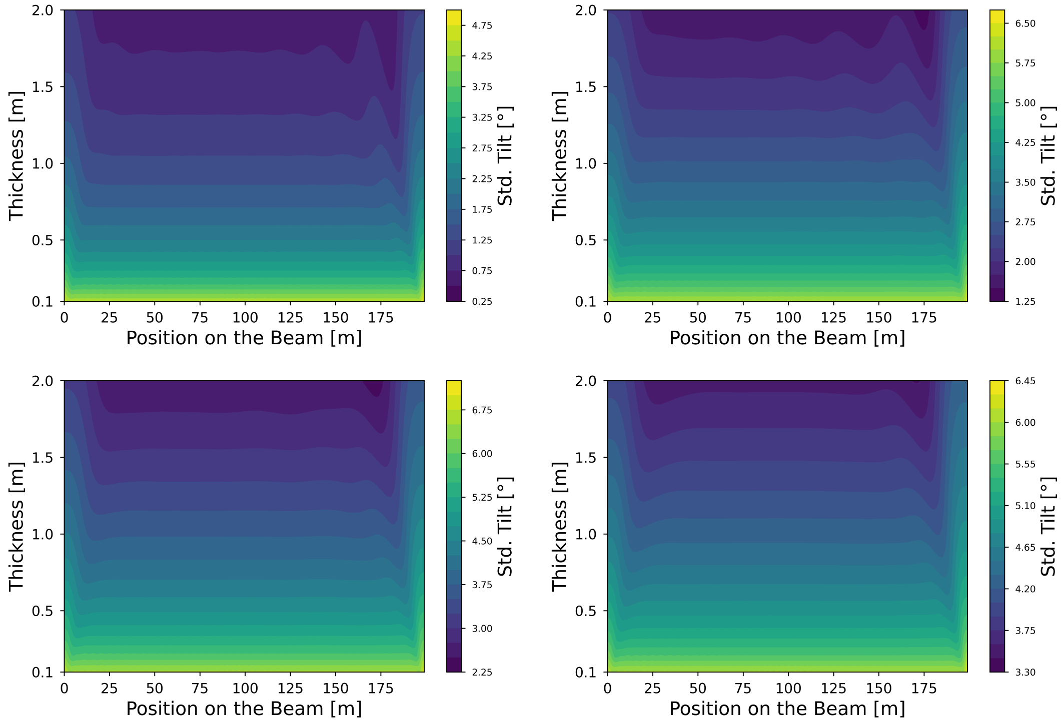

Figure A.11: Standard deviation of the tilt for a calm (top left), moderate (top right), rough (bottom left) and very rough (bottom right) sea for PVC

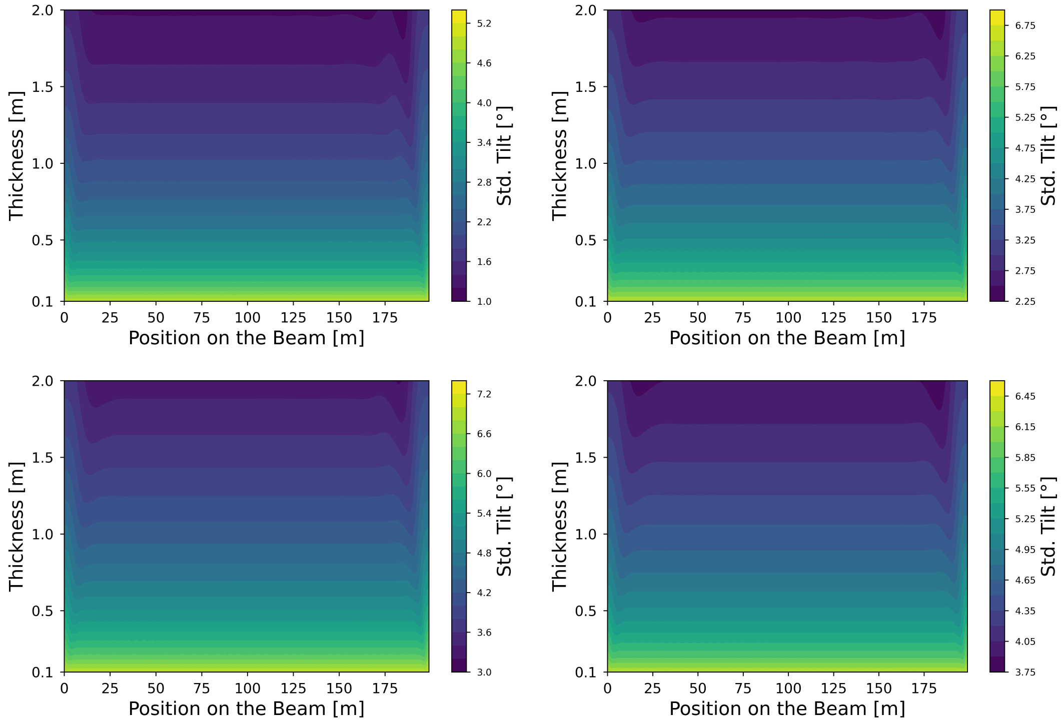

Figure A.12: Standard deviation of the tilt for a calm (top left), moderate (top right), rough (bottom left) and very rough (bottom right) sea for EPS

B

Further Optoelectrical Results

B.1. July and East-ward facing

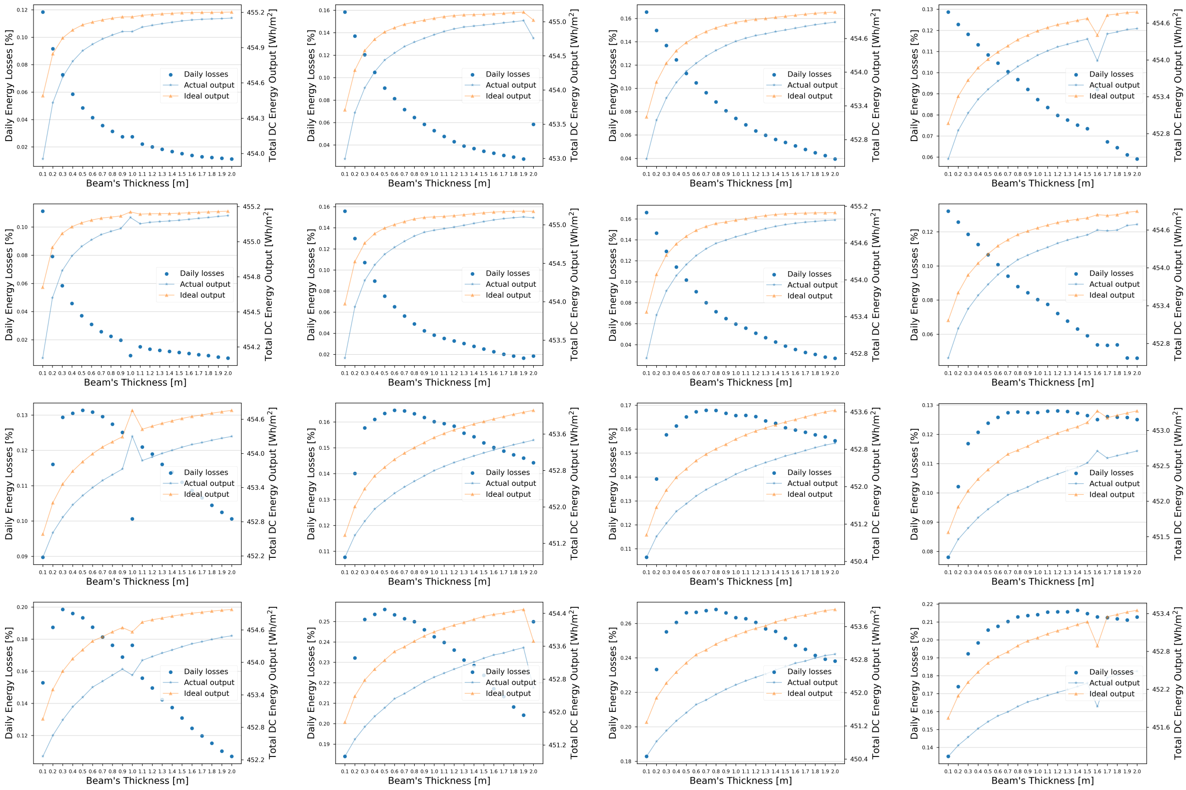

Figure B.1: Energy losses in July for HDPE, GFRP, EPS, and PVC (rows) for slight, moderate, rough, and very rough sea conditions (columns), string's azimuth is East.

B.2. July and South-ward facing

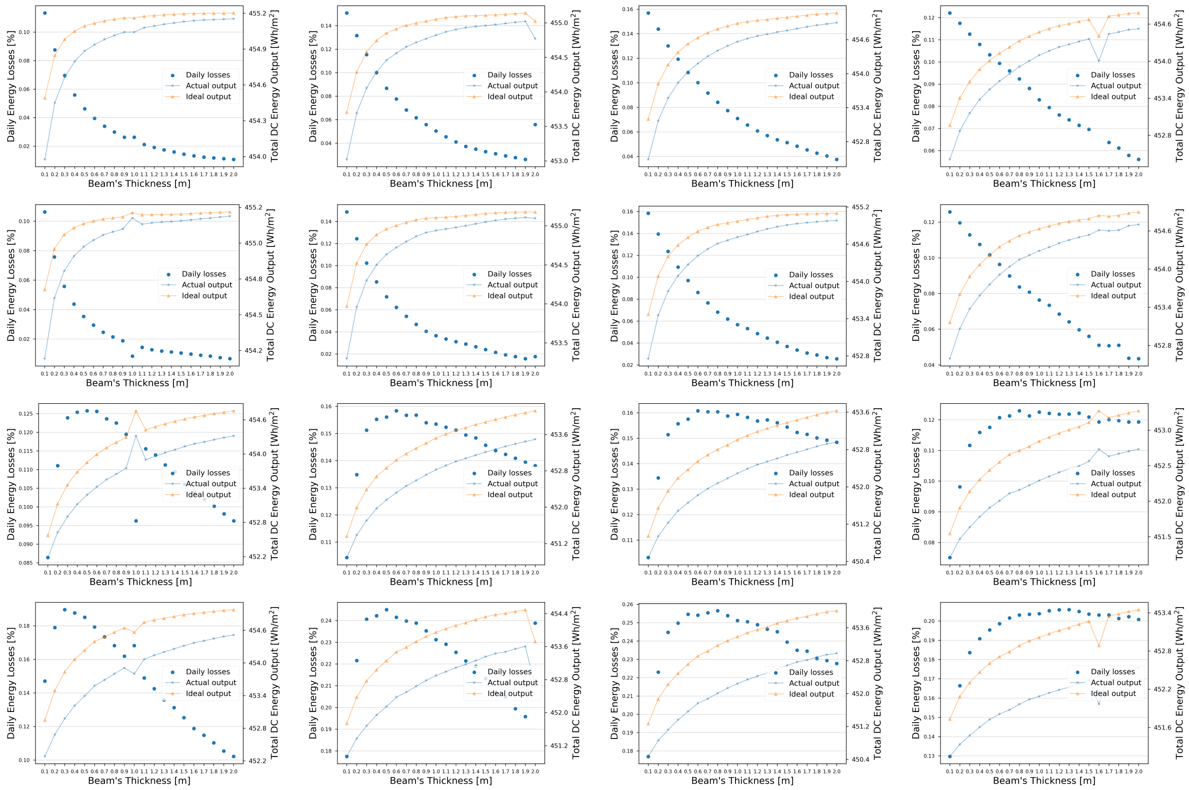

Figure B.2: Energy losses in July for HDPE, GFRP, EPS, and PVC (rows) for slight, moderate, rough, and very rough sea conditions (columns), string's azimuth is South.

B.3. December and East-ward facing

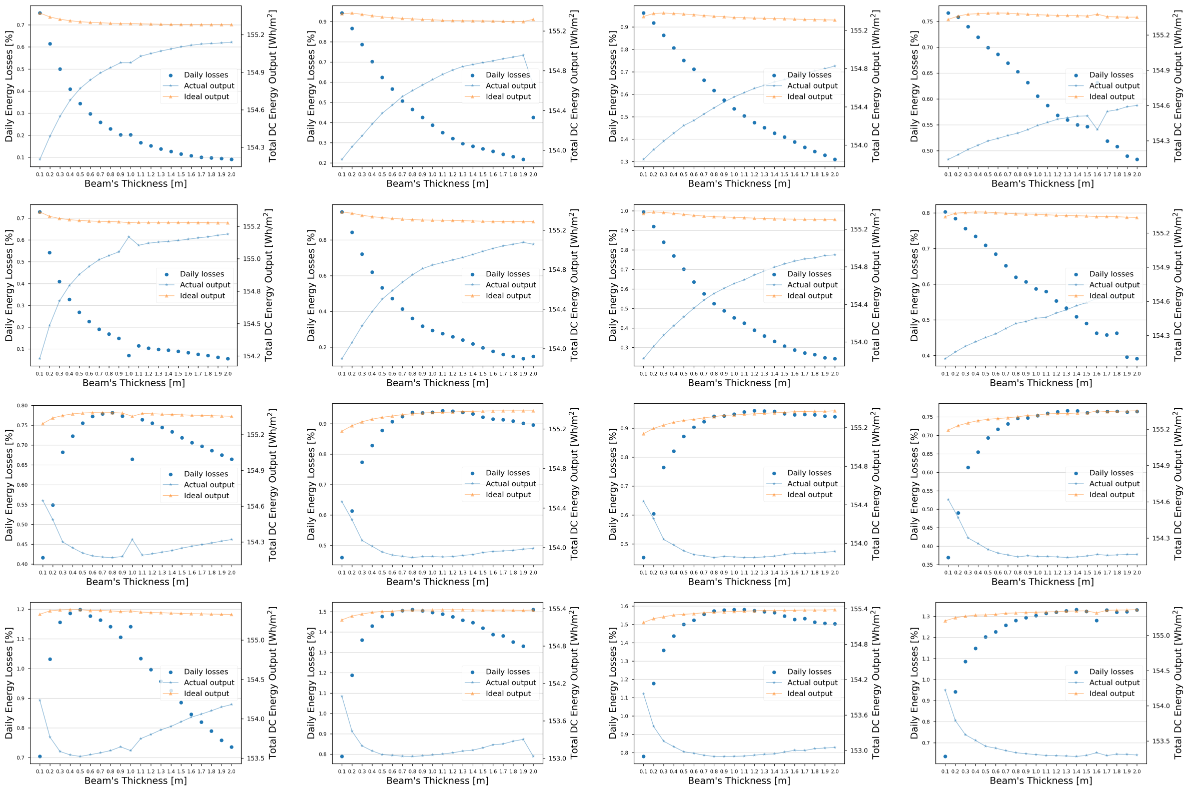

Figure B.3: Energy losses in December for HDPE, GFRP, EPS, and PVC (rows) for slight, moderate, rough, and very rough sea conditions (columns), string's azimuth is East.

B.4. December and South-ward facing

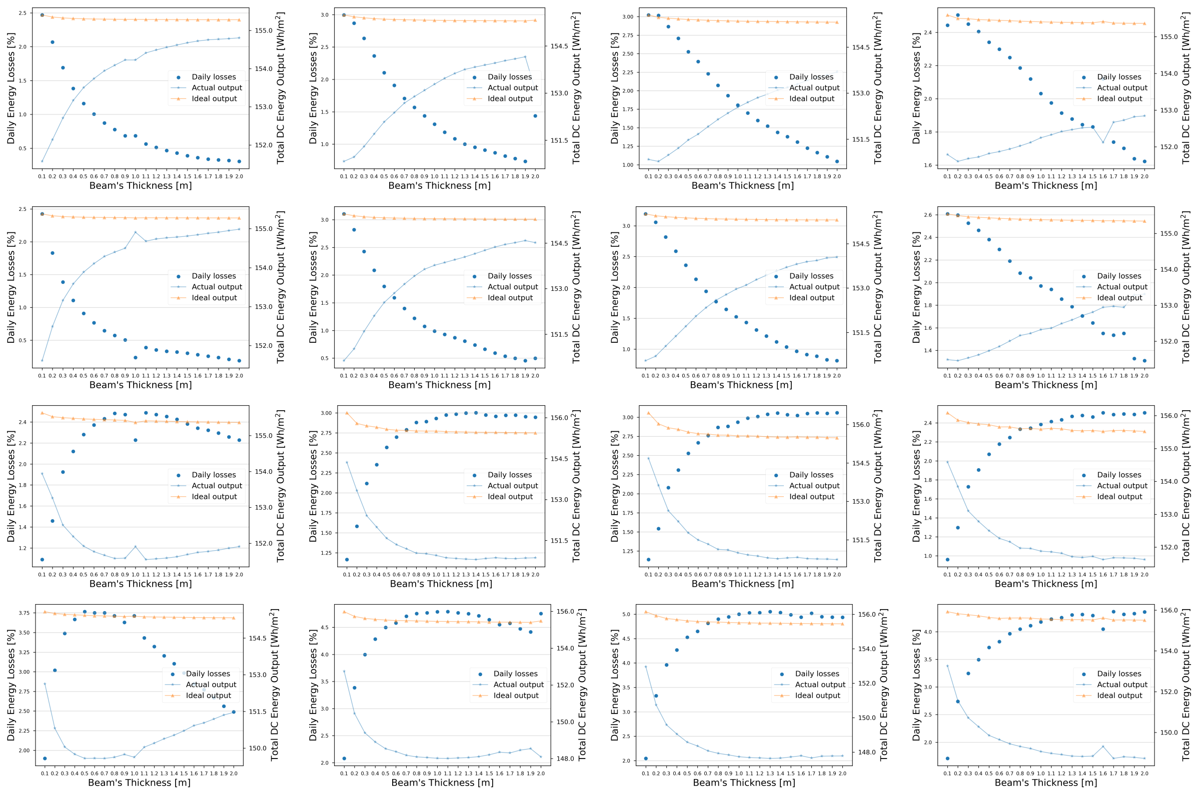

Figure B.4: Energy losses in December for HDPE, GFRP, EPS, and PVC (rows) for slight, moderate, rough, and very rough sea conditions (columns), string's azimuth is South.